Physik Department

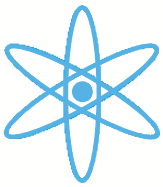

Surface-shifted core level photoemission from clean and oxygen covered metal surfaces

Silvano Lizzit

Dissertation 2003

Technische Universität München
Fakultät für Physik, Lehrstuhl E20 (Oberflächenphysik)

Surface-shifted core level photoemission from clean and oxygen covered metal surfaces

Silvano Lizzit

Vollständiger Abdruck der von der Fakultät für Physik der Technischen Universität München zur Erlangung des akademischen Grades eines

Doktors der Naturwissenschaften

genehmigten Dissertation.

Vorsitzender:		Univ.- Prof. Dr. R. L. Gross
Prüfer der Dissertation:	1.	Univ.- Prof. Dr. Dr. h. c. D. Menzel
	2.	Univ.- Prof. Dr. A. Groβ

Die Dissertation wurde am 03.02.2003 bei der Technischen Universität München eingereicht und durch die Fakultät für Physik am 05.05.2003 angenommen.

Summary

In this thesis, the properties of the binding energy shifts of core electrons arising between surface and bulk atoms, so-called Surface Core Level Shifts (SCLS's), of bare and adsorbate covered metal surfaces have been investigated. The SCLS's are found to be a rich source of chemical and structural information that can be exploited by comparing the experimental results to theoretical calculations. For the systems investigated here, the latter reproduce with high accuracy our experimental SCLS's thus demonstrating that the physical principles governing the SCLS's are well understood. This is due both to the reliability of the calculations as well as to the big advancement in the experimental methods that allow now to measure SCLS's with very high accuracy.

The most important results of this work are summarized in the following.

(1) The SCLS is an interplay between initial state (before ionization) and final state (due to the presence of the core hole) effects. The separation of the two effects can be achieved only on theoretical grounds. The agreement between theory and experiments is really good only if both effects are represented well in the calculations.

(2) When dealing with SCLS's that present more than one shifted component, care must be taken in their assignment to certain atoms. SCLS's of this type are present even in the core level spectra of simple systems like the Be($10\bar{1}0$), Ru($10\bar{1}0$) and Ru(0001) clean metal surfaces. In these cases the SCLS's belong to different atomic layers. We have successfully applied for such systems the high energy resolution photoelectron diffraction approach to distinguish between the SCLS's of first and second layer atoms. Moreover we propose to extend this experimental procedure to other systems for which the surface geometry is already known.

(3) The SCLS's are sensitive to subtle changes of the geometric structure around the emitting atom caused by a temperature change, like the case for surface thermal expansion.
In particular, we have seen that for the Rh(100) surface the $3d_{5/2}$ SCLS decreases on increasing the temperature. The effect was interpreted in terms of a higher anharmonicity of the inter-atomic potential of the surface atoms. For the Be(0001) case, we have developed a new approach for the determination of the multilayer thermal expansion based on the coupling of Be 1s

SCLS measurements, taken at different temperatures, to SCLS theoretical calculations, performed on structures with different relaxations. In this way we determine the surface-layer dependent coefficients of thermal expansion with better accuracy than an earlier LEED study. In particular we find that, while the first interlayer distance strongly expands upon heating, the distance between the second and third layer slightly contracts. This is in agreement with the LEED investigation which found an anomalous thermal expansion of the first-to-second interlayer spacing on Be(0001) but does not agree with highly sophisticated first principle calculations. As a possible reason, we suggest that the inclusion of several variable layer spacings in the theory might improve the result.

(4) The SCLS's are sensitive also to the changes of the chemical environment due to the presence of an adsorbate on the surface. We have studied this for the O/Rh(111) and O/Ru(0001) systems.
We have found that the SCLS's are modified only on those substrate atoms directly bound to the adsorbate and that there is a clear dependence of the SCLS on the number of nearest neighbour O atoms for both systems. Moreover, for both metals the initial state shifts are connected to a varying width of the valence $4d$ band either due to the reduced coordination of the atoms at the surface or to the interaction with the O $2p$ level which causes the formation of bonding and antibonding states widening the band. As the width of the band is connected to the formation of bonds, which scale with the number of directly bound O atoms, similar SCLS's result for equally O coordinated Rh and Ru atoms. The almost linear increase of initial state SCLS for increasingly higher O coordinated metal atoms suggests that the type of bonding remains roughly the same over the considered coverage sequence up to the full monolayer, which may be interpreted as an almost constant amount of charge transferred to each electronegative O atom. These findings confirm that both surfaces show a qualitatively similar on-surface chemisorption behaviour and that a combined experimental and theoretical determination of SCLS's provides valuable insight into the O-metal interaction in different chemical environments.

This study has been limited to the SCLS's of relatively simple systems, because their understanding is a fundamental prerequisite to that of more complicated ones.
Obviously, there are many other interesting problems where the SCLS approach can be applied to advantage. For instance, it is very fruitfully applied to the study of reconstructed surfaces, or that of alloys. For both cases we have already obtained some preliminary results which show that the SCLS's give valuable information also for these systems.

Contents

Introduction

Motivations

Surface Science is a fascinating scientific field because it deals with a special type of systems, i.e. with *surfaces*. The surface is constituted by the few outermost layers of atoms of a solid. When the solid has three dimensional periodicity, the surface is obtained from the breaking of this periodicity in one dimension: for this reason it can be thought of as a particular *defect* of the solid.

Due to the lower dimensionality, the properties of the surface are different than those of the *bulk* of the solid from structural as well as electronic and vibrational points of view. The understanding of these aspects is not only fascinating in itself but is also of practical importance because technological applications are found in many areas of present interest. One of the most well known fields is perhaps *heterogeneous catalysis*: chemicals can be produced easiest in the presence of a catalytic surface, or poisonous exhaust gases are converted into less dangerous gases in a car catalyst. These are just two examples which call for a deep understanding of surfaces due to the need to improve the performances of the already available catalysts, or to find more efficient or cheaper materials to be used in these processes.

In order to reach an understanding of the systems that find use in our daily life, we need to start from a simplified version of these problems. In fact the real catalysts are generally very complicated because, for example, they are constituted of catalytic metal powders dispersed on a porous support, and/or they work at high temperatures or pressures in presence of different kind of molecules in the atmosphere, or they may include different materials, each of them promoting a particular reaction. A good starting point is therefore to study model systems such as well-defined surfaces, like the low index faces of single crystals, or adsorbate overlayers. This can be achieved best by working in an Ultra High Vacuum environment (UHV).

The strong development experienced by UHV technology in the last 40 years has prompt a large number of such studies. Moreover, UHV allows to use a variety of techniques that are very well suitable to study surfaces and that have also experienced big improvements in the last years, the most notable being photoelectron spectroscopy.

This thesis deals with experimental studies of clean and oxygen covered metal surfaces using this technique. Since the development of third generation synchrotron radiation facilities the experimental resolution of photoelectron spectroscopy has improved so much that now new core level shifted components can be distinguished in the measured spectra, like those related to the surface atoms, so called Surface Core Level Shifts (SCLS). The central issue of this thesis is to show, first, that the origin of SCLS's is well understood for a variety of metal surfaces and in different conditions like different substrate temperature or in the presence of an adsorbate on the surface and, second, that the SCLS's are a rich source of chemical and structural informations. The interpretation of the measured SCLS's is mainly made by using theoretical calculations.

Overview

In *Chapter 1* the basic physical principles of photoelectron spectroscopy, SCLS's and photoelectron diffraction are described.
In *Chapter 2* we describe the experimental apparatus that we used to perform the high resolution core level photoemission measurements.
In *Chapter 3* we show how the high-resolution angle scan photoelectron diffraction technique is applied to make the assignment of the SCLS to the first and second layer atoms of a clean metal surface.
In *Chapter 4* we show the temperature behaviour of the SCLS of a clean metal surface. In particular we explain how the SCLS can become a valuable tool to measure the multylayer thermal expansion.
Chapter 5 is devoted to the study of the SCLS's induced by the oxygen adsorption on Rh(111) and Ru(0001) surfaces.

Chapter 1

Core Level Photoemission Spectroscopy

The photoemission spectroscopy technique is based on the photoelectric effect which was discovered by Albert Einstein in 1905. For this Einstein was awarded the 1921 Nobel Prize in Physics [1]. Later on, in the 60's, Kai M. Siegbahn developed the ESCA (Electron Spectroscopy for Chemical Analysis) technique and he also won the Nobel prize in 1981 "*for his contribution to the development of high-resolution electron spectroscopy*" [2]. Since then, photoelectron spectroscopy has attracted a lot of attention for its unique properties and has been used in many fields like the study of heterogeneous catalysis, corrosion prevention, tribology as well as to new materials development and semiconductor technology.
One of the most striking properties of this technique is its *chemical sensitivity* (this is the reason for the name ESCA). The electrons that are photoemitted in the photoemission process, have a particular binding energy which is a fingerprint of the elements present in the sample. Moreover, also different types of bonds affect these binding energies creating the so called *chemical shifts* which are useful to distinguish between atoms or molecules in different chemical or structural environments.
The other important property is the *surface sensitivity* of this technique. Infact, one of the main reasons to use electrons in surface science (in this case the electrons are created in the photoemission process, the photo-electrons) is the inelastic mean free path of the electrons in matter. This is shown in fig. 1.1 as a function of the kinetic energy of the electrons, in the energy range tipical of photoemission experiments. It can be noted that the measured data from many elemental solids follow more or less the calculation: for this reason the curve is often called *universal curve*. Moreover the mean free path curve shows a broad minimum around 70 eV kinetic energy, where it is less than 10 Å. This means that the photo-electrons observed without energy loss originate from the first few layers of the solid. This renders pho-

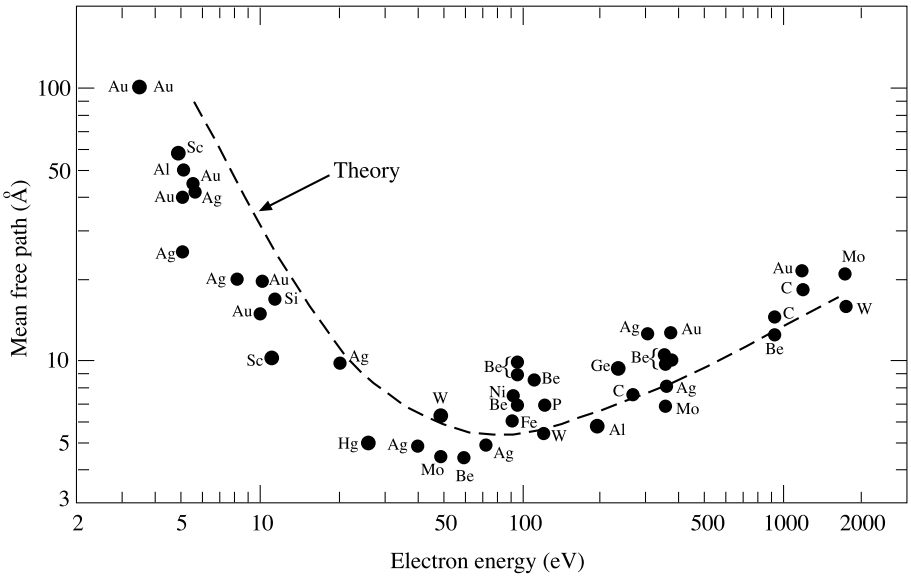

Figure 1.1: Universal curve of dependence of the inelastic mean free path on the electron kinetic energy [3].

toemission spectroscopy suitable to identify the chemical elements present on a surface and in the first substrate layers and to gain insight on the actual electronic structure of the surface itself.
All of these informations are not of easy access by using other techniques instead of photoemission spectroscopy which is itself a straightforward technique in this respect.

The photoemission event from a solid takes place when electromagnetic radiation, i.e. the photons of a proper source hit the solid and kick out electrons that are detected outside . Obviously the energy of the photons, $h\nu$, have to be high enough in order to remove the electron from the proper core level and let it overcome the work function ϕ of the solid. The energy distribution of the electrons detected outside reflects in this way the density of states inside the solid. This is schematically shown in fig. 1.2. If we refer the binding energies to the Fermi level E_F, E_b^F, a quantity that can be easily measured in the photoemission spectrum from a metal, then the energy with respect to the vacuum level E_b becomes:

$$E_b = E_b^F + \phi \tag{1.1}$$

The kinetic energy of the electrons in the vacuum level is given by

$$E_{kin} = h\nu - E_b^F - \phi \tag{1.2}$$

Once the electron is in the vacuum level, in order to enter in the analyser, its energy is changed by the difference in the work function between the electron

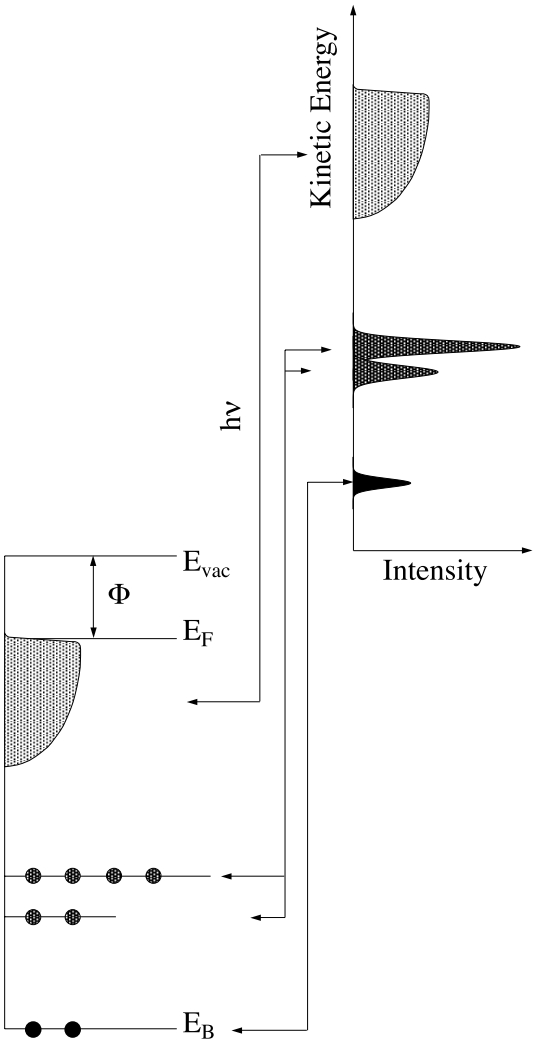

Figure 1.2: Schematic representation of the photoemission process. The circles represent the electrons in the core levels.

energy analyser $\phi_{analyser}$ and the sample. This is because the sample is electrically connected to the spectrometer and therefore they have a common Fermi level. In this way, the measured photoemission signal does not depend anymore on the work function of the sample but from that of the analyser only

$$E_{kin}^{meas} = E_{kin} - \phi_{analyser} = h\nu - E_b^F - \phi - (\phi_{analyser} - \phi) =$$
$$= h\nu - E_b^F - \phi_{analyser}. \tag{1.3}$$

The trick in a photoemission experiment is therefore to use monochromatic light, i.e. with a well defined energy, to ionize the sample and obtain, through

the relations 1.2 and 1.3, once the work function ϕ is known, the binding energies of the electrons in the solid. Since these binding energies are individual for all the elements in the periodic table, and have been already tabulated , it is possible to detect and study in this way a well defined chemical element.
Depending on the energy of the photons used to ionize the sample, the photoemission technique can be divided into two main branches, namely UPS (Ultraviolet Photoemission Spectroscopy) and XPS (X-ray Photoemission Spectroscopy). The UPS, performed with low photon energies, deals mainly with the valence levels while in XPS the higher energy of the photons allows to ionize deeper electronic core levels. For this reason it is also called Core-Level Photoemission Spectroscopy. In the following the XPS technique will be considered.

In order to form a molecule or a solid, individual atoms have to be brought together. The bond between the atoms can be formed only if this rearrangement lowers the energy of the system. This causes, in the case of molecules, the formation of molecular orbitals while, in the case of a solid, the appearance of energy bands. Since the core levels are too deep in order to participate directly in the bonding, they usually retain their localized atomic character. However, even if they do not participate, they feel the bonding itself through the changed potential and this causes a shift in their binding energy with respect to the free atom case. By measuring these shifts it is possible to distinguish between several identical but chemically inequivalent atoms in a molecule or, considering a solid surface, to distinguish between atoms or molecules sitting in different adsorption sites [4, 5] or, even more, to distinguish between surface and bulk atoms of a solid. This last shift is called Surface Core Level Shift and is the subject of the present thesis.

1.1 The photoemission process

The photoemission process is the result of the transition of the electrons from initial, occupied states, to free final states. In order to describe such a process, we need to consider the wave function and the energy of the system before and after the interaction with an electromagnetic radiation field with energy $h\nu$. Therefore, considering a system with N electrons, the removal of one electron from the orbital k can be sketched as follows [6]:

$$\Psi^i_{tot}(N)E^i_{tot}(N) \stackrel{h\nu}{\rightarrow} \Psi^f_{tot}(N,K)E^f_{tot}(N,K). \tag{1.4}$$

where $\Psi^i_{tot}(N)$ is the initial state wavefunction of the N electrons with total energy $E^i_{tot}(N)$ and $\Psi^f_{tot}(N,K)$ is the final state wavefunction of the N electrons with total energy $E^f_{tot}(N,K)$. Here K denotes not only the orbital

from which the electron has been removed but also the excitation modes of the final state.

The energy of the system is conserved, which means that

$$E^i_{tot}(N) + h\nu = E^f_{tot}(N, K). \tag{1.5}$$

If we consider the electron in the final state as being decoupled from the remaining N-1 electrons of the system, the energy of the final state is the sum of that of the ionic system $\Psi^f_{tot}(N-1, K)$ and that of the electron with kinetic energy E_{kin}. The energy can be expressed as

$$E^i_{tot}(N) + h\nu = E^f_{tot}(N-1, K) + E_{kin}. \tag{1.6}$$

The binding energy of the electron becomes therefore

$$E_b(K) = h\nu - E_{kin} = E^f_{tot}(N-1, K) - E^i_{tot}(N), \tag{1.7}$$

i.e. it is given by the difference between two total energies. Its width, for a system with N electrons and p nuclei, will be explained more extensively in sect. 1.2.3.
The dependence of E_b on the energy of the ionic system causes the broadening of the photoemission peaks because of the Heisemberg uncertainty principle

$$\Delta E \Delta t \geq \hbar/2 \tag{1.8}$$

with $\hbar = 6.6 \times 10^{-16}$ (eV·s). This gives a line width broadening of the order of $\hbar/\tau$ with τ the lifetime of the core-hole in seconds.

1.1.1 Photoemission cross section

Let's calculate now the probability per unit time for exciting a system from an initial state $\Psi^i(N)$ to a final state $\Psi^f(N)$ with photon flux of 1 $cm^{-2}s^{-1}$, which is the photoemission cross section [6]. In order to do this, we need to consider the Hamiltonian for a system in presence of an external electromagnetic field. From the classical point of view, considering Maxwell's equations, a particle with charge e and velocity $\mathbf{v}$ in an electromagnetic field defined with $\mathbf{E}$ and $\mathbf{B}$ feels the Lorentz's force which amounts to

$$\mathbf{F} = e(\mathbf{E} + \frac{1}{c}\mathbf{v} \wedge \mathbf{B}). \tag{1.9}$$

The electromagnetic radiation can be defined via the scalar potential V and the vector potential $\mathbf{A}$ that obey the following relations:

$$\mathbf{E} = -gradV - \frac{1}{c}\frac{\partial \mathbf{A}}{\partial t}$$

$$\mathbf{B} = rot\mathbf{A}. \tag{1.10}$$

The Hamiltonian of the system is therefore:

$$H = \sum_{n=1}^{3} \frac{1}{2m}(p_n - \frac{e}{c}A_n)^2 + eV + U \tag{1.11}$$

where m is the electron mass, p_n are the components of the electron momentum, and U is an external potential. The Hamiltonian operator can be written as:

$$\hat{H} = \frac{\hat{\mathbf{p}}^2}{2m} - \frac{e}{2mc}(\hat{\mathbf{p}}\hat{\mathbf{A}} + \hat{\mathbf{A}}\hat{\mathbf{p}}) + \frac{e^2}{2mc^2}\hat{\mathbf{A}}^2 + e\hat{V} + \hat{U} \tag{1.12}$$

or using the commutator $[\hat{\mathbf{p}}, \hat{\mathbf{A}}] = -i\hbar\nabla\hat{\mathbf{A}}$

$$\hat{H} = \frac{\hat{\mathbf{p}}^2}{2m} - \frac{e}{2mc}(2\hat{\mathbf{A}}\hat{\mathbf{p}} - i\hbar\nabla\hat{\mathbf{A}}) + \frac{e^2}{2mc^2}\hat{\mathbf{A}}^2 + e\hat{V} + \hat{U}. \tag{1.13}$$

The term $e^2/2mc^2\hat{\mathbf{A}}^2$ is always *small* and can be neglected. Moreover, within the *Coulomb gauge*, the scalar potential $V = 0$. Furthermore, considering a propagating *transverse wave*, the term $\nabla\hat{\mathbf{A}} = 0$ and the Hamiltonian becomes:

$$\hat{H} = \frac{\hat{\mathbf{p}}^2}{2m} + \hat{U} - \frac{e}{mc}\hat{\mathbf{A}}\hat{\mathbf{p}}. \tag{1.14}$$

The first two terms represent the Hamiltonian $\hat{\mathbf{H}}_0$ of the unperturbated system while the last term represents the perturbation Hamiltonian

$$\hat{H}' = -\frac{e}{mc}\hat{\mathbf{A}}\hat{\mathbf{p}}. \tag{1.15}$$

Since the interaction of the photons with charged particles is a time dependent process, we make use of the time dependent perturbation theory for solving this problem. The transition rate between the initial state $\Psi^i(N)$ and the final state $\Psi^f(N)$ is given by *Fermi's golden rule* [7]:

$$\frac{d\omega'}{dt} \propto | < \Psi^f(N)|\hat{H}'(N)|\Psi^i(N) > |^2\delta(E_f - E_i - h\nu) \tag{1.16}$$

or, considering eq. 1.15

$$\frac{d\omega'}{dt} \propto | < \Psi^f(N)|\sum_{i=1}^{N}\hat{\mathbf{A}}(\mathbf{r}_i)\hat{\mathbf{p}}_i|\Psi^i(N) > |^2\delta(E_f - E_i - h\nu). \tag{1.17}$$

The incident radiation can be described as a superposition of plane waves with angular frequency ω, photon wavevector $\mathbf{k}'$ directed along the propagation direction, $|\mathbf{k}'|=2\pi/\lambda = \omega/c$, and amplitude εA_0, with ε a unit vector parallel to the polarization :

$$\mathbf{A}(\mathbf{r}, t) = \varepsilon A_0 e^{i(\mathbf{k}'\mathbf{r} - \omega t)}. \tag{1.18}$$

From this, the square of the matrix element $M_{f\leftarrow i}$ of eq. 1.17, that defines the differential cross section $d\sigma/d\Omega$, becomes:

$$|M_{f\leftarrow i}|^2 \;=\; \hbar^2 A_0^2 | < \Psi^f(N)| \sum_{i=1}^{N} e^{i\mathbf{k'}\mathbf{r}_i} \varepsilon \nabla_i |\Psi^i(N) > |^2. \tag{1.19}$$

Assuming electron kinetic energies lower than 1 keV, the wavelenght λ is much longer than the atomic distances; in this way the exponential can be approximated to

$$e^{i\mathbf{k'}\mathbf{r}} = 1 + i\mathbf{k'}\mathbf{r} - \frac{1}{2}(\mathbf{k'}\mathbf{r})^2 \approx 1. \tag{1.20}$$

thus giving eq. 1.19 in the form

$$|M_{f\leftarrow i}|^2 \;=\; \hbar^2 A_0^2 | \varepsilon < \Psi^f(N)| \sum_{i=1}^{N} \nabla_i |\Psi^i(N) > |^2. \tag{1.21}$$

This is the so-called *dipole-approximation.*
The differential photoionization cross section is given by

$$\frac{d\sigma}{d\Omega} = C \left(\frac{1}{h\nu}\right) |\varepsilon < \Psi^f(N)| \sum_{i=1}^{N} \nabla_i |\Psi^i(N) > |^2. \tag{1.22}$$

Using commutation relations the matrix element in eq. 1.22 can be written in the equivalent forms

$$\frac{i}{\hbar} < \Psi^f(N)| \sum_{i=1}^{N} \mathbf{p}_i |\Psi^i(N) >, \tag{1.23}$$

$$\frac{m\omega}{\hbar} < \Psi^f(N)| \sum_{i=1}^{N} \mathbf{r}_i |\Psi^i(N) >, \tag{1.24}$$

$$\frac{1}{\hbar\omega} < \Psi^f(N)| \sum_{i=1}^{N} \nabla_i V |\Psi^i(N) > . \tag{1.25}$$

with V the potential of the unperturbated Hamiltonian $\hat{H}_0$. The matrix element in eqs. 1.23, 1.24 and 1.25 represent the *dipole momentum*, *dipole lenght* and *dipole acceleration* terms respectively. From the last equation it can be seen that for a constant potential like in free space no photoemission can take place.

1.1.2 Sudden approximation

In order to determine the transition rate one should know the many-body wave functions of the initial and final states. The most often used approximation for further treatment of this problem is to work in a single-particle picture. In this way, the wave function of the initial/final state can be split into two contributions, namely a one-electron and a (N-1) electrons wave function. The initial, ground state wave function is therefore

$$\Psi^i(N) = \psi_k(1)\Psi_R(N-1), \tag{1.26}$$

while in the final state

$$\Psi^f(N) = \phi_f(1)\Phi_{k,j}(N-1), \tag{1.27}$$

where $\psi_k(1)$ is the single-particle wave-function of the electron to be removed from orbital k, $\Psi_R(N-1)$ is the anti-symmetrized determinant of the $N-1$ electrons in the initial state, $\phi_f(1)$ is the wave-function of the free electron and $\Phi_{k,j}(N-1)$ are the possible states of the ionic system that has one electron missing in orbital k.
A further assumption is the so-called *sudden approximation* where the transition from the initial to the final state is fast compared to the relaxation times of the $N-1$ electrons [8]. The N electrons matrix elements present in eqs. 1.22-1.25 split up into a single and many-particle part and the differential cross section becomes:

$$\frac{d\sigma}{d\Omega} \propto | < \phi_f(1)|\varepsilon\mathbf{r}|\psi_k(1) >< \Phi_{k,j}(N-1)|\Psi_R(N-1) > |^2. \tag{1.28}$$

1.1.3 Relaxation effects

Free atoms

Let's consider now the core-level photoemission process taking place on a free atom and discuss, keeping in mind eq. 1.28 the corresponding binding energy positions.
When $< \Phi_{k,j}(N-1)|\Psi_R(N-1) >= \delta_{k,0}$, the matrix element turns into the single-particle picture

$$\frac{d\sigma}{d\Omega} \propto | < \phi_f(1)|\varepsilon\mathbf{r}|\psi_k(1) > |^2. \tag{1.29}$$

which is the form widely used to perform cross sections calculations. In this case the N-1 electrons in the ionic state do not feel the presence of the hole and just remain in the same positions and with the same energy as in the non-ionized system i.e. they are *frozen* in their original distribution, which is the assumption of Koopmans' theorem [9]. This means that the electron binding energy as calculated with eq. 1.7 within the Hartree-Fock theory

for total energy calculations, explained in more detail in sect. 1.2.3, simply equals the negative orbital energy ϵ_k

$$E_b(K) = -\epsilon_k. \tag{1.30}$$

In the real system, firstly electron correlation effects, not considered in the Hartree-Fock approximation, have to be taken into account and the corresponding energy difference is denoted with ΔE_c, secondly, the effect of the presence of the hole must be included. Infact, since the remaining electrons do feel the ionization, they reorganize themselves to the new potential. This effect is called *intra-atomic relaxation* and it depends on the kinetic energy of the emitted electron. In the case of low kinetic energy, we are in the *Adiabatic* limit in which the N-1 electrons system is left fully relaxed, i.e. in the ionic state with the lowest energy. In this case the ejected electron picks up the full relaxation energy ϵ_{rel} thus increasing its kinetic energy.
The photoemission spectrum is qualitatively similar to that calculated in the frozen orbital approximation but now the binding energy of the photoelectron becomes

$$E_b(K) = -\epsilon_k + \Delta E_c - \epsilon_{rel} \tag{1.31}$$

A large ϵ_{rel} implies that the initial and final state wave functions are very different. The Adiabatic approximation is valide in the time regime of $10^{-15} - 10^{-16}$ s.
When we consider higher photon energies, i.e. higher kinetic energies of the emitted electrons, the time scale of the photoemission process falls in the region of 10^{-17} s and the sudden approximation is applicable. This means that the photoemission process is faster than the relaxation and the N-1 electrons system is left, with a certain probability, in an excited state. Therefore in eq. 1.28, if we project $\Psi_R(N-1)$ onto the eigenstates of the ionic system there will be overlap not only with the ground state but also with some of the excited states with j not equal to zero. This reduces the energy given to the photoelectron and features with kinetic energy lower than that of the fully relaxed, adiabatic *main line*, named satellites, shake-up or shake-off , appear in the spectrum.
All the structures present in a spectrum, coming from a well defined excitation, are related to the binding energy of the Koopmans' theorem through the "sum rule"

$$-\epsilon_k = \frac{\sum_p (E_b)_p I_p}{\sum_p I_p} \tag{1.32}$$

where I_p is the intensitiy of the peak at binding energy $(E_b)_p$. This is shown in fig. 1.3

Let's consider again eq. 1.29 and decompose the initial and final wave functions $\psi_k(1)$ and $\phi_f(1)$ into a radial and an angular part (the spin part

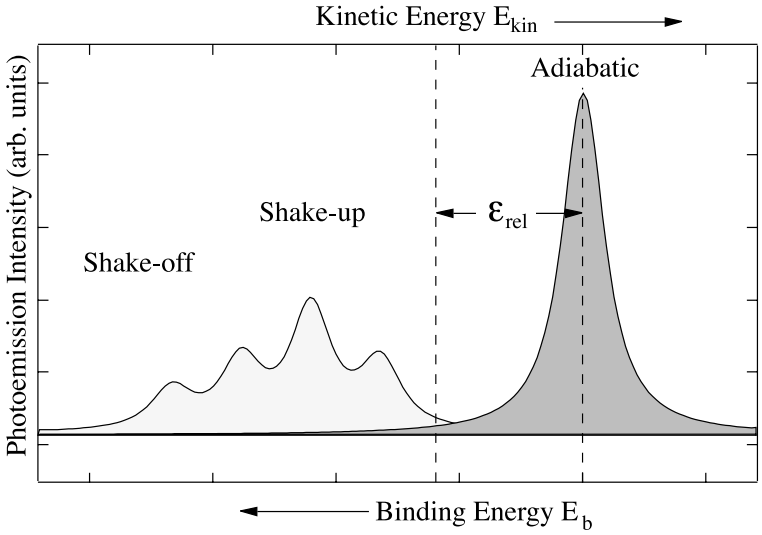

Figure 1.3: Schematic representation of an XPS spectrum. The main line is the adiabatic peak while the other, smaller components, are the shake-up and shake-off transitions. The total area under the curves corresponds to the intensity calculated in the frozen-orbital approximation.

is neglected)

$$\psi_k(1) = U_{nl}(r)Y_{lm}(\theta,\varphi), \tag{1.33}$$

$$\phi_f(1) = U_{l'}(r)Y_{l'm'}(\theta,\varphi), \tag{1.34}$$

where l, l' are the initial and final orbital quantum numbers, m, m' are the initial and final magnetic quantum numbers and n is the initial principle quantum number. The evaluation of the angular integrals in eq. 1.29 leads to the well known selection rules

$$l' = l \pm 1 \qquad m' = m, m \pm 1. \tag{1.35}$$

Therefore for a given l the final state will be a coherent sum of the two angular momentum states $l+1$ and $l-1$, generally called *channel up* and *channel down*. In general it is found that for photon energies well above threshold the channel up is the most probable. The actual cross section is now contained in the radial integrals that are also influenced by the n and l values.

Metals

Let's consider now an atom placed in a solid metal surface. In this case, the presence of all the nuclei should be considered in eq. 1.4 but, by using the Born-Oppenheimer approximation explained more extensively in sec. 1.2.3,

it is possible to decouple the Hamiltonian of the nuclei from that of the N electrons. Therefore eq. 1.7 can be used again to estimate the core level binding energies.
In a metal, the valence electrons available in the conduction band are very mobile and therefore can flow to the site of the core-hole, screening in this way its positive charge. This means that the core ionized atom is a neutral atom with a core hole, compared to the free atom case whose final state is an ionic state.
In the adiabatic limit, the full energy coming from the valence electrons is transfered to the emitted electron. Thus, its kinetic energy is higher than from the atom in its free state, by an amount called *interatomic relaxation* energy, denoted here with ϵ_{rel}^{int}.
In the sudden approximation we would expect to see well separated shake-up and shake-off related features in the spectrum as explained before for the free atom case. This does not happen for the atom in the solid because its excited states now form a continuum in the valence band. In this case electron-hole pairs around the Fermi level are excited. These low energy excitations give rise to a low kinetic energy tail to the observed photoemission peak. This effect was firstly experimentally observed on many metals by Hüfner *et al* [10, 11]. The most important conclusion of these studies was that the transition metals exibit larger asymmetry than noble metals. The reason of this is that the transition metals have higher density of states at the Fermi level which results in higher probability of core-hole creation.

1.1.4 Core level line shape

The shape of an XPS spectrum is much more complicated than that described in the previous section. There are many contributions that one has to take into account in order to explain the spectral features and their line profile [12]. In particular in the case of a solid excitations other than the shake-up and shake-off are possible in the photoemission process, like surface or bulk *plasmons* that are collective oscillations of the electrons in valence band. The corresponding satellites will have lower kinetic energy (by multiples of the plasmon energy) than the adiabatic peak.
All the losses explained up to now take place in the photoemission process itself and for this reason they are called *intrinsic losses*. There is however another possibility in a solid, i.e. to have *extrinsic losses* which can be incurred by the emitted electrons during their transport from the emitting atom to the surface. The inelastic scattering suffered by these electrons leads to the creation of electron hole pairs as well as to plasmons which effect on the spectral line profile adds to that of the intrinsic losses. Unfortunately, a clear separation between these two types of losses is difficult to achieve, because the time that the photoelectron needs to reach the surface is not

long compared to the photoemission process itself and the two effects can interfere coherently. Therefore care has to be taken when applying the sum rule of eq. 1.32 in the case of core level photoemission from solids.
Another factor that can show an effect in the core level spectra is the vibrational motion of the ions around their lattice points. This effect is analogous to the vibrational excitations caused by electronic transitions in molecules. In this case the removal of a core electron modifies substantially the electronic structure of the emitting atom thus influencing also the bond equilibrium positions and the potential energy curve of the molecule. Since the photoemission process is much faster than the nuclear motion, the final state is created in the initial state geometry, i.e. the nuclei can be considered frozen, according to the Born-Oppenheimer approximation. If the difference in geometry or in the shape of the potential energy curves of the initial and final state is large, different vibrational modes will be excited in the final state with the distribution of the vibrational states being governed by the Franck-Condon principle.
The same phenomenon occuring in XPS of core levels in solids leads to *phonon* excitations and the effect is schematized in fig. 1.4 [13]. As can be seen from the figure, the phonon excitations produce a core level shift and a line broadening, as compared to a vibrationally adiabatic transition.
The origin of such an effect can be appreciated in terms of the equivalent core approximation (ECA, explained in sect. 1.2.2) that assumes the atom with the core hole equivalent to the next atom in the periodic table (also called Z+1 approximation). Due to the Born-Oppenheimer approximation, the photoemission process produces a $Z+1$ element in the geometry of the Z element and this implies that the core ionized atom can be in a state of compression or tension depending on whether the $Z+1$ element is bigger or smaller than the Z counterpart. Therefore the corresponding core level shift and line broadening depend on the size change between the Z and Z+1 atom. The phonon excitations are of intrinsic type as well as they can be extrinsic, i.e. their creation comes from the photoelectron phonon scattering on the photoelectron path inside the solid.
Another phenomenon that can induce phonon excitations is the recoil of the core ionized atom because of the emission of the photoelectron. This is due to the requirement of momentum conservation in the XPS event. It is quite obvious that the recoil energy is bigger for light atoms than for heavier elements. In any case it is always quite small, as demonstrated by the fact that its maximum value for Li is 0.1 eV and 0.01 eV for Rb using at photon energy of 1486 eV obtained with a conventional X-ray source.

1.1.5 Analyzing photoemission spectra

Let's focus now on the procedures used to extract quantitative informations from a photoemission spectrum. In order to do this we need to make a

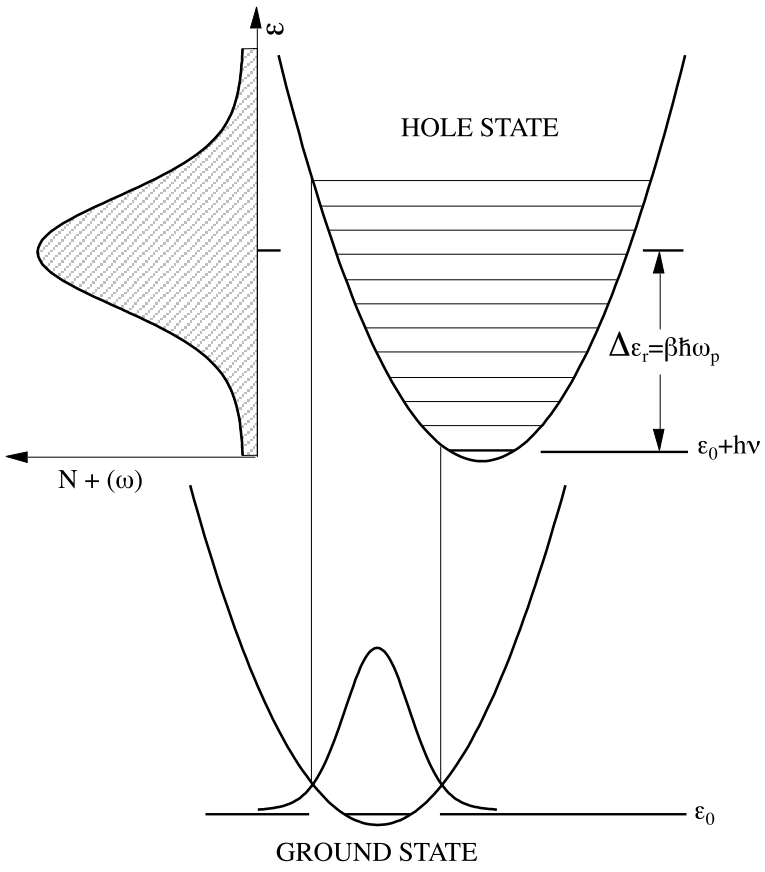

Figure 1.4: Schematic representation of phonon excitation during the photoemission process. The shift in the core level binding energy is $\Delta\epsilon_r$ and is given by the excitation of β phonons of energy $\hbar\omega_p$ [13].

decomposition, i.e. to perform a fit of the measured spectrum with a model line of appropriate line shape and broadening. From here on, only the shape of the main line of the photoemission spectrum will be considered. This line shape can be decomposed into several contributions, the most important being the natural lifetime and the gaussian broadening.

(i) Life time broadening

A photoemission peak has an intrinsic width which is due to the finite lifetime of the core-hole. Its decay can be either radiative or non radiative [14]. These processes involve some of the orbitals that have a lower binding energy than the excited core level. The influence of the chemical surrounding on the decay rate is usually quite small and therefore the intrinsic width is essentially an atomic property.
Considering the Heisenberg's uncertainty principle of eq. 1.8, for τ, life-

time of the core hole, of the order of some 10^{-15} s the peak will have a natural width of 100-200 meV. This broadening, always present in any photoemission spectrum, is described with a Lorentzian distribution (eq. 1.36), whose full width at half maximum (FWHM) is denoted with Γ and E_0 is the position for the maximum intensity I_0

$$I_{Lor}(E_{kin}) = I_0 \frac{\frac{\Gamma}{2\pi}}{(E_{kin} - E_0)^2 + \frac{\Gamma^2}{4}}. \tag{1.36}$$

(ii) Gaussian broadening

The Gaussian broadening of a core level photoemission peak is mainly given by three contributions namely, the experimental energy resolution, the vibrational and inhomogeneous broadening .
The *experimental energy resolution* is due to the fact that the photon source has a finite line width determined by the monochromator used, and the electron energy analyser has a certain resolving power. During the past years this instrumentation has improved considerably. The increased energy resolution allows now to distinguish very fine structures in the spectra . This is a fundamental point to be fullfilled expecially for the experiments that will be presented in this thesis, dealiang with Surface Core Level Shifts that can be as small as 50 meV.
The *vibrational broadening*, in molecules or solids, is given by the excitation of low energy vibrational modes in the final state as explained in sect. 1.1.4. For solids, while multiple phononic losses end up in the low kinetic energy region of the so-called *true* secondary electrons, the intrinsic phonons induce a broadening of the photoemission peaks which can, in most cases, be described by a gaussian distribution [15].
The *inhomogeneous broadening* is due to the presence in the spectrum of unresolved chemical or structural shifted components. These three effects are represented by a gaussian distribution with FWHM, σ,

$$I_{Gaus}(E_{kin}) = I_0 exp\left(- \frac{ln2(E_{kin} - E_0)^2}{\frac{\sigma^2}{4}} \right). \tag{1.37}$$

Doniach-Ŝunjić line-shape

In the case of a metal, the shape of the peak is the convolution of a lorentzian life time broadening, of a gaussian broadening plus an asymmetry due to the creation of electron-hole pairs at the Fermi level. The most commonly used line shape in analyzing photoemission spectra from metals is the *D-Ŝ* line shape calculated by Doniach and Ŝunjić [16]. It is obtained by taking the convolution of a singularity function

$$f(E) \propto \frac{1}{(E_0 - E)^{1-\alpha}} \tag{1.38}$$

representing the core-hole excitation in metals for a constant density of states around the Fermi level at T=0 K, with the Lorentzian broadening of eq. 1.36. The calculated intensity is:

$$I_{DS}(E_{kin}) = I_0 \frac{\Gamma_E(1-\alpha)}{\left((E_0 - E_{kin})^2 + \frac{\Gamma^2}{4}\right)^{\frac{(1-\alpha)}{2}}} \xi(E_{kin}), \tag{1.39}$$

and

$$\xi(E_{kin}) = cos\left[\frac{1}{2}\pi\alpha + (1-\alpha)tan^{-1}\left(2\frac{(E_0 - E_{kin}}{\Gamma}\right)\right] \tag{1.40}$$

where Γ_E is the so-called Γ *function* defined as

$$\Gamma_E(x) = \int_0^\infty t^{x-1}e^{-t}dt, \tag{1.41}$$

α the asymmetry parameter and Γ the FWHM of the lifetime broadening.

The T=0 K approximation implies that there are no electron-hole pair excitations in the neutral ground state. At finite temperature the core-level should exibit additional broadening due to thermal excitations of the conduction electrons. However, this effect is quite small compared to the phonon or lifetime broadening and is well approximated with an additional gaussian broadening. The other approximation, i.e. the constant density of states around the Fermi level, is not always a good approximation, for example in the case of Pt or Pd that have a strong energy dependent density of states close to the Fermi level. In this case a different function have to be used.

In all the studies described in this thesis, dealing with metals like Be, Rh and Ru, the deconvolution of the spectra have been performed using the *D-*$\hat{S}$ line shape, convoluted with a gaussian broadening.

1.1.6 Core-level chemical shifts

So far we have considered the effects of the different kinds of excitations taking place due to the photoemission process, on the XPS line shape. Another important aspect that has to be taken into account in photoemission is that the core levels of an atom are affected by which kind of chemical bond the atom is influenced. This means that the measured core level binding energy depends also on the chemical surroundings of the emitting atom. The binding energy difference of a certain core level in two atoms of the same element but with different chemical surroundings is called *chemical shift*.
The demonstration that the high resolution core level photoelectron spectroscopy technique is a sensitive probe of the chemical environment of the emitting atom was given by Siegbahn and co-workers studying the oxidation of copper [17, 18]. They found that the 1s core level of copper was shifted towards higher binding energy by 4.4 eV on going from metallic copper to

copper oxide. This is because the exact peak position of the core level lines is determined by the oxidation level of the emitting atom and the electric field generated by adjacent atoms [19]. In general, when the emitting atom is bound with a more electronegative ligand, i.e. it undergoes a withdrawal of electrons, its core level electrons are more difficult to excite and appear at higher binding energy in the spectra. This is a quite general behaviour that can be observed on many metal atoms where changes in the oxidation state of the metal are usually accompanied by binding energy shifts towards higher binding energies.
The chemical shifts span an energy range from a few meV to several eV [20], thus enabling an identification of binding partners and a distinction of single or double covalent bonds. An example of the chemical shift is shown in fig. 1.5 for the ethyl-trifluoroacetate $C_4F_3O_2H_5$ molecule for which the C 1s photoemission signal shows four well separated components.
In order to understand the origin of the chemical shift, let's consider again

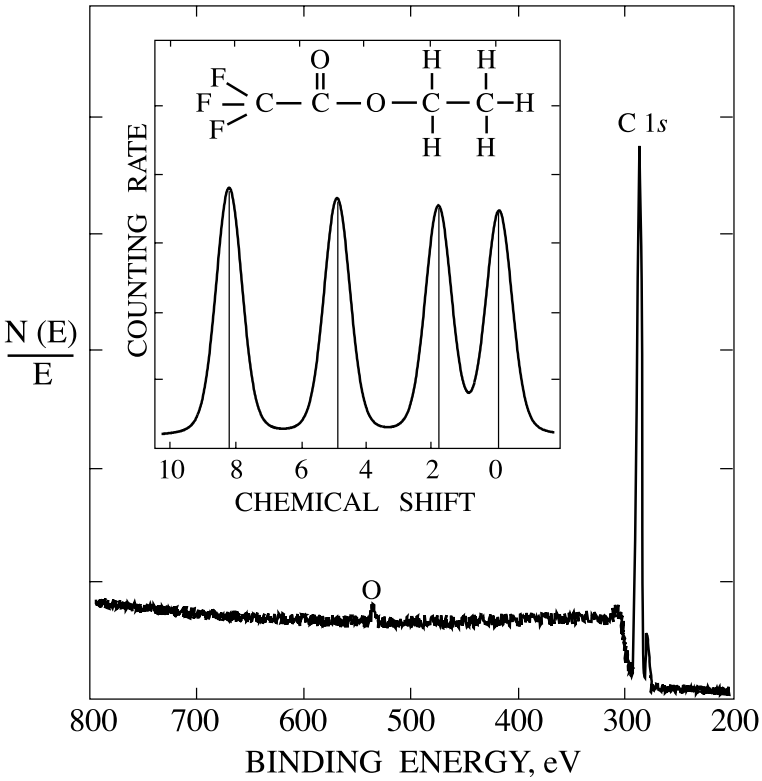

Figure 1.5: Photoemission spectra from $C_4F_3O_2H_5$ molecule. The $C1s$ peak shows four different components related to the carbon atoms bound to different ligands.

eq. 1.7 for the calculation of the binding energy of a core electron. The

chemical shift is given by:

$$\Delta E_b = E^f_{tot,A}(N-1) - E^i_{tot,A}(N) - E^f_{tot,B}(N-1) - E^i_{tot,B}(N) = \Delta^f_{A,B} - \Delta^i_{A,B}, \quad (1.42)$$

where A and B denote the system A and system B respectively and $\Delta_{A,B}$ the total energy difference between the two systems. It is clear then that the chemical shift is not just an initial state effect but one has to take into account also the system with the core-hole, i.e. the final state effects to achieve a good description of such shifts.

1.2 Surface Core Level Shifts

A special type of binding energy shift is that arising between the bulk atoms of a solid and the surface atoms. This shift, named *surface core level shift*, henceforth denoted with SCLS, is caused by the structural environment modification of the atoms at the surface with respect to the bulk. The SCLS's are small compared to the chemical shifts occuring in compounds, since the electronic modifications are not as strong, and therefore the detection of these shifts became possible only by using high energy resolution photoelectron spectroscopy.
The first experimental evidence of such a shift, explained in terms of SCLS, was obtained by Citrin and co-workers in 1978 measuring the Au $4f$ core level of a polycristalline Au clean surface [21]. After that experiment a number of experiments on other systems have been performed trying to elucidate the origin of SCLS's and to predict their width on the basis of theoretical calculations. Moreover, such experiments have been performed not only on clean surfaces but also on adsorbate covered ones. Infact, in presence of an adsorbate, the atoms at the surface change their chemical surrounding and this changes also the SCLS's.
The explanation of the SCLS of a clean surface given by Citrin [21], was that it is related to the lower coordination of the atoms at the surface with respect to the bulk. This causes a narrowing of the valence band thus producing a charge redistribution at the surface and a change in the potential. This potential change is felt by the core electrons that shift in binding energy. This view takes into account only the initial state effects and neglects completely the final state effects that are related to the response of the system to the presence of the core-hole.
Such an approach was further applied by the theoreticians in order to calculate the SCLS's of other metals. In this connection the work of Desjonquéres and co-workers [22] who studied sistematically the SCLS's of a transition series considering only initial state effects, the so-called *microscopic approach* is notable. In parallel to this, other calculations have been performed by

other groups, based on the *thermodynamical approach* which uses a Born-Haber cicle to determine the SCLS's of clean metal surfaces. In the latter approach, also the final state effects, i.e. the screening of the core hole are taken into account. Later on, these two methods of SCLS's calculations have been extended to the case of adsorbate covered surfaces by Tréglia and co-workers [23].
Nowadays, the increased computational speed of the new computers together with the availability of new codes, render it possible to perform *ab-initio* total energy calculations of a many body system. Therefore, considering eq. 1.42, the SCLS is defined as

$$\begin{aligned} \Delta_{\mathrm{SCLS}} &= \left[E^{\mathrm{surface}}(n_c-1) - E^{\mathrm{surface}}(n_c)\right] - \\ &- \left[E^{\mathrm{bulk}}(n_c-1) - E^{\mathrm{bulk}}(n_c)\right] \quad , \end{aligned} \tag{1.43}$$

where $E^{\mathrm{surface/bulk}}(n_c)$ is the total energy of the system considered as a function of the number of electrons, n_c, in a particular core level, c, of a surface or bulk atom respectively [13, 24]. These calculations permit to distinguish between initial and final state contributions to the SCLS's and are able to reproduce the measured SCLS's with high accurancy.
This thesis deals with SCLS's of clean as well as adsorbate covered surfaces. Therefore a detailed explanation of the methods used to calculate such shifts is given in the following.

1.2.1 Microscopic model

Let's consider again eq. 1.43 and expand the total energies as

$$E(n_c - \delta n_c) = E(n_c) - \frac{\partial E(n_c)}{\partial n_c}\delta n_c + \frac{1}{2}\frac{\partial^2 E(n_c)}{\partial n_c^2}(\delta n_c)^2 + \dots \tag{1.44}$$

where the derivative equals the orbital eigenenergy,

$$-\frac{\partial E(n_c)}{\partial n_c} = \epsilon_c(n_c). \tag{1.45}$$

If we put eq. 1.44 into eq. 1.43 we obtain the SCLS expressed as

$$\Delta_{\mathrm{SCLS}} = -(\epsilon_c^{surface}(n_c) - \epsilon_c^{bulk}(n_c)) - \frac{1}{2}\frac{\partial}{\partial n_c}\epsilon_c^{bulk} + \frac{1}{2}\frac{\partial}{\partial n_c}\epsilon_c^{surface} + \dots, \tag{1.46}$$

or

$$\Delta_{\mathrm{SCLS}} = \Delta_{\mathrm{SCLS}}^{conf-chem} + \Delta_{\mathrm{SCLS}}^{relax}, \tag{1.47}$$

where

$$\Delta_{\mathrm{SCLS}}^{conf-chem} = -(\epsilon_c^{surface}(n_c) - \epsilon_c^{bulk}(n_c)), \tag{1.48}$$

and

$$\Delta_{\mathrm{SCLS}}^{relax} = -\frac{1}{2}\frac{\partial}{\partial n_c}\epsilon_c^{bulk} + \frac{1}{2}\frac{\partial}{\partial n_c}\epsilon_c^{surface} + \dots. \tag{1.49}$$

From eq. 1.47, neglecting the derivatives, we find that the SCLS is simply given by $\Delta_{\mathrm{SCLS}}^{conf-chem}$ which is the variation of the orbital eigenenergies caused by the change of the electronic configuration and of the chemical environment between the surface and the bulk in the initial state. This is the Koopman's theorem.
The derivative terms, $\Delta_{\mathrm{SCLS}}^{relax}$, take into account for all the effects that are not included in Koopmans' theorem like the correlation and screening effects. The first ones do not change much when going from the surface to the bulk atoms [25], and therefore the latter are the most important.
Moreover, the screening can be either intraatomic, i.e. due to the relaxation of the electrons of the emitting atom, or interatomic that involves the electrons of the other atoms. The difference in intraatomic screening between the surface and the bulk can be neglected since this screening is almost the same for an atom free or embedded in the bulk [25]. Moreover, also the contribution of the interatomic screening to the SCLS is quite small because, considering transition metals, it is due to the d electrons that are still quite localized and most probably not much affected by the presence of the surface. In this way we end up with the SCLS given by the simple expression

$$\Delta_{\mathrm{SCLS}} = -(\epsilon_c^{surface}(n_c) - \epsilon_c^{bulk}(n_c)) \tag{1.50}$$

This is the *initial state* description of the SCLS's, in which the screening effects are not taken into account.
Let's give now a qualitative explanation of the SCLS's as calculated with eq. 1.50. In order to do this, we need to understand how the shifts of the core levels are related to those of the valence d levels.
By considering the model of ref. [26], and approximating the d orbitals by a spherical shell with radius R and with N_d electrons, the Hartree potential energy inside the sphere is given by

$$V = e^2 \frac{N_d}{R}. \tag{1.51}$$

Therefore any change in N_d is reflected in the potential through the eq. 1.51: this potential change is felt by the core levels, which are inside the sphere, and their energy shifts accordingly.
When, on the contrary, the d orbitals are not totally confined on the spherical shell, then, most probably, the deeper core levels should display the stronger energy shift because they are confined in a more localized region around the nucleus. A more detailed calculation of the effect of a small change of the number of valence electrons on the energy of different levels, have been performed within the model of ref. [27]. As an example, for Rh, that is one of the metals whose SCLS is discussed in this thesis, by changing the number of $4d$ electrons by 0.08 and $4s$ by 0.02, the shift of the $3d$ core level is 1.56 eV while that of the $4d$ valence band is 1.36 eV. From these results

the SCLS of eq. 1.50 can be written as a function of the centre of gravity, so-called *centroid* ϵ_d, of the valence d band

$$\Delta_{\mathrm{SCLS}} \simeq -1.1(\epsilon_d^{surface} - \epsilon_d^{bulk}). \tag{1.52}$$

In the tight binding theory framework, a change in the potential of the surface atoms is reflected in a shift of the same amount of the valence band centroid.
With all these information we can now develop a qualitative picture of the SCLS, for which a schematic representation is shown in fig. 1.6 for a d band less and more than half full respectively [28]. Here the d band of a transition

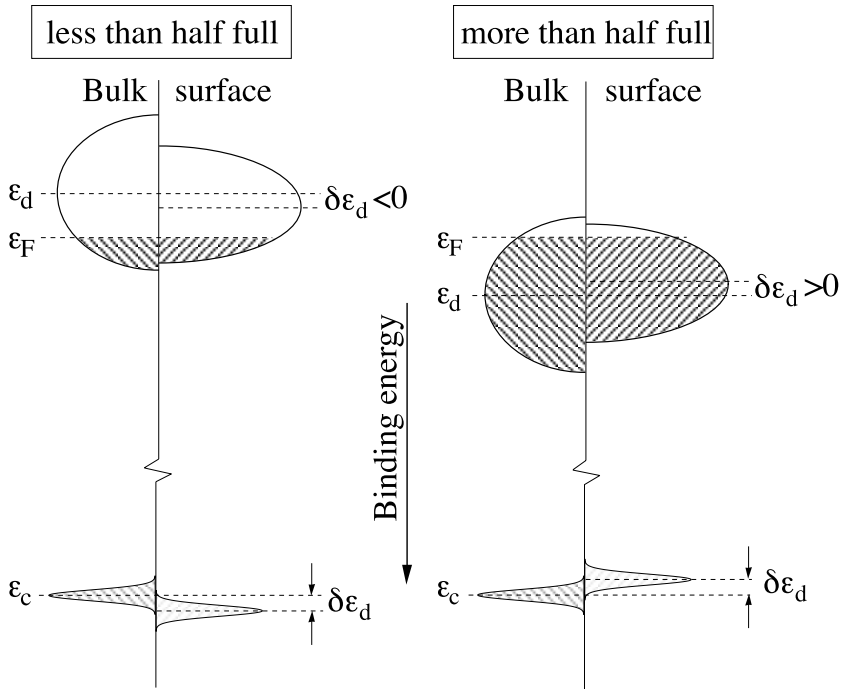

Figure 1.6: Schematic representation of the SCLS caused by d-band narrowing and an electrostatic shift for transition metals. On the left the d-band is less than half full while on the right it is more than half full [3].

metal is approximated with a symmetric distribution around a central value. The difference between surface and bulk atoms is that the former have a narrower distribution of the band due to their lower coordination. Therefore a charge rearrangement is needed in order to maintain a common Fermi level between the bulk and surface atoms, i.e. electrons will flow from the bulk to the surface in the case of a band more than half full and the opposite happens in the case of a band less than half full. This gives rise to an electrostatic potential difference $\delta\epsilon_d$ that shifts rigidly both the valence band centroid and the deep core levels of the surface atoms. This shift is towards higher

(lower) binding energies for a d band less (more) than half full.
From all the above considerations it follows that the SCLS of a transition metal series should parallel the occupation number of the valence d band. Moreover, the more the band narrows, the stronger should be the SCLS. Since the narrowing is due to the number of cut bonds at the surface, the fcc metals for example should display an increasing SCLS moving from the (111) (3 cut bonds) to the (100) (4 cut bonds) and to the (110) (5 cut bonds) surfaces.
This effect has been calculated within the tight-binding theory framework and the derived expression for the SCLS of the $4d$ transition metal series is:

$$\Delta_{\mathrm{SCLS}} = \left(\sqrt{\frac{Z_{surface}}{Z_{bulk}}} - 1\right)\left(\frac{n_d - 5}{10}\right)W_d \tag{1.53}$$

where $Z_{surface/bulk}$ are the coordination numbers of the surface/bulk atoms

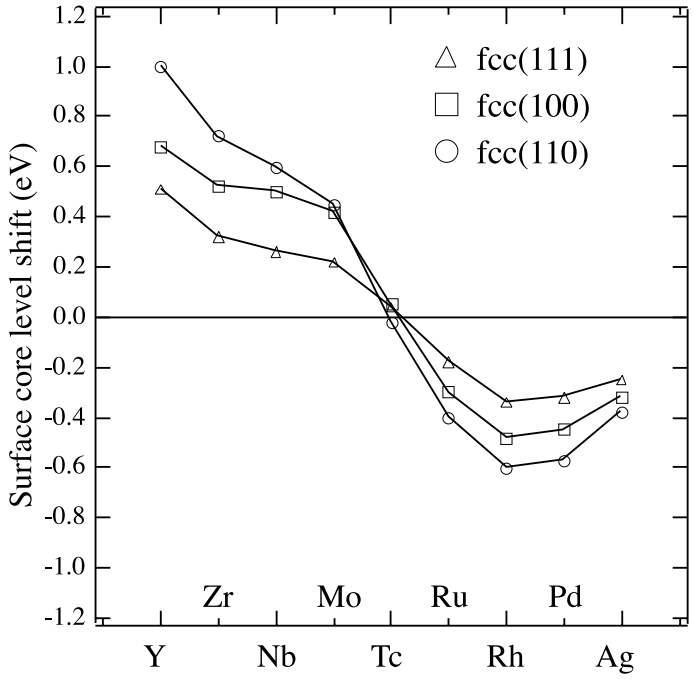

Figure 1.7: *Ab-initio* calculations of the initial state SCLS's of the $1s$ state of the 4d transition metal series. All metals have been treated as fcc and the SCLS's have been calculated for all the three low index surfaces. The SCLS's of the $3d$ core states are lower by ≈ 0.02 eV at the ends of the series and by ≈ 0.08 eV near the middle.

and n_d and W_d are the d band occupation number and width, respectively [29].
A more detailed analysis of the initial state SCLS's of the $4d$ transition

metals has been done by performing *ab-initio* calculations of the SCLS; the results are shown in fig. 1.7 [30].
These calculations confirm the above conclusions on the SCLS, even though the behaviour of the variation of the SCLS is not monotonic along the series. This is due to the fact that the shape of the d band is not as simple as depicted in fig. 1.6 but it presents also sharp peaks. When the Fermi level is found in a peak of the bulk band, the SCLS variation decreases.
Another important aspect to be noted is that the eq. 1.53 can be used to normalize the surface dependent SCLS's of fig. 1.7. The result of such a normalization is that the curves are almost superimposed. This means that tight binding calculations give a good estimation of the narrowing of the d band when bonds are cut.

1.2.2 Thermodynamic model

As explained in the previous section, the microscopic approach considers the SCLS's just within the initial state approximation and does not take into account the final state effects due to the screening of the core-hole. These effects can be quite large, as will be shown for example in sections 5.1 and 5.2 and therefore the theoretical calculations need to take into account all the effects involved in order to describe accurately the properties of the system that determine the SCLS's. The first theoretical approach that was used in this sense is the so-called *thermodynamic approach* [31, 32] which uses an expression based on different Born-Haber cycles for the surface and bulk atoms. These cycles connect the same initial state with two different final states, one with the core-hole located at the surface and the other with the core hole located in the bulk.
The basic assumption of this approach is that the core ionized state is an electronically completely screened final state where the conduction electrons have attained a fully relaxed configuration in presence of the core-hole.
Moreover, a further approximation is made, the so called *equivalent core approximation* (ECA) to describe the system with the core hole. Within this approximation the core electrons are assumed to be located entirely inside the valence electrons. In this way it is reasonable to assume that the removal of a core electron is felt by the valence electrons as a change in the nuclear charge from Z to Z+1. Therefore the properties of the core ionized atom are the same as the next element in the periodic table [33].
Each Born-Haber cycle can be sketched as follows (see fig. 1.8 for the bulk case): consider a Z metal, sublimate it, ionize one of the sublimated atoms and screen the created core hole then condensate again all the remaining atoms including the Z+1 impurity. The resulting metal will be, in one case a Z metal with a Z+1 impurity at the surface and in the other, a Z metal with a Z+1 impurity in the bulk. Therefore, since the SCLS is the difference between the energies in the two cases, the energies on atomic level related to

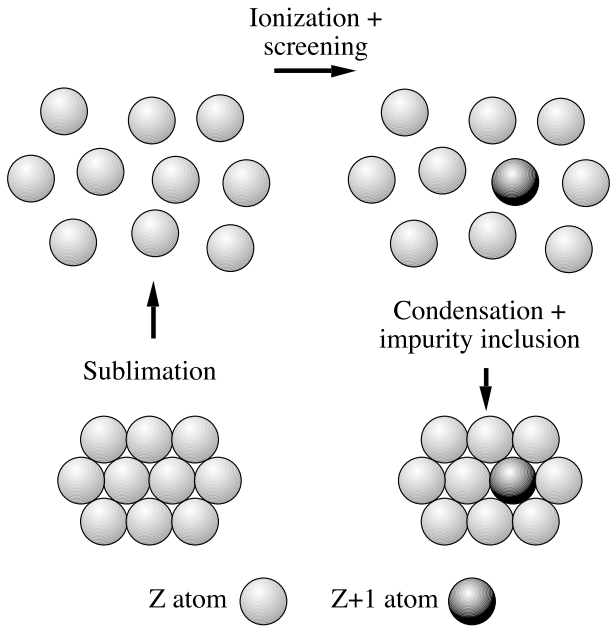

Figure 1.8: Schematic representation of a Born-Haber cycle for the ionization of a bulk atom [24].

the screening will cancel each other. The terms that survive are only those corresponding to the way in which the ionized atom bonds to the lattice before and after the ionization process at the surface and in the bulk.

$$\Delta_{\mathrm{SCLS}} = \left(E_{coh}^{Z+1} + E_{imp}^{Z+1}(Z) - E_{coh}^{Z}\right)^{surf} - \left(E_{coh}^{Z+1} + E_{imp}^{Z+1}(Z) - E_{coh}^{Z}\right)^{bulk}$$
$$= E_{Z\to Z+1}^{surf} - E_{Z\to Z+1}^{bulk} \tag{1.54}$$

where E_{coh} is the cohesive energy, i.e. the energy gained when transforming a free atom into a bulk atom, $E_{imp}^{Z+1}(Z)$ is the solution energy of a Z+1 atom in the Z metal, $E_{Z\to Z+1}^{surf/bulk}$ is the energy required to substitute a Z with a Z+1 atom at the surface/bulk. This is sketched in fig. 1.9. This energy difference corresponds to the surface segregation energy of the core ionized atom in a Z matrix $\Delta U_{Z+1}(Z)$ [34]. Therefore the SCLS is given by

$$\Delta_{\mathrm{SCLS}} = \Delta U_{Z+1}(Z). \tag{1.55}$$

If we consider again eq. 1.54 and we neglect the impurity contribution $E_{imp}^{Z+1}(Z)$ we find

$$\Delta_{\mathrm{SCLS}} = \left(E_{coh}^{Z+1,surf} - E_{coh}^{Z+1,bulk}\right) - \left(E_{coh}^{Z,surf} - E_{coh}^{Z,bulk}\right)$$
$$= E_{surf}(Z+1) - E_{surf}(Z) \tag{1.56}$$

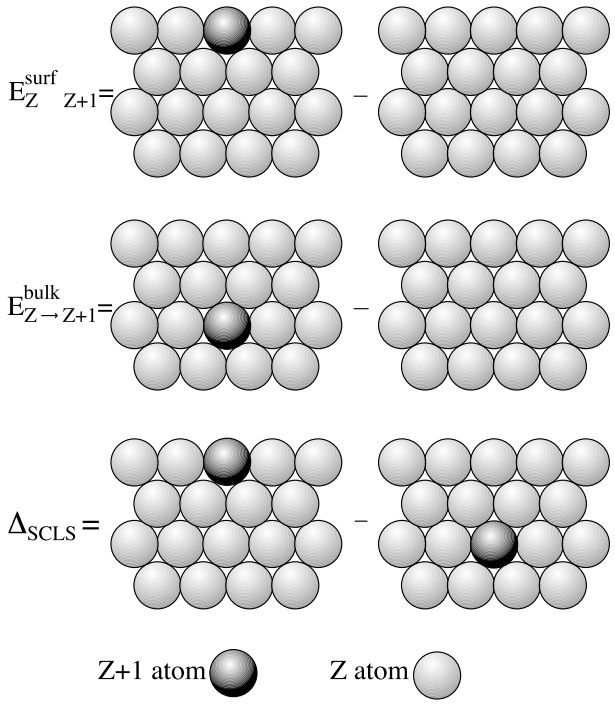

Figure 1.9: Schematic representation of the SCLS whithin the thermodynamic model as explained in eq. 1.54. The dark atom is a fully screened core ionized atom that in the ECA approximation is a Z+1 atom [13].

where E_{surf} is the surface energy, i.e. the variation of energy per surface atom due to the creation of the surface.
In order to attein a qualitative understanding of eq. 1.56 let's write the surface energy as a function of the cohesive energy, using the empirical relation $E_{surf} \simeq 0.2E_{coh}$, which holds roughly for all the elements, provided that the same surface structure is considered

$$\Delta_{\mathrm{SCLS}} = 0.2\Big(E_{coh}(Z+1) - E_{coh}(Z)\Big). \tag{1.57}$$

With this equation in mind it is quite simple to explain the behaviour of the SCLS along the $5d$ transition metal series, for which different determinations of eq. 1.56 [31, 32, 35] agree quite well with the experimental results [36]. Infact, for the $5d$ metals the cohesive energy is mainly due to the $5d$ electrons whose density of states can be occupied by 10 electrons per atom. Considering the first element of the series, only the bonding states are occupied and the occupation of these states increases moving to the middle of the series, thus increasing the cohesive energy. From the middle to the late elements, antibonding states become occupied thus reducing the cohesive energy. This behaviour, introduced in eq. 1.57, explains why the SCLS's of $5d$ transition elements are positive (towards higher binding energy) for the

early elements of the series and negative for the late ones [37].
Thinking in the opposite way, the knowledge of the SCLS's can give useful informations on the process of surface segregation of alloys formed with adjacent atoms in the transition metal row. Infact, from eq. 1.55 and considering for example the SCLS's experimental results of ref. [36] for the $5d$ transition metals, it turns out that on the left (right) side of the row the Z-1 (Z+1) atom will segregate on the surface of an alloy formed with Z atoms, because of the positive (negative) SCLS's. This rule can be generalized to alloys formed with elements that are not adjacent in the periodic table.
The thermodynamic approach, as explained in this section, is quite general, in the sense that it can be applied to all the elements and, most important, takes into account for the screening effects. However with this method it is possible to calculate only the SCLS's of the top layer atoms because the generalization of the thermodynamic approach to the calculation of the SCLS's of subsurface layers would introduce energies that are not measurable.

1.2.3 $Ab-initio$ calculations

The methods outlined in sect. 1.2.1 and 1.2.2 to calculate the SCLS's, are based on approximations that limit their applicability to some selected systems. They permit however to understand the physical reasons of the SCLS's.
In order to make an exact calculation of the SCLS's, it is necessary to determine the total energies for the bulk and surface ionized states, to be put into eq. 1.43. Nowadays these energies can be computed by performing $ab-initio$ calculations within the density functional theory framework. This kind of calculations have been performed by different theoretical groups (more details are found in chapters 3, 4, 5) to explain the SCLS's that we have measured on different systems and we are going to present. Therefore in the following we enphasize the most important aspects of a total energy calculation just to appreciate the theoretical improvements that have been done in the last decades, which allow now to understand more deeply the physics of SCLS's for a variety of systems, as shown in the following chapters.

Born-Oppenheimer approximation

A crystal is composed by many atoms (10^{23} or so) arranged in an ordered structure. In order to calculate the wave function of such a complex system, all the p nuclei, located at $\mathbf{R}_1, \ldots, \mathbf{R}_p$ as well as all the N electrons, located in $\mathbf{r}_1, \ldots, \mathbf{r}_N$ and with spin $\mathbf{s}_1, \ldots, \mathbf{s}_N$ must be taken into account. This is a so-called *many body problem* and its wave function

$$\Psi_{tot}(N) = \Psi_{tot}(\mathbf{r}_1, s_1, \ldots, \mathbf{r}_N, s_N; \mathbf{R}_1, \ldots, \mathbf{R}_p). \tag{1.58}$$

obeys the time independent Schrödinger equation

$$\hat{H}_{tot}|\Psi_{tot}>=E_{tot}|\Psi_{tot}> . \tag{1.59}$$

The Hamiltonian $\hat{H}_{tot}$ contains the kinetic terms of the electrons and of the nuclei, the electron-nucleus and the nucleus-nucleus interaction and finally the electron-electron interaction.
In general the wave function 1.58 cannot be determined exactly due to the exceedengly high number of bodies and to the nature of the interactions between them. Very sophisticated approximations have been developed in the years that allow to find a solution to these problems.
The first approximation introduced is the *Born-Oppenheimer* approximation [38] that decouples the motion of the nuclei from that of the electrons. This means that the total energy of a given nuclear configuration can be calculated by minimizing the energy of the electrons in the constant external potential of the nuclei. In this way the kinetic term of the nuclei can be regarded as zero. This means that the nucleus-nucleus interaction will be constant and therefore the total energy of the system can be obtained just by adding the electronic energy E to the nucleus-nucleus repulsion. This term can be therefore excluded from the hamiltonian of the N electrons system. We are then left with the Schrödinger equation

$$\hat{H}|\Psi>=E|\Psi> \tag{1.60}$$

where $\Psi=\Psi(\mathbf{r}_1,s_1,\ldots,\mathbf{r}_N,s_N)$ and the Hamiltonian is given by

$$\hat{H}=\hat{T}+\hat{U}+\hat{W}. \tag{1.61}$$

Here $\hat{T}$ is the kinetic energy operator

$$\hat{T}=-\frac{1}{2}\sum_{i=1}^{N}\nabla_i^2, \tag{1.62}$$

$\hat{U}$ represents the interaction of the electrons with the coulombic field from the nuclei of charge Z_α

$$\hat{U}=\sum_{i,\alpha}^{N,p}\frac{Z_\alpha}{|\mathbf{r}_i-\mathbf{R}_\alpha|}, \tag{1.63}$$

and $\hat{W}$ is the two particle interaction operator

$$\hat{W}=\sum_{i,j>i}^{N,N}\frac{1}{|\mathbf{r}_i-\mathbf{r}_j|}. \tag{1.64}$$

In order to determine the ground state energy of the system, eq. 1.60 must be solved, within the constrain $<\Psi|\Psi>=1$. The equivalent *variational*

form of the Schrödinger equation states that a solution of 1.60 is any state that satisfies

$$< \hat{H} >_{\Psi} = \frac{< \Psi | \hat{H} | \Psi >}{< \Psi | \Psi >} \Rightarrow Stationary, \tag{1.65}$$

and the ground state of the system is that represented by the wave function that minimizes 1.65.
Let's see now how the wave function Ψ can be approximated in order to solve 1.65.

Hartree-Fock approximation

Whitin the Hartree-Fock approximation, the wave function of the N electrons system Ψ is the sum of N! antisymmetrized products of N single electron orbitals $\psi_i(\mathbf{r}_j, s_j)$, given by a Slater determinant

$$\Psi_{HF} = \left(\frac{1}{N!}\right)^{\frac{1}{2}} \begin{vmatrix} \psi_1(\mathbf{r}_1, s_1) & \dots & \psi_N(\mathbf{r}_1, s_1) \\ \psi_1(\mathbf{r}_2, s_2) & \dots & \psi_N(\mathbf{r}_2, s_2) \\ \vdots & \ddots & \vdots \\ \psi_1(\mathbf{r}_N, s_N) & \dots & \psi_N(\mathbf{r}_N, s_N) \end{vmatrix}. \tag{1.66}$$

The wave function Ψ_{HF} is antisymmetric and satisfies the Pauli exclusion principle because when two electrons are in the same state, i.e. they have the same orbitals, two columns are identical and Ψ_{HF} becomes zero.
By using now this wave function into 1.65, with the Hamiltonian of eq. 1.61 it is possible to determine the energy E_{HF}. To find this solution the eigenvalue equation for each electron quantum state must be solved, with a potential for each state. Since the potential is not known and depends on the wave function itself, the problem must be solved recursively by a self-consistent method. This means that one guesses the single particle wave-function, calculates the potential and uses this potential to recalculate the wave function, until the new wave function does not differ from the previous one. This method is called *Self Consistent Field* (SCF) method.
The energy obtaind in this way, E_{HF}, is given by

$$E_{HF} = T_{HF} + U_{HF} + W_{HF} \tag{1.67}$$

were $T_{HF} =< \Psi_{HF} | \hat{T} | \Psi_{HF} >$ and $U_{HF} =< \Psi_{HF} | \hat{U} | \Psi_{HF} >$.
The last term W_{HF} is the electron-electron interaction energy. This energy is the sum of two different contributions: the first one, called *Hartree energy*, is the result of the interaction between the electron i with the charge density created by all the other electrons, that include also the electron i itself and, the second, called *exchange term* that corrects this last effect, i.e. the fact that the electron cannot act with a Coulomb force on itself.
The wave function Ψ_{HF} is just an approximation of the true wave function Ψ of the N electrons system and therefore also the energy calculated E_{HF}

is not the exact ground state energy E of eq. 1.60. This is because of the way in which Ψ_{HF} is defined, i.e. as a superposition of one electron wave functions, which means that the electrons are thought as indipendent particles. The exact energy of the ground state is therefore given by

$$E = E_{HF} + E_c \tag{1.68}$$

where E_c is the so-called *correlation energy*. Therefore, the calculation of the total energy is again very difficult to perform because, while the E_{HF} is relatively simple to compute, the E_c is not, because it represents all the effects that are not included when introducing the Slater determinant. In order to overcome this problem, another approach to the solution of a many body problem has been adopted, namely the *density functional theory* (DFT). Whithin this theory, the energy is not considered as an eigenvalue of a certain wave function but as a functional of the electron density $\rho(\mathbf{r})$.

Density functional theory

The DFT is based on three theorems [39, 40, 41].
The first theorem states that the ground state expectation value of any observable is a unique functional of the ground state electron density $\rho^0(\mathbf{r})$. In other words, the density $\rho^0(\mathbf{r})$ determines all the properties of the ground state and therefore also the total energy, that now can be written, following the notation adopted in eq. 1.61 as

$$E[\rho^0] = T[\rho^0] + U[\rho^0] + W[\rho^0], \tag{1.69}$$

i.e. the energies T, U and W are all functionals of the electron density.
The second theorem is the variational principle and states that for any charge density $\rho(\mathbf{r})$, of N electrons, the total energy $E[\rho]$ has a minimum in the ground state, i.e.

$$E[\rho^0] \leq E[\rho]. \tag{1.70}$$

At this point it would be possible to solve eq. 1.69 but the only functional that is known exactly is $U[\rho]$ and both $T[\rho]$ and $W[\rho]$ are not known. We can therefore write eq. 1.69 as

$$E[\rho^0] = F[\rho^0] + \int V(\mathbf{r})\rho^0(\mathbf{r})d\mathbf{r} \tag{1.71}$$

where $V(\mathbf{r})$ is the external potential and $F[\rho^0]$ includes the kinetic energy and the electron-electron interaction.
The third theorem states that $F[\rho]$ is universal, i.e. it has the same analytical form for all the systems and does not depend on the external potential V. Therefore the analytical form of $F[\rho]$ is needed in order to solve the many body problem. In order to find this, Kohn and Sham reintroduced the one-electron orbitals of non-interacting electrons $\psi_i(\mathbf{r})$, giving the same ground

state density of the interacting system $\rho^0(\mathbf{r})$ (so-called Kohn-Sham orbitals), instead of the electron density. In this way the expectation value of the kinetic energy operator is the kinetic energy of a non-interacting electron gas $T_0[\rho]$, and the electron-electron interaction $W[\rho]$ contains the ordinary Coulomb repulsion term, or Hartree term $H[\rho]$ plus an unknown term, called exchange and correlation term $E_{xc}[\rho]$. We have therefore

$$F[\rho] = T_0[\rho] + H[\rho] + E_{xc}[\rho]. \tag{1.72}$$

By applying the variational principle, stated in the second theorem described before, to the Kohn-Sham orbitals, the following set of equations results

$$\hat{H}_{KS}\psi_i(\mathbf{r}) = \epsilon_i\psi_i(\mathbf{r}) \tag{1.73}$$

where $i = 1, \ldots, N$, ϵ_i are the Kohn-Sham eigenvalues and

$$\hat{H}_{KS} = -\frac{1}{2}\bigtriangledown^2 + V_{eff}(\mathbf{r}), \tag{1.74}$$

where $V_{eff}(\mathbf{r})$, the effective potential that the independent particles move in, is defined as

$$V_{eff}(\mathbf{r}) = V(\mathbf{r}) + \int \frac{\rho(\mathbf{r}')}{|\mathbf{r} - \mathbf{r}'|} d\mathbf{r}' + V_{xc}(\mathbf{r}; [\rho]). \tag{1.75}$$

The $V_{xc}(\mathbf{r}; [\rho])$ is the unknown exchange-correlation potential, which is a functional of the density ρ. It is a non-local function because its value in a point $\mathbf{r}$ depends on the density in all the space. The equations 1.73 are non-linear and therefore they must be solved recursively or in a self-consistent way. The resulting electron density will be

$$\rho(\mathbf{r}) = \sum_{i=1}^{N} |\psi_i(\mathbf{r})|^2 \tag{1.76}$$

and the corresponding ground state energy will be given by eq. 1.71.
The most problematic term remains the exchange-correlation energy functional $E_{xc}[\rho]$ that must be approximated.

Local Density Approximation

One way of treating the $E_{xc}[\rho]$ is by applying the Local Density Approximation (LDA). Within this approximation, the $V_{xc}(\mathbf{r}; [\rho])$, which is in general a non local function, becomes local, in the sense that it depends only on the electron density at point $\mathbf{r}$

$$V_{xc}(\mathbf{r}; [\rho] \cong V_{xc}^{LDA}(\mathbf{r}; \rho(\mathbf{r})). \tag{1.77}$$

This is achieved by defining an exchange and correlation energy per particle of a homogeneous electron gas with density $\rho(\mathbf{r})$, $\epsilon_{xc}(\rho(\mathbf{r}))$, and the corresponding $E_{xc}[\rho]$ becomes

$$E_{xc}^{LDA}[\rho] = \int \rho(\mathbf{r})\epsilon_{xc}(\rho(\mathbf{r}))d\mathbf{r}. \tag{1.78}$$

Various methods are used in order to determine the $\epsilon_{xc}(\rho(\mathbf{r}))$. Once this function is available it is possible to solve eq. 1.73 and then to find the total energy of the system.
In principle the LDA should be suitable only for systems in which the electron density varies slowly, even though it works well also for systems with relatively large density gradients. In any case, in order to treat this kind of systems, a more advanced approximation must be considered.

Generalized Gradient Approximation

In the Generalized Gradient Approximation (GGA) [42] the electron density gradient is included in the definition of $V_{xc}(\mathbf{r};[\rho])$ that becomes

$$V_{xc}(\mathbf{r};[\rho] \cong V_{xc}^{GGA}(\mathbf{r};\rho(\mathbf{r}),\bigtriangledown\rho(\mathbf{r})). \tag{1.79}$$

The corresponding exchange energy can be written as

$$E_{xc}^{GGA}[\rho^{\alpha},\rho^{\beta}] = \int f(\rho^{\alpha},\rho^{\beta},\bigtriangledown\rho^{\alpha},\bigtriangledown\rho^{\beta})d(\mathbf{r}). \tag{1.80}$$

Also in this case, as for the LDA, many exchange and correlation functionals have been proposed.

Wave function expansion

In order to solve the Kohn-Sham equations of eq. 1.73, the one electron orbitals $\psi_i(\mathbf{r})$ are often expanded in a set of basis functions $\{\phi_j(\mathbf{r})\}$. For a complete basis set the wave function $\psi_i(\mathbf{r})$ can be expressed as

$$\psi_i(\mathbf{r}) = \sum_j c_{i,j}\phi_j(\mathbf{r}), \tag{1.81}$$

and the summation is over an infinite number of coefficients and basis functions. In order to perform a real calculations it is therefore necessary to construct basis functions well suited for the problem and consider just a finite sum of them, because the larger the basis set is, the higher computational effort is needed.
One of the methods that is widely adopted to solve the Kohn-Sham equations is the so-called *Full Potential Linearized Augmented Plane Wave* method (FP-LAPW) [43, 44, 45]. In this case the unit cell is divided into non overlapping muffin-tin spheres that are centered at the atomic sites, and

an interstitial region. Two different basis sets are used in each region. In particular inside the atomic spheres, a linear combination of radial functions times spherical harmonics is used, while in the interstitial region a plane wave expansion is adopted. At this point the calculation can be done recursively until self consistency is achieved.

1.2.4 SCLS's total energy calculations

Let's consider again the eq. 1.43 where the SCLS Δ_{SCLS} is expressed as the difference in energy which is needed to remove a core electron either from a surface or from a bulk atom.

Within the initial state approximation the SCLS, $\Delta^{\mathrm{initial}}_{\mathrm{SCLS}}$, is given by eq. 1.50, i.e.

$$\Delta^{\mathrm{initial}}_{\mathrm{SCLS}} \approx -\left[\epsilon_c^{\mathrm{surface}}(n_c) - \epsilon_c^{\mathrm{bulk}}(n_c) \right] \quad . \tag{1.82}$$

Now $\epsilon_c^{\mathrm{surface}}$ and $\epsilon_c^{\mathrm{bulk}}$ do not represent anymore the Hartree Fock eigenvalues but the Kohn-Sham eigenvalues of the particular core state, c. In this approximation the SCLS is simply due to the variation of the orbital eigenenergies before the excitation of the core electron.
A full calculation of the ionization energy, which includes the screening contributions from the valence electrons in response to the created core hole, can be achieved by calculating the total energy of an impurity with a core hole in the selected core state. The SCLS is then the difference of two total energies, with the impurity once located at the surface and once inside the bulk, as shown in fig. 1.9 within the ECA approximation [31]. To a good approximation, this difference can also be obtained via the Slater-Janak transition-state approach of evaluating total energy differences [46]. Using the mean value theorem of integration,

$$\begin{aligned} E(n_c - 1) - E(n_c) &= \int_{n_c}^{n_c - 1} \frac{\partial E(n')}{\partial n'} dn' \approx \\ &\approx -\epsilon_c(n_c - 1/2) \quad , \end{aligned} \tag{1.83}$$

the $\Delta^{\mathrm{initial}}_{\mathrm{SCLS}}$ can be cast into the form of eq. 1.82, yet this time with a core level occupation of $n_c - 1/2$ i.e.

$$\Delta_{\mathrm{SCLS}} \approx -\left[\epsilon_c^{\mathrm{surface}}(n_c - 1/2) - \epsilon_c^{\mathrm{bulk}}(n_c - 1/2) \right] \quad . \tag{1.84}$$

Note that this latter approach, from which we derive the total SCLS, takes both initial and final state effects (in the spectroscopic sense) into account, so that the results of such a calculation can be compared with the experimental values.

1.3 Photoelectron diffraction

The intensity of a core level photoemission peak at a certain photon energy is proportional to the integral over the solid acceptance angle of the electron detection system, of the photoelectric cross section defined in paragraph 1.1.1 and to the number of emitters. In case of photoemission from solids there are however other effects that determine the intensity like the elastic and inelastic scattering events that take place during the transport of the photoelectrons from the emitters to the vacuum. The former cause a lowering of the photoemission signal when the emitters are found in deeper layers, due to the inelastic mean free path of the photoelectrons in solids while the latter, called photoelectron diffraction effects, can either give a lowering or an increase of the photoemission signal depending on the geometry around the emitter, the photoelectron kinetic energy and the detection angle.
A schematic picture of the photoelectron diffraction effect is shown in fig. 1.10.

In a photoelectron diffraction experiment a core electron is excited by an

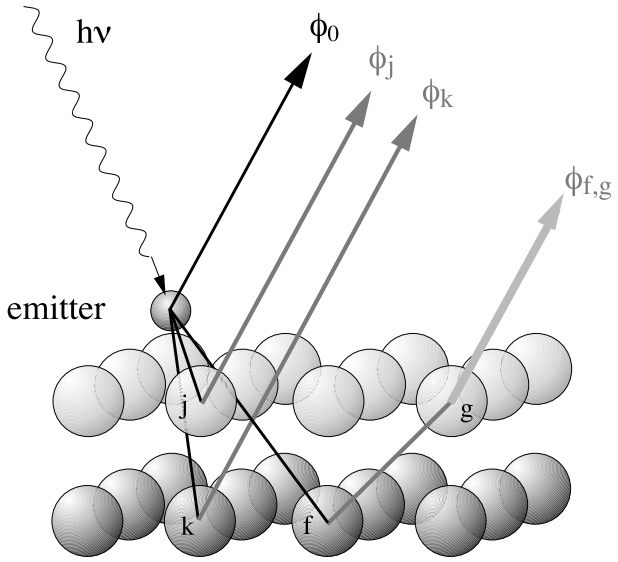

Figure 1.10: Schematic representation of the photoelectron diffraction effect. The primary wave ϕ_0 is generated by the photoemission process of the atom adsorbed on top of the surface of a crystal. The secondary waves ϕ_j, ϕ_k are the singly scattered waves by the atoms j , k of the surface and subsurface layers respectively. A double scattered wave $\phi_{f,g}$ is also shown.

x-ray photon. The outgoing electron wave ϕ_0 can reach the electron detector on a direct path or it can be scattered by the atoms surrounding the emitter, generating the waves ϕ_j, ϕ_k and $\phi_{f,g}$ that interfere with the direct wave producing a diffraction pattern characteristic for each emitter. The final

diffraction intensity can then be measured as a function of the azimuthal or polar emission angles or, at fixed emission angles but as a function of the photon energy, as shown in fig. 1.11. As the photoelectron undergoes

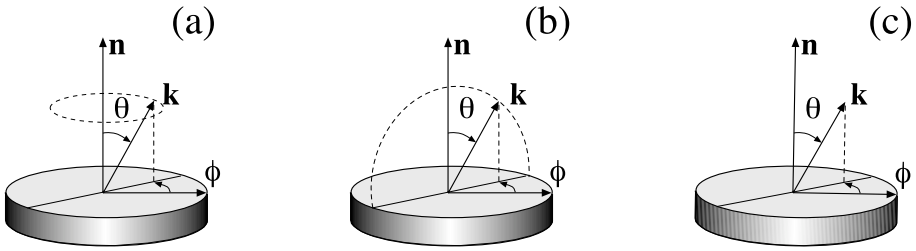

Figure 1.11: Three different modes to perform photoelectron diffraction: (a) azimuthal scan, (b) polar scan and (c) photon energy scan (k varying).

the scattering process, it collects informations on the local surroundings. In order to extract such informations the measured interference pattern has to be compared with multiple scattering calculations performed for a model structure.
The photoelectron diffraction technique combines therefore chemical, structural and surface sensitivity and the structural characterization it gives is *local* because of the inelastic effects. Moreover, since different atoms hit by the incident light act as time uncorrelated photoemitters and their intensities add up incoherently, there is no need to have long range order in order exploit the photoelectron diffraction technique.

An often used way to consider the photoemission process, including the elastic and inelastic scattering effects, is the *three step model* in which the photo absorption, the transport of the photoelectron from the emitter to the surface and its propagation from the surface to the detector, are treated separately.

1.3.1 Step I : Photoemission

The photoemission process has been extensively treated in sect. 1.1. Now, let's call the initial core electron wave function with quantum numbers (n, l, m), $\psi_c(\mathbf{r})$, and the final photoelectron wave function with wave vector $\mathbf{k}$ and quantum numbers (l', m'), $\phi(\mathbf{r}, \mathbf{k})$, then eq. 1.29 becomes

$$\frac{d\sigma}{d\Omega} \propto | < \phi(\mathbf{r}, \mathbf{k}) | \varepsilon \cdot \mathbf{r} | \psi_c(\mathbf{r}) > |^2. \tag{1.85}$$

This is the dipole approximation that implies the well know selection rules of eq. 1.35. It is worth noting that the cross section depends on the angle θ_p between the polarization vector ε and the emission direction. In the particular case of photoemission from an s level ($l = 0$) for example, the final

state is a wave of p type ($l' = 1$) and the emitted intensity is proportional to $cos^2(\theta_p)$. This gives strong anisotropy of the emitted intensity which goes to zero for $\theta_p = 90°$.
In order to avoid such atomic effects on the photoemission intensity, the photoelectron diffraction technique, that is used to study solid state structural effects, is performed by keeping the photon incidence and electron analysis directions constant. Therefore, as already mentioned before, the photoelectron diffraction pattern is obtained by rotating the sample or changing the photon energy at constant θ_p. In this way the measured intensity is just due to the interference between direct and scattered waves. By using this data collection mode the so-called *Constant Initial State*, CIS spectra are obtained.

1.3.2 Step II : Scattering from atoms

Single scattering approach

After the photoemitted electron leaves the emitter, it undergoes scattering by the surrounding atoms. In the single scattering approximation [47] the final state wave function $\phi(\mathbf{r}, \mathbf{k})$ is a linear superposition of the direct wave $\phi_0(\mathbf{r}, \mathbf{k})$ with all the waves $\phi_j(\mathbf{r}, \mathbf{r}_j \rightarrow \mathbf{k})$ singly scattered at $\mathbf{r}_j$ and emerging in the direction $\mathbf{k}$

$$\phi(\mathbf{r}, \mathbf{k}) = \phi_0(\mathbf{r}, \mathbf{k}) + \sum_j \phi_j(\mathbf{r}, \mathbf{r}_j \rightarrow \mathbf{k}). \tag{1.86}$$

Since the electron detector is far away from the emitter, at infinity along $\mathbf{k}$, these waves can be considered of spherical form

$$\phi_0 \propto \frac{e^{ikr}}{r}, \tag{1.87}$$

$$\phi_j \propto \frac{e^{ik|\mathbf{r}-\mathbf{r}_j|}}{|\mathbf{r}-\mathbf{r}_j|} f_j(k, \theta_j) \tag{1.88}$$

with $\mathbf{r}$ and $\mathbf{k}$ the electron position and wave vector respectively, θ_j the angle between $\mathbf{r}_j$ and $\mathbf{k}$ and $f_j(k, \theta_j)$ the scattering factor of the atom at $\mathbf{r}_j$.
In order to calculate the electron-atom scattering, the wave ϕ_0 is further approximated by a plane wave, $\phi_0 \propto e^{ikr}$ and the complex scattering factor becomes

$$f_j(k, \theta_j) = |f_j(k, \theta_j)| e^{i\chi_j(\theta_j)} \tag{1.89}$$

with $\chi_j(\theta_j)$ representing the phase shift associated with the scattering. An example the amplitude of the plane wave scattering factor as a function of the scattering angle and kinetic energy is given in fig. 1.12.

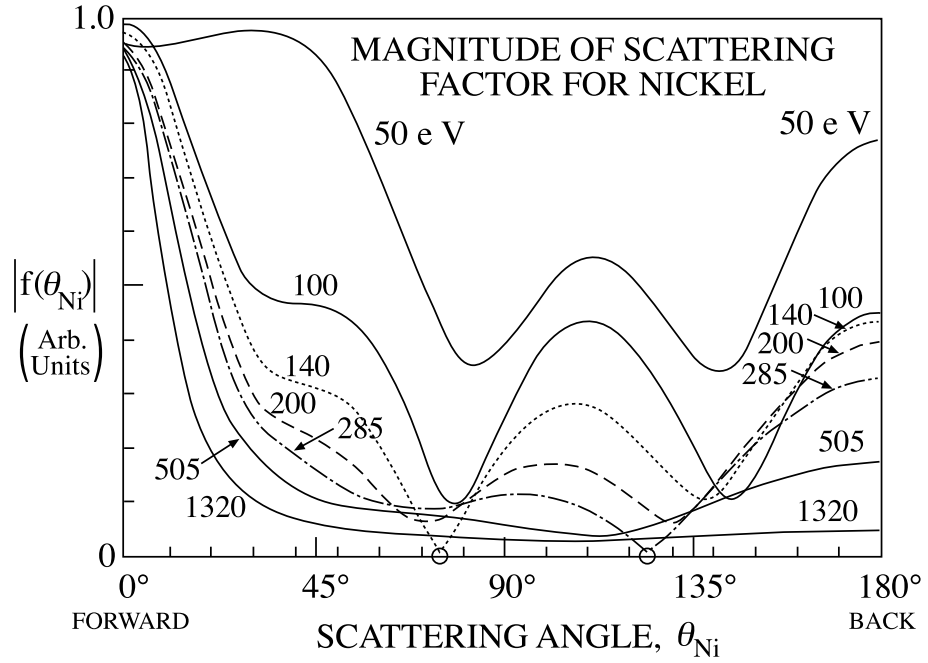

Figure 1.12: Amplitude of the plane wave scattering factor for Nickel [47].

By applying the partial wave method to a suitable spherically symmetric potential [7], the scattering factor $f(k,\theta)$ can be most accurately written as

$$f(k,\theta) = \frac{1}{k}\sum_{l=0}^{\infty}(2l+1)e^{i\delta_l}sin\delta_l P_l(cos\theta) \tag{1.90}$$

where P_l are Legendre polynomials and δ_l the partial-wave phase shifts.
The scattering potentials at each lattice site can be represented by charge spheres of finite radius r_{MT}, slightly lower than half the nearest neighbour distance, and by a constant potential in the interstitial region, the so called *muffin tin* potential.
Considering again eq. 1.89, the overall phase shift between the wave ϕ_0 and the scattered wave ϕ_j is given by

$$kr_j(1 - cos\theta_{j)} + \chi_j(\theta_j), \tag{1.91}$$

i.e. by the pathlength difference plus the scattering phase shift of the atom at r_j. This is sketched in fig. 1.13. Interference fringes will be observable when

$$kr_j(1 - cos\theta_{j)} + \chi_j(\theta_j) = 2\pi n. \tag{1.92}$$

The final intensity is the sum of the individual intensities of the emitters as given by eq. 1.85, i.e.

$$I(k,\theta,\varphi) \propto \sum_{emitt} | < \phi_0 + \sum_j \phi_j|\varepsilon \cdot \mathbf{r}|\psi_c > |^2. \tag{1.93}$$

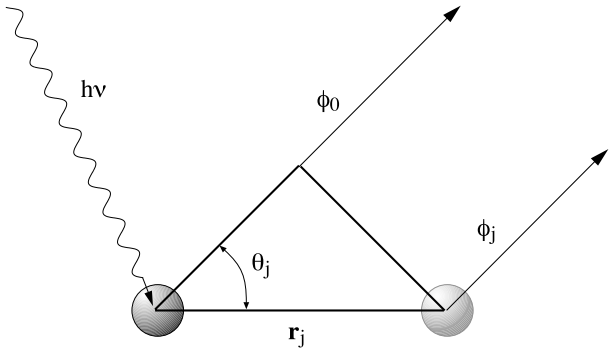

Figure 1.13: The primary wave ϕ_0 is scattered by the atom at a distance r_j from the emitter and generates the wave ϕ_j

Multiple scattering calculations

The emitted photoelectron usually does not only suffer one scattering event; therefore multiple scattering must be considered in order to perform a reliable photoelectron diffraction simulation.
A typical multiple scattering path is shown in fig. 1.14. Here the scatter-

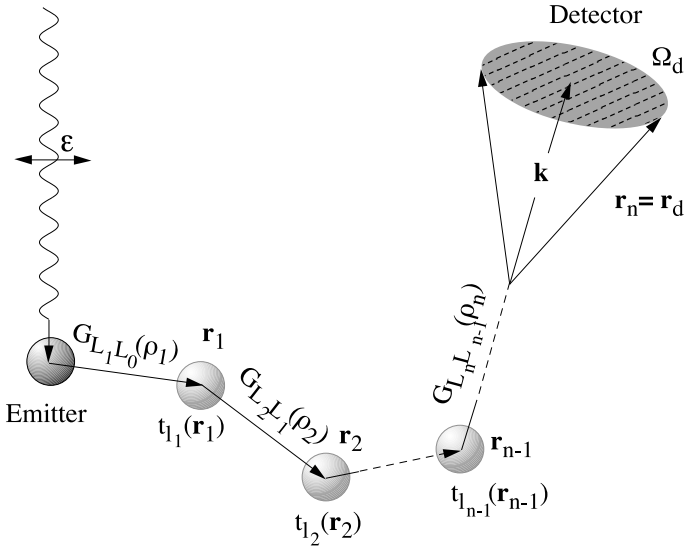

Figure 1.14: Multiple scattering path from the emitter to the detector placed at $\mathbf{r}_n$. The number of scattering events is n-1.

ing is formulated in terms of diagonal plane-wave scattering t matrices with elements $t_l = sin(\delta_l)e^{i\delta_l}$ and matrix elements of the free Green's function propagator $G_{L_{i+1},L_i}(k(\mathbf{r}_{i+1} - \mathbf{r}_i))$ $(L = (l, m))$ giving the strength of the component L_{i+1} of the spherical waves centered on $\mathbf{r}_{i+1}$ atomic sites [48].

The total intensity becomes [49]:

$$I_{nl}^{n_{sc}}(k,\theta,\varphi) = \sum_{emitt}\sum_{m}\left|\sum_{l'=l\pm1} m_{l',c}\cdot\Sigma_G\right|^2, \tag{1.94}$$

where n_{sc} is the scattering order (for single scattering $n_{sc}=2$), Σ_G is the sum of multiple scattering Green's functions for different scattering paths and

$$m_{l',c} = (-i)^{l'} e^{i\delta_{l'}} < \phi_{E_k,l'}|\varepsilon\cdot\mathbf{r}|\psi_c > \tag{1.95}$$

is the *radial matrix element*.

The strongest effect caused by multiple scattering is the defocusing of the intensity in a multiple forward scattering (i.e. at $\theta_j = 0$ in fig. 1.13) along a row of atoms. This is shown in fig. 1.15 for chains of 2, 3, 5 atoms of Cu with the emitter at their base [49].

Two important effects are missing in the calculations considered so far i.e. the inelastic scattering of the photoelectrons and the thermal vibrations.

The inelastic scattering attenuates the propagation of the electrons in the crystal. This is taken into account by introducing in the final formula a simple exponential damping of the elastic amplitude of each component ϕ_0 and ϕ_j with the distance L, $e^{-L/2\lambda}$, with λ the inelastic mean free path of the photoelectrons [50].

The thermal vibrations modulate the pathlength differences and this can be thought as the scattered waves lose some of their coherence thus reducing the intensity of the diffraction peaks. This effect is taken into account in the calculations via a Debye-Waller damping factor W [47].

In order to perform multiple scattering calculations several computational approaches have been developed. Usually the Green function of the total system is expanded into a series over all scattering pathways from the emitter to the detector but further approximations are needed in order to reduce the computational time. Two approximate schemes have been used to perform the photoelectron diffraction simulations of this thesis, namely those developed by Fritzsche [51] and by Rehr and Albers [52].

Computer programs based on the first scheme have been successfully applied to perform many surface structural determinations by Woodruff and Bradshaw's group [53, 54] while the second scheme has been adopted in one of the more recent multiple scattering codes called MSCD, developed by Y. Chen and M.A. Van Hove [48, 55].

For the calculation of the phase shifts, which are among the most important parameters for the description of the elastic scattering of the electrons, and which depend on the material and the electron kinetic energy, the Barbieri-Van Hove phase shift package was used [56]. The radial matrix element were computed with the PSRM utility program included in the MSCD package [55].

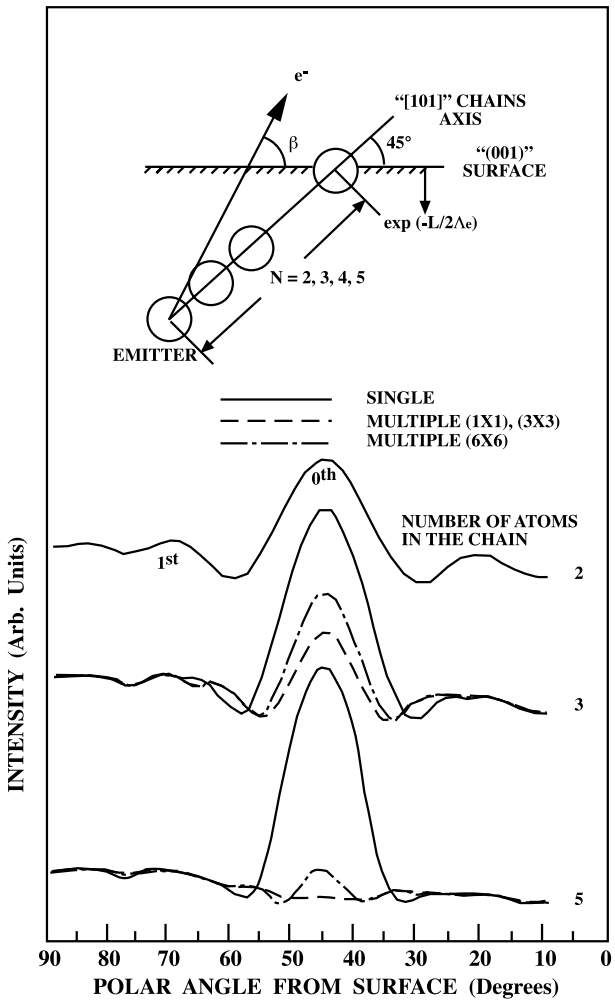

Figure 1.15: Calculated Auger electron diffraction patterns at 917 eV for linear chains of Cu atoms in single and multiple scattering. The geometry adopted in the calculation is shown at the top [49].

1.3.3 Step III: Surface refraction

The last step of the model considered is the transmission of the electron through the surface to reach the vacuum. This implies that the electron must overcome the potential barrier at the surface, that can be approximated to a sharp step whose height is the *inner potential* V_0. This lowers its kinetic energy in the vacuum by V_0. As a consequence refraction takes place at the surface barrier of the solid.
The momentum of the photoelectron parallel to the surface $\mathbf{k}_{\parallel}$ has to be conserved when the wave in the solid matches to the free electron wave in the vacuum. This defines the change in $k_{\perp}$ and therefore the change of the

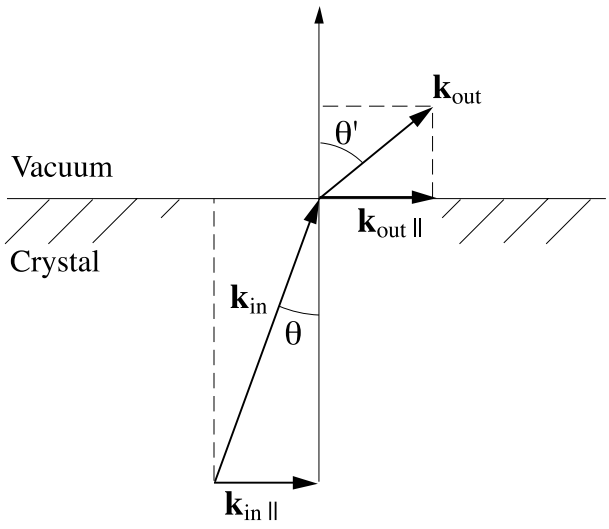

Figure 1.16: Electron refraction at the surface potential barrier.

angle with respect to the surface normal, between the electron trajectory in the solid and in vacuum. This is shown in fig. 1.16. The angle θ' is given by:

$$sin\theta' = sin\theta\sqrt{\frac{(E' + V_0)}{E'}}. \tag{1.96}$$

The value of the inner potential is given roughly by the sum of the work function and the valence band width. It can assume values from 5 to 20 eV. In a scattering simulation it is usually treated as adjastable parameter.

1.3.4 Forward scattering photoelectron diffraction

Let's consider the results of the calculation of the amplitude of the scattering factor shown in fig. 1.12. The most notable feature is the strong peak at 0° which dominates at all kinetic energies except 50 eV. Moreover, the higher is the kinetic energy the narrower this peak becomes. It is the so-called *forward scattering* peak. On the contrary, at the opposite angle, 180°, in the *back scattering* geometry, the intensity is very small at 500 eV and grows when the kinetic energy decreases.
A forward scattering geometry is found when an atom is sitting in line between the electron detector and the emitter [53]. In this particular direction, at sufficently high kinetic energy the photoemission intensity increases because of the forward scattering enhancement, also called *forward focusing*. This is due not only to the strong forward scattering but also to the small scattering phase shift at high kinetic energy, otherwise the interference could also be destructive. A sketch of this effect is shown in fig. 1.17.

Forward scattering photoelectron diffraction has been extensively used to

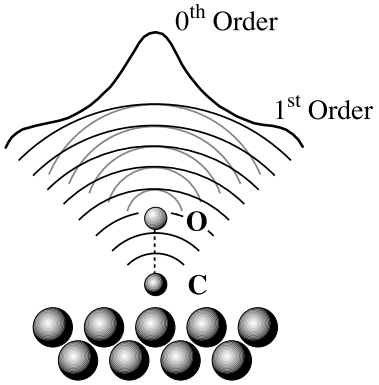

Figure 1.17: CO molecule adsorbed on a surface, in the on-top adsorption site. C is the emitter while O the scatterer [53].

determine the orientation of molecules adsorbed on surfaces by performing angular scans, either polar and azimuthal. Moreover, azimuthal scans at a grazing emission angle can give valuable informations on the symmetry of the adsorption site [53].
In the studies that are presented in this thesis, we used the photoelectron diffraction technique for a different purpose, i.e. not to make a structural characterization but to determine the *chemical identity* of the surface core level shifted components of different metals.

Chapter 2

Experiment

The key ingredient to perform surface science experiments is the ultra-high vacuum (UHV) for two reasons: first because of the need of keeping a surface clean long enough to be able to study it and, second, because the investigation techniques using electrons, like photoelectron spectroscopy, operate only if the mean free path of the electrons in the gas phase is long enough to allow them to reach the detector, i.e. in the metric range.
The contaminants on a surface can come from the ambient atmosphere, or from inpurities that diffuse from within the bulk to the surface. The effects of the former are proportional to the impact rate for a gas onto the surface

$$\frac{P}{\sqrt{(2\pi mkT)}},$$

where m is the mass of the molecules, P is the pressure and T the temperature [3]. With a sticking probability of 1 the surface would become completely covered in a few seconds at a pressure of 10^{-6} mbar thus preventing any kind of measurement to be performed. This is why pressures in the range of 10^{-10} mbar or below, are needed.
There are many ways to prepare a clean surface and this depends on which kind of sample is used. The materials considered in this thesis are Be, Rh and Ru single crystals. The procedure used to clean the surfaces of these metals are described in detail in the experimental sections of chapters 3, 4, 5. An *in situ* prepartion of these surfaces involves *sputtering* cycles, which means ion bombardment with Ar^+ or Ne^+ followed by annealing treatments, and heating to high temperatures in UHV to evaporate surface impurities. In the case of Rh and Ru the high temperature annealing is performed in oxygen atmosphere to remove the residual carbon from the sputtering.

2.1 UHV set-up

The experiments of this thesis were performed in the experimental chamber, shown in fig. 2.1, of the SuperESCA beamline (see sect. 2.3) [57].

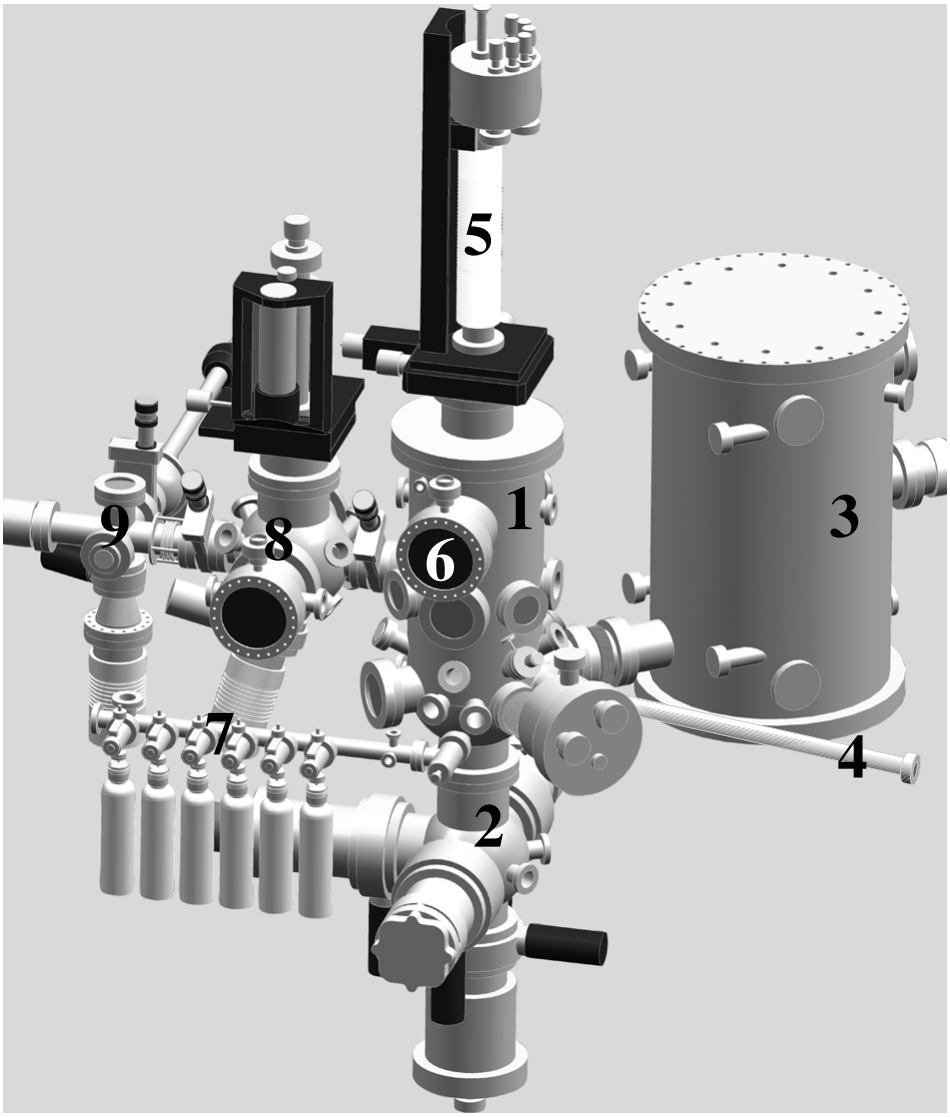

Figure 2.1: Drawing of the SuperESCA experimental chamber. (1) Vacuum chamber with two μ-metal shields inside. (2) Pumping system. (3) Electron energy analyser. (4) Beamline. (5) Sample manipulator. (6) Low Energy Electron Diffraction (LEED). (7) Gas inlet. (8) Preparation chamber. (9) Transfer system with fast entry lock.

The chamber (1) is made of stainless steel and is isolated from residual magnetic fields which would deflect the electron trajectories, by two internal μ-metal shields. It is pumped by a pumping system (2) which is composed of two magnetically suspended turbo pumps, a cryogenic pump, a Ti sublimation pump and an ion pump. The overall pumping speed is of the order

of 1500 l/s. The pumping system permits to maintain a stable base pressure in the chamber of 10^{-10} mbar.
The chamber is composed of three different levels. The double pass electron energy analyser (3) is mounted in the bottom level . In this level also the beamline (4) (see sect. 2.3) is connected. The angle between the beamline and the electron analyser is 40°. The intermediate level is for tranfering samples from the air to the vacuum using the transfer system and fast entry lock (9). In the top level the sample manipulator (5) is mounted together with the LEED instrument (6). A gas inlet system (7) with the possibility of using a channelplate doser, is also connected to the chamber. Finally, a preparation chamber (8) is available. The chamber is also equipped with a sputter gun, mass spectrometer, and various evaporators.

Two different manipulators are available, namely a 5 degrees of freedom (xyz θ, ϕ) fully computer-controlled sample manipulator and a manual, 4 degrees of freedom manipulator. The first one, shown in fig. 2.1, is a modified version of the CTPO from VG Instruments and the sample temperature range is 120-1500 K while the second one is an He cryostat with xyz translations and just 1 rotational axes θ but with sample temperature range of 20-1500 K. The transfer system is not usable with the low temperature manipulator. In all the experiments of this thesis we used the CTPO manipulator.

2.2 Electron energy analyser

The experimental station is equipped with a double pass electron energy analyser shown in fig. 2.2 [58]. It is composed by a lens system and two hemispheres of 150 mm mean radius R_0, each. This design allows performances comparable to a 300 mm electron energy analyser. It is operated at fixed *pass energy* E_0 (the energy at which electrons follow a circular trajectory inside the spheres) and the energy scans are performed by scanning the voltages of the electron lenses. The energy resolution depends on the pass energy, on the angle α which the electrons enter the slit placed at the end of the lenses and at the entrance of the first hemisphere, as well as on the dimension h of this entrance slit, through the relation

$$\Delta E = E_0\Big(\frac{h}{4R_0} + \frac{\alpha^2}{4} + \frac{\Phi^2}{8}\Big),$$

where Φ is a parameter that depends on the length and curvature of the entrance slit.

The analyser is equipped with a novel detector with 96 discrete parallel anodes, also shown in fig. 2.2 [59]. Since the energy dispersion of the electrons is almost linear with the position on the detector, it allows to measure a spectrum with 96 points in one shot, so-called *snap shot mode*. However,

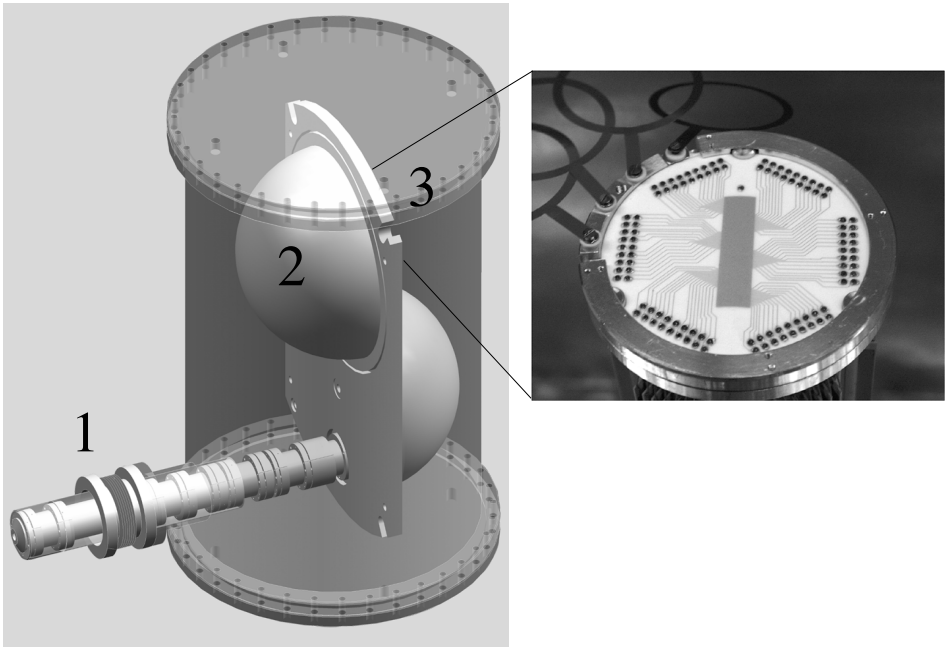

Figure 2.2: left: drawing of the double pass electron energy analyser composed by a lens system (1) and two hemispheres 150 mm each (2). right: 96 multichannel parallel detection system (3).

this acquisition mode, while allowing to achieve very high acquisition rates since the voltages of the lenses do not need to be scanned, does not provide very high energy resolution. Since the latter is a fundamental requirement to be fulfilled in our SCLS measurements, we always used the analyser in the *scanning* mode.

2.3 SuperESCA beamline

The light sources used in photoelectron spectroscopy are of several different kinds. In core level photoemission, the X-rays are usually produced by conventional sources which are based on the Mg or Al K_α emission. These sources provide photons at fixed energy of ≈1256 and ≈1486 eV (the energy difference between the $1s$ and $2p$ levels of the two materials), with an energy spread of the order of 0.6 eV and 1 eV for Mg and Al respectively.

Other X-ray sources are now widely used, i.e. electron-storage rings that produce synchrotron radiation. There are many advantages of using synchrotron radiation, the most important ones being its energy tunability and high photon flux.
Synchrotron radiation is produced by the electrons that orbit in a large storage ring with a velocity close to the speed of light (see fig. 2.3). In this

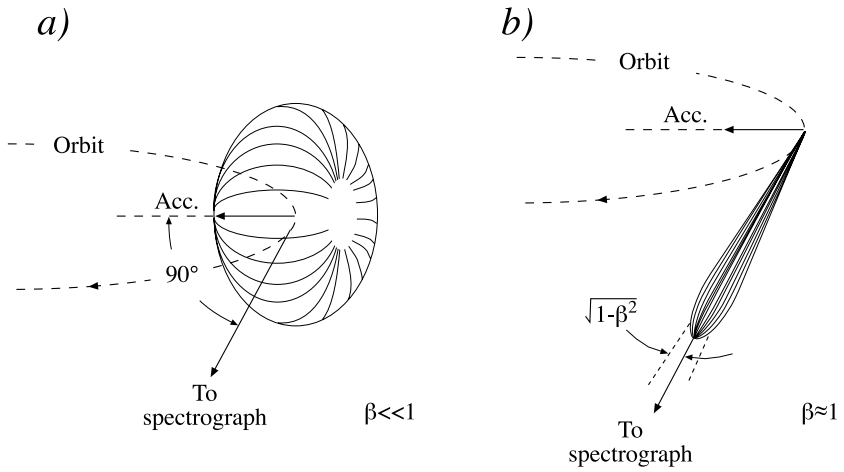

Figure 2.3: Radiation pattern for *a*) a slow electron and *b*) a relativistic electron moving in a circular path [60].

case the radiation is sharply peaked in the forward direction when observed from the laboratory frame and has a broad, continuum range of photon energies, high brilliance and high photon flux. Moreover, in the orbit plane the synchrotron radiation is plane polarized while it is elliptically polarized slightly out of this plane.

We performed all the studies of this thesis on the SuperESCA beamline of the ELETTRA storage ring, placed in Trieste, Italy [61]. This is a third generation synchrotron facility, where the light not only is produced by the bending magnets but also by insertion devices, which are placed in the straight sections of the storage ring. These are periodic magnetic arrays which give radiation in a narrower energy range and with higher intensity than the bending magnets.

The insertion device of the SuperESCA beamline is a 56 mm period undulator (minimum gap 19 mm), composed of three sections with 81 periods, which covers a photon energy range of 85 to 1500 eV at a ring energy of 2 GeV. When the ring is operated at 2.4 GeV the photon energy range is 120 to 2100 eV.

The beamline is sketched in fig. 2.4. The monochromator is a stigmatic SX700 with a horizontally pre-focusing mirror (cylindrical mirror, magnification 8:1) and an entrance slit, and covers the photon energy range from 85 to ≈1000 eV with a single plane grating. The resolving power of the monochromator, (E/ΔE) is of the order of 10^4 at 400 eV, while it decreases to $\approx 5 \times 10^3$ at 900 eV. An ellipsoidal re-focusing mirror (magnification 2:1) focusses the monochromatized radiation in the center of the experimental

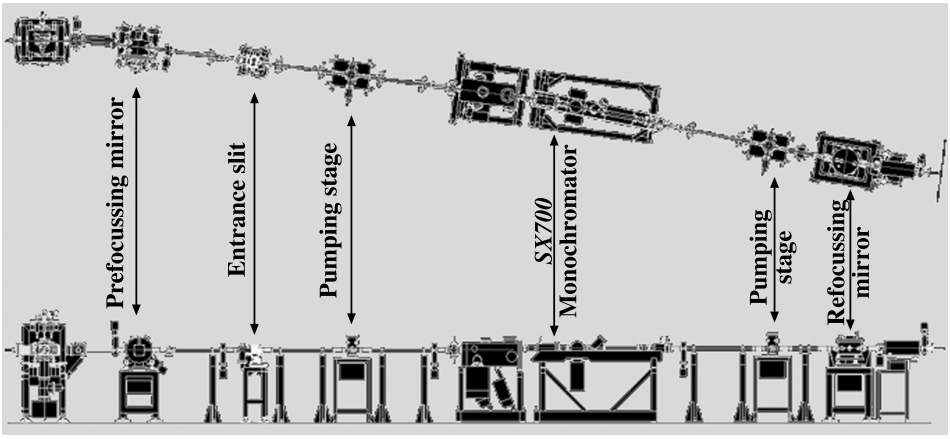

Figure 2.4: Sketch of the SuperESCA beamline. The optical elements are: cylindrical pre-focusing mirror, fix focus PGM (SX700) with plane mirror, plane grating and focusing ellipsoidal mirror, ellipsoidal re-focusing mirror. Fixed entrance and exit slits are also present. The exit slit is at the end of the monochromator.

chamber. The size of the spot on the sample is 100×(exit slit dimension) μm^2. The photon flux at 400 eV and resolving power 10^4, is of the order of 10^{11} photons/s.

Chapter 3

SCLS assignment using photoelectron diffraction

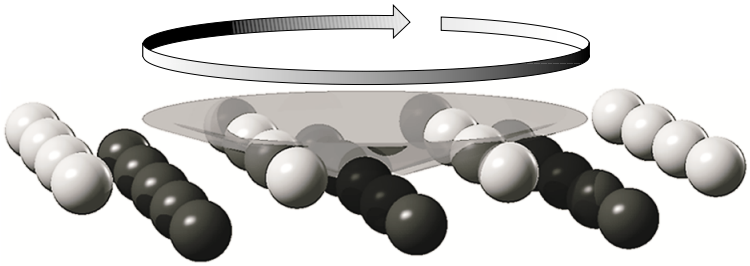

Figure 3.1: Azimuthal angle scan photoelectron diffraction for SCLS assignment. The gray atoms are from the top layer while the black ones belong to the second layer.

The different environment between the surface atoms and those in the bulk of a solid gives rise to the SCLS's, as explained in sect. 1.2. These shifts are usually quite small and can be resolved in a core level photoemission spectrum only thanks to the high energy resolution available today.
Most clean metal surfaces display, at least apparently, just one single core level shifted component related to the top layer atoms while the SCLS's for the deeper layers are unmeasurably small because these atoms have a chemical environment quite similar to that in the bulk. However, some metals exist which clearly display more than one shifted component. In this case it is crucial to find the right assignment between core level shift and chemical environment.
In this chapter we show how we achieved this in a straight-forward way, using high-resolution angle scan photoelectron diffraction at high energies. Azimuthal scans are preferred to polar scans because in the first case the symmetry of the system is reflected in the angular modulation of the pho-

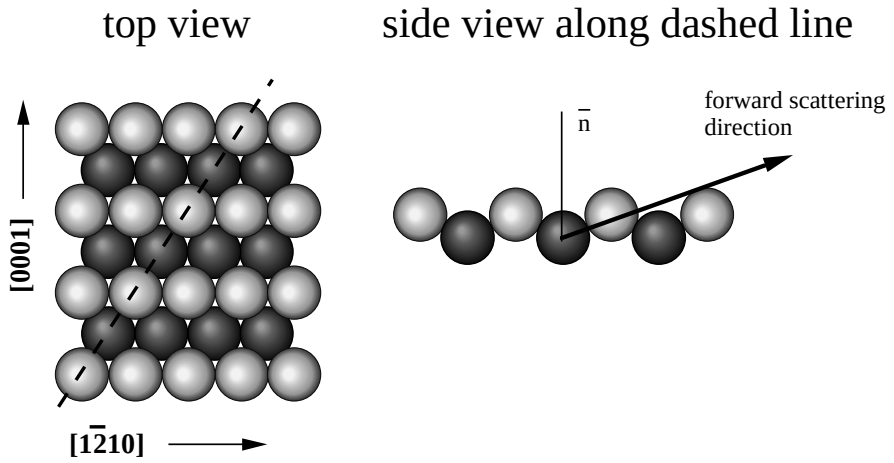

Figure 3.2: Sketch of the forward scattering geometry for the Be(10$\bar{1}$0) surface. A first layer atom has to lie on a straight line between a second layer atom and the electron detector.

toemission intensity and this provides an easy check for the quality of the diffraction data. Moreover, the path travelled by the electrons in the solid is always constant for azimuthal scans while it changes quite strongly in the case of polar scans, rendering the calculations of the diffraction pattern more complicated.
The basic idea of the experiment is to use the high atomic forward scattering factor and small scattering phase shift of the ion cores for electrons with kinetic energies more than about 400 eV [53] (see sect. 1.3.4). In the so-called forward scattering geometry where an atom of the first layer lies on a straight line between a second layer atom and the detector (see fig. 3.2), this strong forward scattering ensures an enhancement of the core level component from the second layer. An inspection of the spectra taken in an angular scan around this forward scattering geometry then reveals the identity of the second layer peak which shows the pronounced forward-scattering enhancement while the intensity from the first layer stays more or less constant.

3.1 Be(10$\bar{1}$0)

The surfaces of beryllium provide an excellent test case for the quantitative understanding of SCLS for two reasons: the first one is that both the (0001) and the (10$\bar{1}$0) surface show three unusually large surface related 1*s* core level shifts [62, 63] and, the second is that their geometric structure is already known (see fig. 3.3 for the Be(10$\bar{1}$0) surface).

The number of shifted components and the size of the shifts are caused

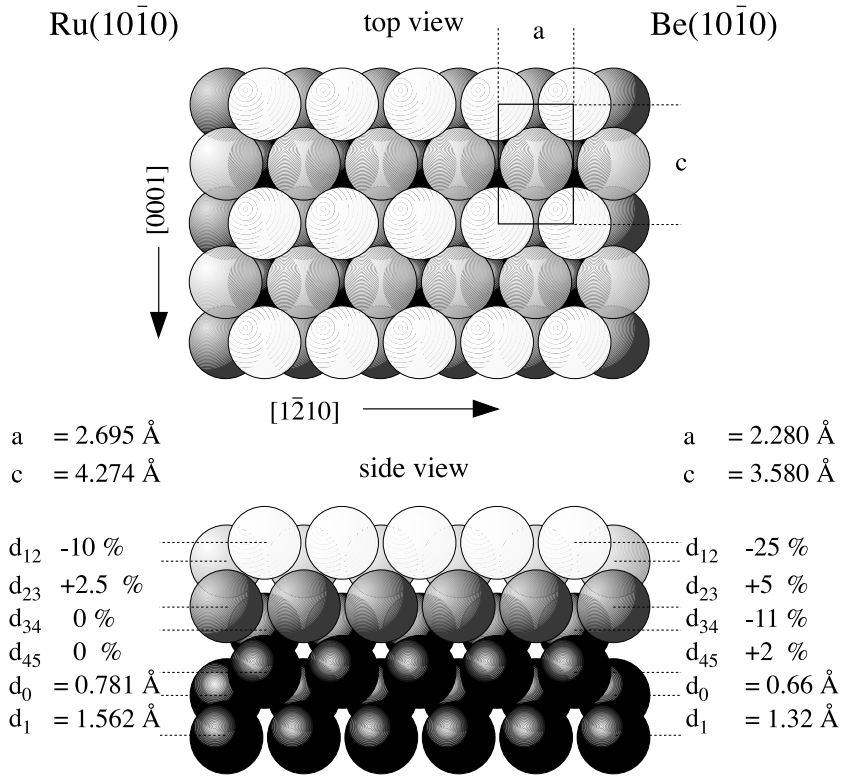

Figure 3.3: Surface structure of Be(10$\bar{1}$0) and Ru(10$\bar{1}$0) [64, 65].

by the unusual electronic structure of Be. While the bulk has a low density of states at the Fermi-level the surface electronic structure is dominated by the presence of metallic surface states, as shown in fig. 3.4 [66, 67, 68]. In this sense Be is closer to a semiconductor than to a simple metal.
Johansson and co-workers have assigned the SCLS such that the component with the largest shift originates in the first layer, the component with the second largest shift in the second layer and the component with the smallest shift in the third and third plus fourth layer for Be(0001) and Be(10$\bar{1}$0), respectively. This assignment was not only based on intuition but also supported by the relative intensity of the lines: the SCLS lines from the deeper layers were lower in intensity, consistent with the expectation that the electrons from these layers are more likely to suffer inelastic scattering processes. For Be(0001) four different calculations gave more or less satisfactory agreement with the measured shifts [66, 69, 70, 71]. All calculations confirmed the basic assignment of the experimental data.
On the (10$\bar{1}$0) surface doubt over the initial assignment of the shifted components in the core level spectrum was created by a calculation which predicted the second layer to have a larger shift than the first layer [72]. We have therefore investigated this issue by high energy-resolution angle-scan

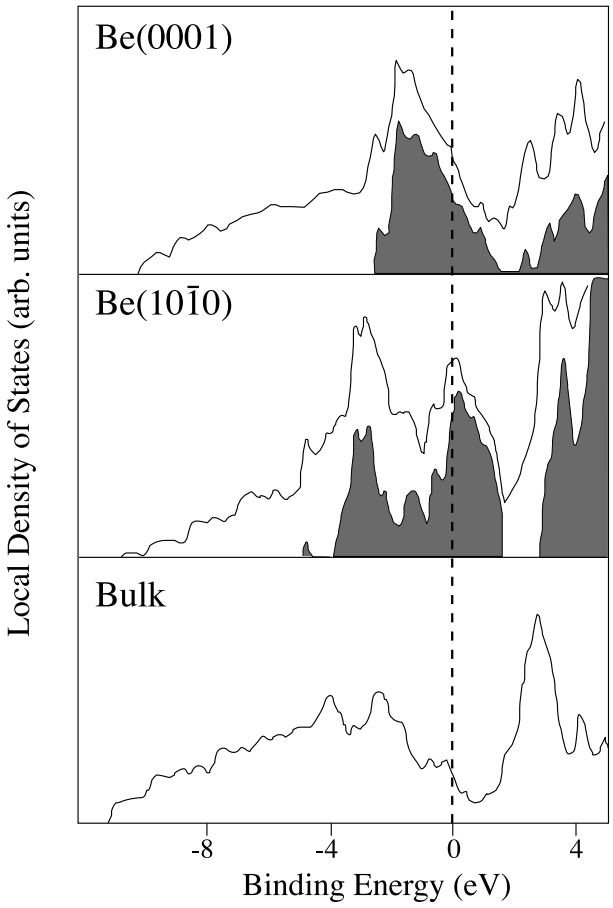

Figure 3.4: Electronic density of states for the Be(0001) and Be(10$\bar{1}$0) top layer atoms and for the bulk. The gray area represents the positive difference between the DOS of the top layer atoms and that of the bulk [67, 68].

photoelectron diffraction. In the following we will describe the results which, indeed, confirm the unusual assignment predicted by the latest theory. Then we will use the results of first-principles calculations to discuss the physics of the Be(10$\bar{1}$0) core level spectrum.

3.1.1 Experimental

The clean Be(10$\bar{1}$0) sample was prepared by repeated cycles of Ne^+ sputtering at 670 K and annealing to 720 K [73]. Surface order and cleanliness were checked by LEED and core level photoemission which did not show any presence of oxygen or other contaminants below the detection limit of 0.005 ML.
Be 1s core-level spectra were taken for two photon energies: $h\nu$=180 eV for the high resolution XPS, and $h\nu$=500 eV for the photoelectron diffraction

measurements. The combined resolution of the beamline and the electron energy analyzer was 70 meV and 250 meV, respectively. The lower energy resolution of the photoelectron diffraction experiment is due to the need for a higher photon flux because of the small cross section for the Be 1s excitation at higher energies. All the measurements were performed at a sample temperature of 120 K with a base pressure in the chamber lower than 2×10^{-10} mbar. The photoelectron diffraction experiment consisted of an azimuthal scan at a polar emission angle of 75° off the surface normal, selected for maximum forward scattering.

3.1.2 Results

Fig. 3.5 shows a spectrum taken at $h\nu$=180 eV. We have fitted these data to four Doniach-Sunjic lines convoluted with Gaussians and a linear background. This resulted in shifts and line shape parameters very similar to those found by Johansson et al. [63] except for higher asymmetries of 0.09 and 0.14 for the bulk and surface components, respectively. Our SCLS are –0.71 eV, –0.50 eV and –0.24 eV for S1, S2 and S3, respectively. Note that we use the same nomenclature as Johansson et al., i.e. S1 is the component with the largest shift.

Fig. 3.6 shows three spectra taken at azimuthal emission directions [1$\bar{2}$10], [0001] and in the forward scattering direction. In the latter spectrum a very clear increase in the intensity on the low binding energy side is observed. From an inspection of the raw data, however, it is not possible to judge if this increase is due to the S1 or S2 component. We have fitted all the data taken at $h\nu$=500 eV using the fit parameters obtained at $h\nu$=180 eV only allowing for a different Gaussian width in order to account for the poorer resolution.

Fig. 3.7 shows the intensities of the S1 and S2 components as a function of azimuthal emission angle ϕ, normalized to the maximum intensity of the S1 component. It can be clearly seen that S1, i.e. the peak with the largest shift, shows the forward scattering enhancement at the expected angle ($\phi = 57.5°$) whereas S2 does not change very much as a function of ϕ. Furthermore the solid line in fig. 3.7 represents the result of a multiple-scattering calculation of the diffracted intensity, performed by V. Fritzsche in the Fritz-Haber-Institut, Berlin, Germany [74], of the photoelectrons emitted in the second layer which agrees remarkably well with the observed modulations of the S1 component. As input for the calculations the structural parameters of fig. 3.3 were used.

3.1.3 Discussion

While experiment and theory clearly show that the second layer gives a larger shift than the first layer, this result needs to be explained. First-principles

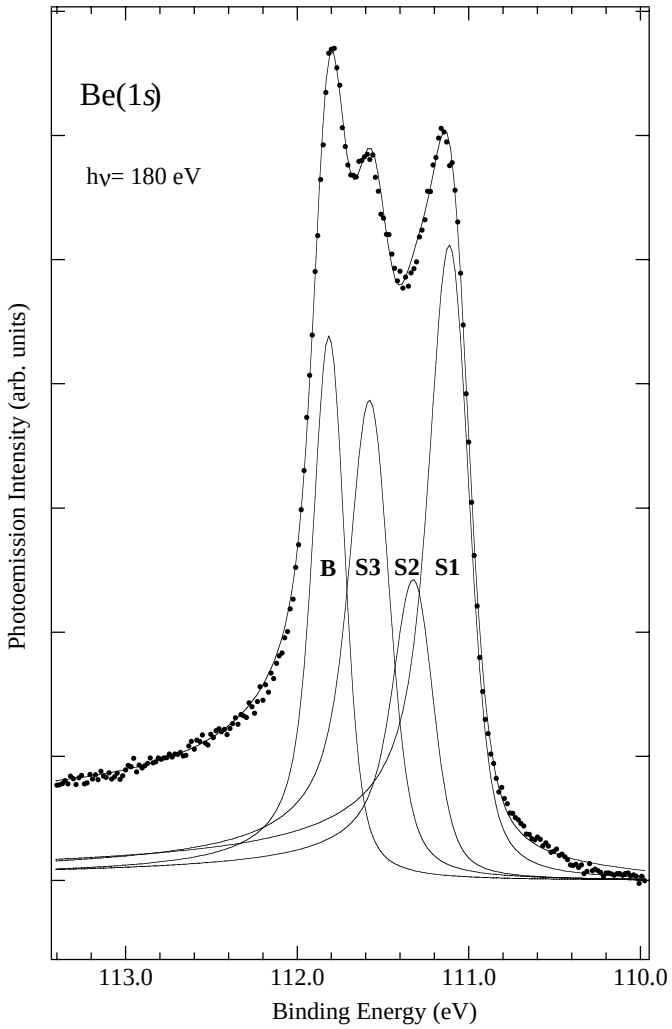

Figure 3.5: Be 1s core level spectrum taken at T = 120 K and $h\nu = 180$ eV in normal emission. An inspection of the raw data reveals that four lines are necessary to obtain a satisfactory fit. The solid lines represent the fitted components for the bulk (B) and the surface layers (S1,S2,S3). Note that we use the nomenclature of Johansson et al. (Ref. [63]) where S1 is the component with the largest shift.

calculations have been performed by R. Stumpf from Sandia National Laboratories, Albuquerque, New Mexico, USA, in which the total core level shifts for each layer are broken down into two initial state contributions (electrostatic and exchange/correlation) and the final state contribution (screening). The calculations [66] rely on density functional theory within the local density approximation (LDA) for exchange and correlation (XC) [75]. To calculate SCLS the total energy of a Be atom with a 1s core hole in the bulk

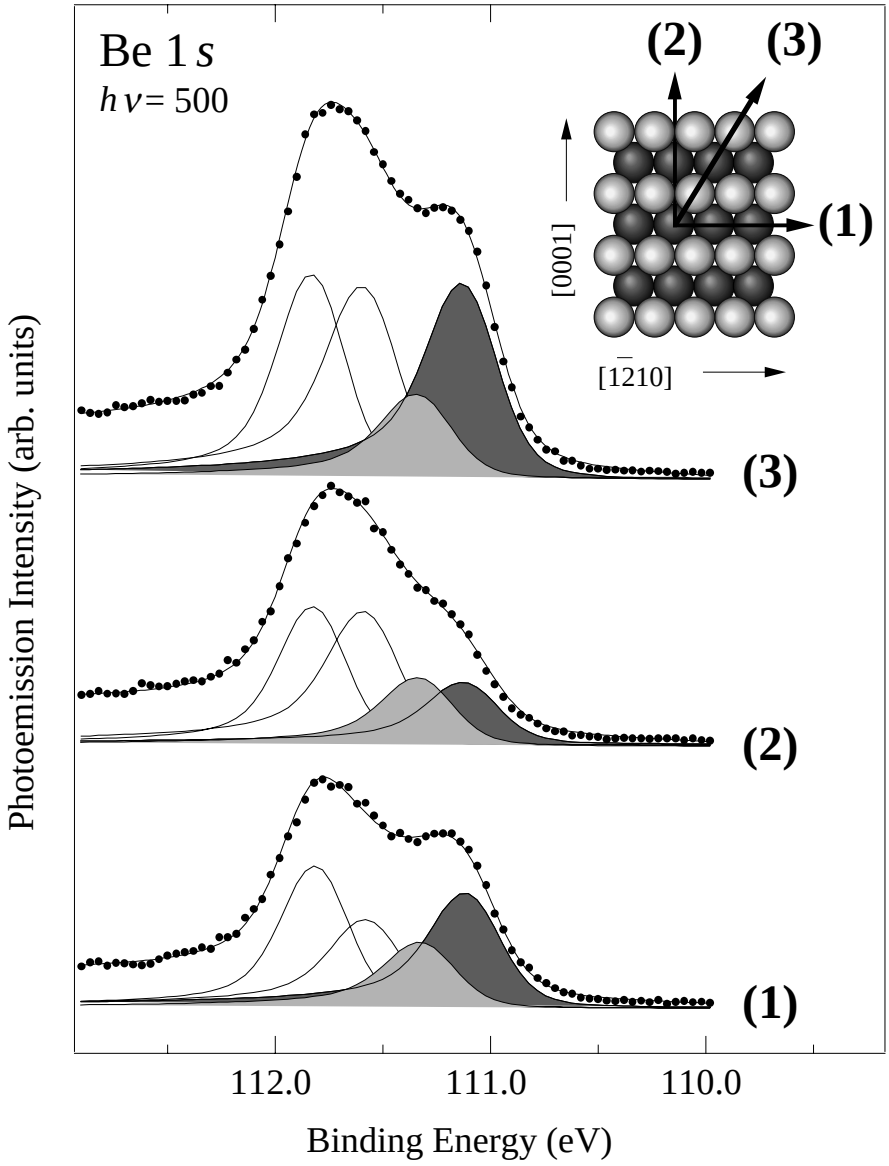

Figure 3.6: Three Be 1s core level spectra taken at T = 120 K and $h\nu$ = 500 eV taken at a polar emission angle of 75° off normal and an azimuthal emission direction of (1) [1$\bar{2}$10], (2) [0001], and (3) 57.5 deg off [1$\bar{2}$10], i.e. in the forward scattering geometry. The latter spectrum shows a clear enhancement of the intensity on the low binding energy side. A fit shows that this is due to the intensity increase of S1. The inset shows a sketch of the measurement geometry.

and in different surface layers was compared, without allowing structural relaxation in response to the core hole. For this purpose a Be pseudopotential

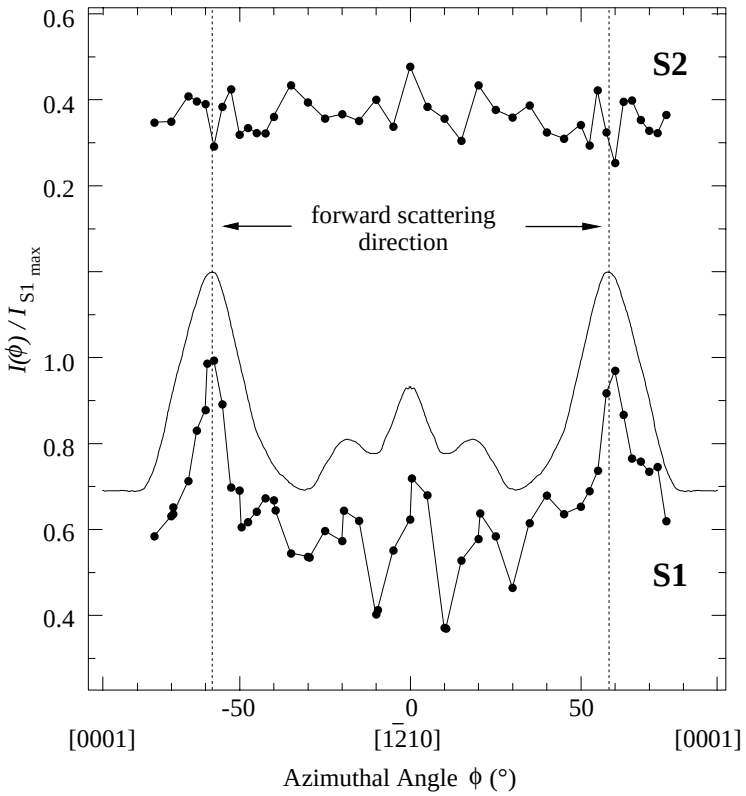

Figure 3.7: Angular dependence of S1 and S2, i.e. for the core level component with the largest and second largest shift. The S1 signal shows a clear peak in the forward scattering direction, indicating that S1 is due to emission from the second layer. The solid lines represent the result of a multiple scattering cluster calculation for the diffracted intensities.

with a core hole was constructed. To analyze the origin of the SCLS, the initial state contribution, which is the difference of bulk and surface electrostatic and XC potentials at the atomic cores of relaxed Be($10\bar{1}0$), must be considered. The final state or screening contribution is the difference between initial state and full SCLS.

The Be($10\bar{1}0$) surface is represented by fully relaxed 18 layer slabs. Ideally a single core hole should be used to calculate the SCLS. However, using a core hole concentration of 1/4 ML gives SCLS to better than 0.05 eV accuracy. Tests performed for **k**-sampling, slab thickness, impurity concentration and plane wave cutoff indicate that the calculated SCLS are converged to better than 0.1 eV within LDA.

Table 3.1 gives the resulting SCLS which agree qualitatively with the experiment. The unusual ordering of the SCLS is mainly caused by the anomalous electrostatic initial state shift for the first and second layers. The initial state

Table 3.1: Calculated and measured SCLS of Be(10$\bar{1}$0) in eV. Negative SCLS indicate a lower binding energy of the core electron as compared to the bulk. The initial state contribution is composed of a shift of the electrostatic and the exchange-correlation (XC) potential. The final state or screening contribution is the difference between the full and the initial state SCLS.

		1.lay	2.lay	3.lay	4.lay	5.lay
full SCLS	calculation	–0.57	–0.80	–0.39	–0.19	–0.18
	experiment	–0.50	–0.71	–0.24		
initial state		–.10	–0.62	–0.11	–0.11	0.01
	electrostatic	0.0	–0.59	–0.11	–0.11	0.01
	XC	–0.10	–0.03	0	0	0
final state		–0.47	–0.18	–0.28	–0.08	–0.19

shift for the first layer is very small. This is surprising keeping in mind the high contribution of surface states to the density of states in this layer [73]. It should create an electrostatic potential to keep the surface layer charge neutral causing an electrostatic shift of the core level towards lower binding energy, as sketched in fig. 3.8 [70, 71]. In this case, however, the calculation of the density of states projected on the top layer atoms (PDOS) shows a significant band narrowing due to the reduced coordination of the atoms. This reduction of the occupied PDOS almost compensates the surface state without a shift in the electrostatic potential of the first layer. The second layer atoms, on the other hand, are almost fully coordinated, which reduces the band narrowing. Furthermore, as shown in fig. 3.9, a p_z like peak is present in the PDOS which is cut by E_F; it is mostly empty in the first layer and moved below E_F in the second layer. The first-to-second layer bonds, which are partially formed by the second layer p_z orbitals, are especially strong which is reflected in the 25 % first layer contraction, as shown in fig. 3.3. This increases the surface state contribution in the second layer. Thus, the surface state is not compensated in the second layer and this leads to the large initial state shift.

The final state contribution reflects the ability of the electrons to screen the core hole. A good measure for this ability is the PDOS at the E_F. In the first layer this PDOS is very high due to the p_z like PDOS peak which is cut by E_F. In the second layer the p_z peak in the PDOS shifts below the Fermi energy and thus contributes little to the screening.

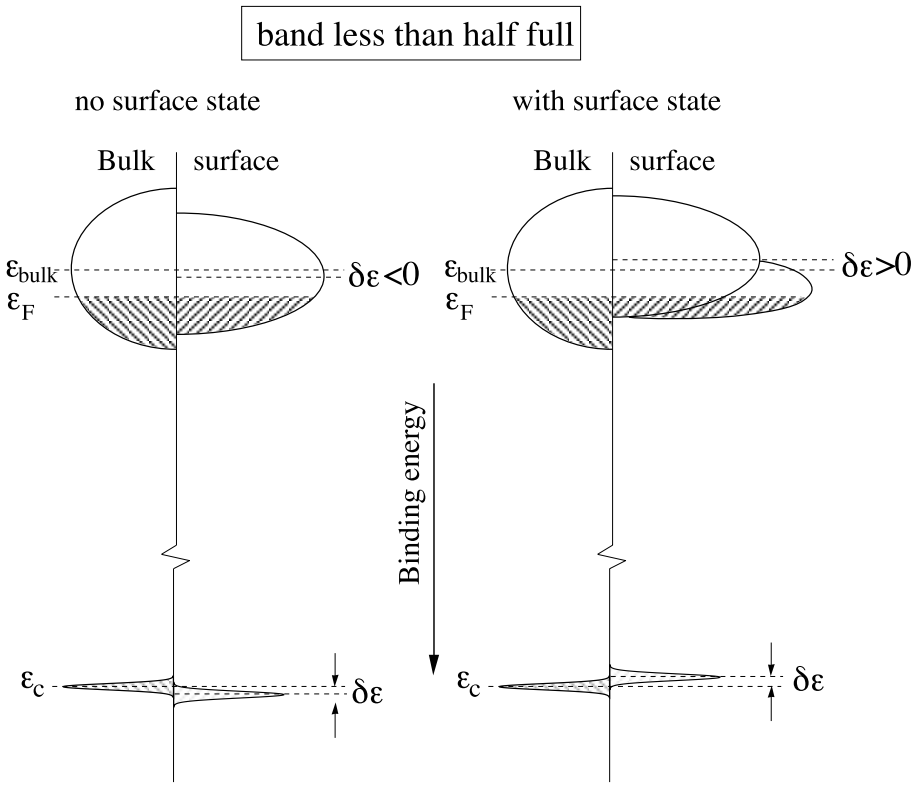

Figure 3.8: Schematic representation of the SCLS caused by the narrowing of the band (left) and, the same but in presence of a surface state (right). The band is less than half full; therefore the lower coordination gives a positive SCLS while the surface state creates an electrostatic potential to keep the surface layer charge neutral causing an electrostatic shift of the core level towards lower binding energy. Note that the effect of the surface state is the same also for a band more than half full.

3.2 Ru(10$\bar{1}$0)

As pointed out in the previous section, on most metals only the first layer of atoms gives rise to an observable surface core level shift. This is due to the nature of the metallic bonding: in the second layer the atoms are highly coordinated and embedded in a charge density very similar to the bulk. There are, however, exceptions to this general trend, as witnessed by the Be(0001) and Be(10$\bar{1}$0) surfaces as well as by the 5d transition metals where second layer shifts have been found in the very narrow 4f core lines [24, 76, 77].
In this section we report on the finding of three peaks also in the $3d_{5/2}$ core level spectra taken from Ru(10$\bar{1}$0). They can be assigned to emission from the bulk and the first two layers. This finding is rather unexpected since

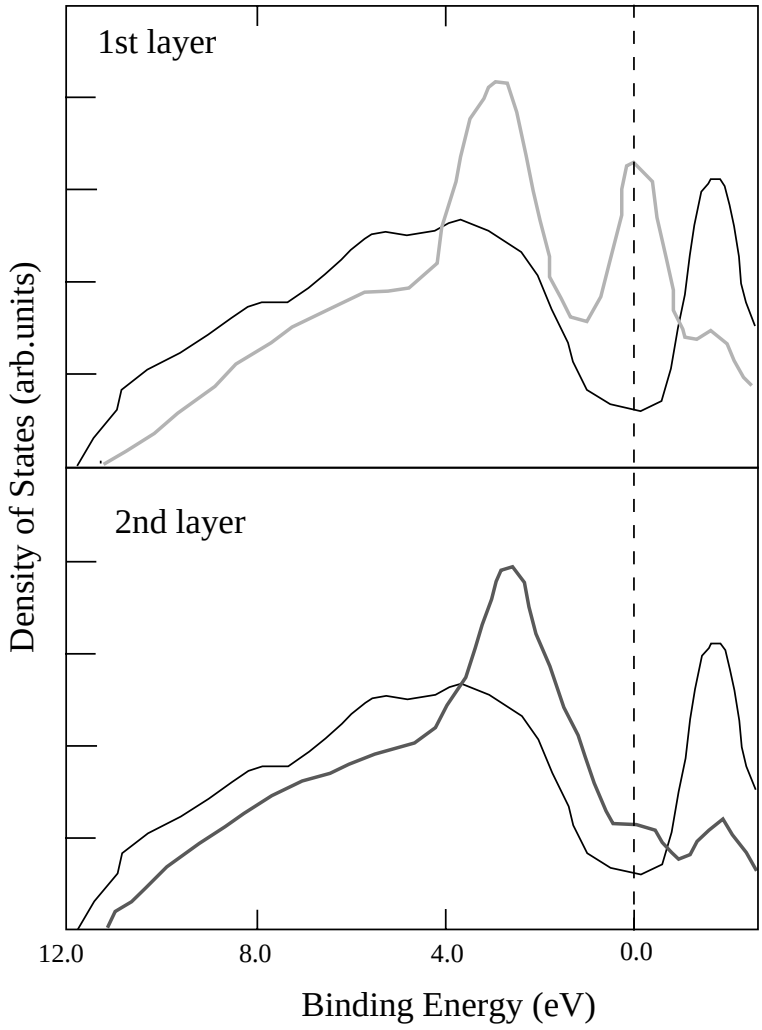

Figure 3.9: Calculation of the density of states (DOS) projected on the top (light grey) and second (dark grey) layer atoms, for Be(10$\bar{1}$0). The thin, black line represents the DOS of the bulk atoms.

no clearly observable second layer core level shifts have been reported for the other 4*d* transition metal surfaces. It is also of potential importance for further research on the catalytic properties of 4*d* transition metals: the second layer core level shift permits a detailed XPS investigation of the role the sub-surface atoms play in gas-surface interactions and Ru(10$\bar{1}$0) could be used as a model system. However, due to the findings on the SCLS of Be(10$\bar{1}$0) also in this case an independent confirmation of the right assignment of the different components is mandatory. In order to do this, we used the same experimental approach as on Be(10$\bar{1}$0), i.e. photoelectron diffraction at high energy.

3.2.1 Experimental

The Ru($10\bar{1}0$) sample was cleaned by repeated cycles of Ar^+ sputtering, annealing to 1500 K, oxygen treatment at 900-1100 K and oxygen reduction in hydrogen (p=1x10^{-6} mbar, T=800 K). This procedure resulted in a sharp (1x1) LEED pattern and in C, O and S 1s XPS intensities below our detection limit of 0.005 ML. All the experiments were performed at a temperature of 120 K. The high resolution data were acquired at several photon energies with an overall energy resolution of 65 meV. The emission direction was 40° off the surface-normal, the photons were coming in at 80° off-normal. The photoelectron diffraction experiment, an azimuthal scan at a fix polar emission angle of 75°, was performed at a photon energy of 500 eV and energy resolution of 200 meV.

3.2.2 Results

The upper part of fig. 3.10 shows the Ru $3d_{5/2}$ spectra measured at three photon energies. Three distinct structures, named S_b, S_1 and S_2, are clearly resolved in the spectra, with relative intensities strongly dependent on photoelectron kinetic energy. Saturating the surface with oxygen or carbon monoxide left only the position of the S_b peak unchanged, and the latter was therefore assigned to emission from the bulk. The data were analyzed quantitatively by a least-squares fit, where the line shape of each peak was described by a convolution of a Doniach-Sunjic function (Lorentzian width Γ, asymmetry α) and a Gaussian. Interestingly, very good fits, as judged by structureless residuals, could be obtained using the same set of line-shape parameters for all three peaks. As an example, the 365 eV photon energy spectrum is shown together with the fit in the lower part of fig. 3.10. The best fits parameter values are 0.28±0.01 eV, 0.085±0.010 and 75±10 meV for Γ, α and the Gaussian width, respectively. The obtained shifts of S_1 and S_2 relative to the bulk component are -480±10 meV and -240±10 meV, respectively.
In the simple qualitative picture of the SCLS, one would assign the component S_1 to emission from the first layer and the component S_2 to emission from the second layer. However, in order to obtain a reliable assignment, we have performed a Photoelectron Diffraction (PED) experiment. The procedure is the same as the one previously adopted for the Be($10\bar{1}0$) surface.
In order to find the best conditions to perform this experiment we made preliminary multiple scattering simulations of the photoemission intensity as a function of the azimuthal angle and at a fixed polar angle of 75°. We used the MSCD Package Program [55] which calculate the elemental and state-specific core-level photoelectron diffraction pattern from a surface, using multiple scattering theory and the Rehr-Albers separable representation of spherical-waves propagators. The structural parameters used in the sim-

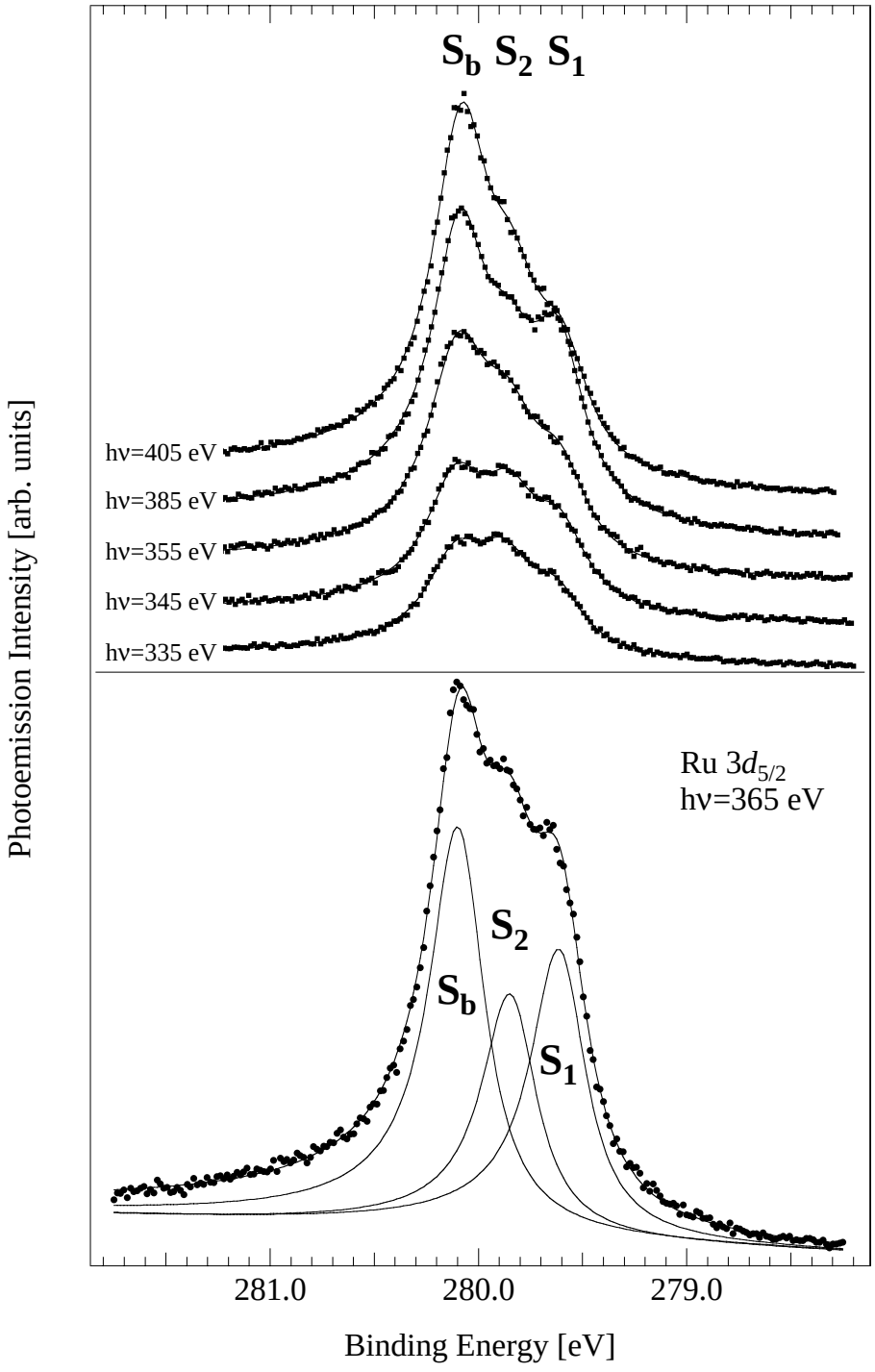

Figure 3.10: upper part: Ru $3d_{5/2}$ core levels spectra from Ru(10$\bar{1}$0) recorded at 120 K using photon energies ranging from 335 eV to 405 eV, and respective fits. lower part: the spectrum taken at 365 eV together with a fit using three components. The parameters are given in the text.

ulation have been taken from the LEED I/V work of Döll *et al.* [65] (see fig. 3.3).
We plot the modulation function for the S_1 and S_2 components. This function is defined as $(I(\phi) - I_0)/I_0$ where $I(\phi)$ is the intensity as a function of azimuthal emission angle and I_0 is the average intensity. $\phi = 0°$ corresponds to the direction of the close-packed atom rows on this surface and $\phi = 57.5°$ to the forward scattering direction. The results of the simulations at three different energies are shown in fig. 3.11. It can be clearly seen that

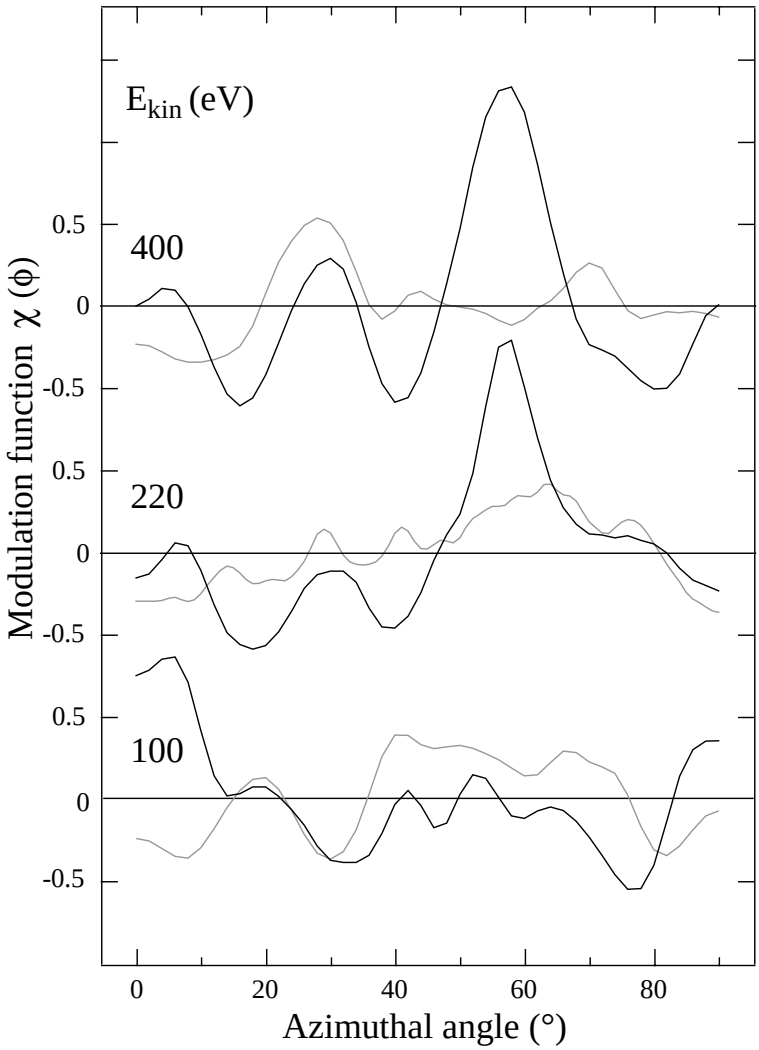

Figure 3.11: Simulations of the modulation function of the Ru $3d_{5/2}$ photoemission signal from the first (grey line) and the second (black line) layer atoms, at three different kinetic energies.

at a kinetic energy of 220 eV the forward scattering is quite strong, showing

the pronounced peak in the forward scattering direction. Moreover, it is also clear that a kinetic energy of 100 eV is not sufficient to have different modulation functions from the first and the second layer. The best kinetic energy, where the photoelectrons emitted from the second layer atoms show strong modulations, would be of 400 eV but, at such a high energy the photoemission cross section and the surface sensitivity would decrease quite drastically, resulting in a low intensity from the first atomic layers. Therefore we chose the kinetic energy of the Ru $3d_{5/2}$ core level peak to be 220 eV, corresponding to a photon energy of 500 eV.
Fig. 3.12 shows the result of the azimuthal scan recorded at 500 eV photon energy and at a polar emission angle of 75° off the surface normal. It is

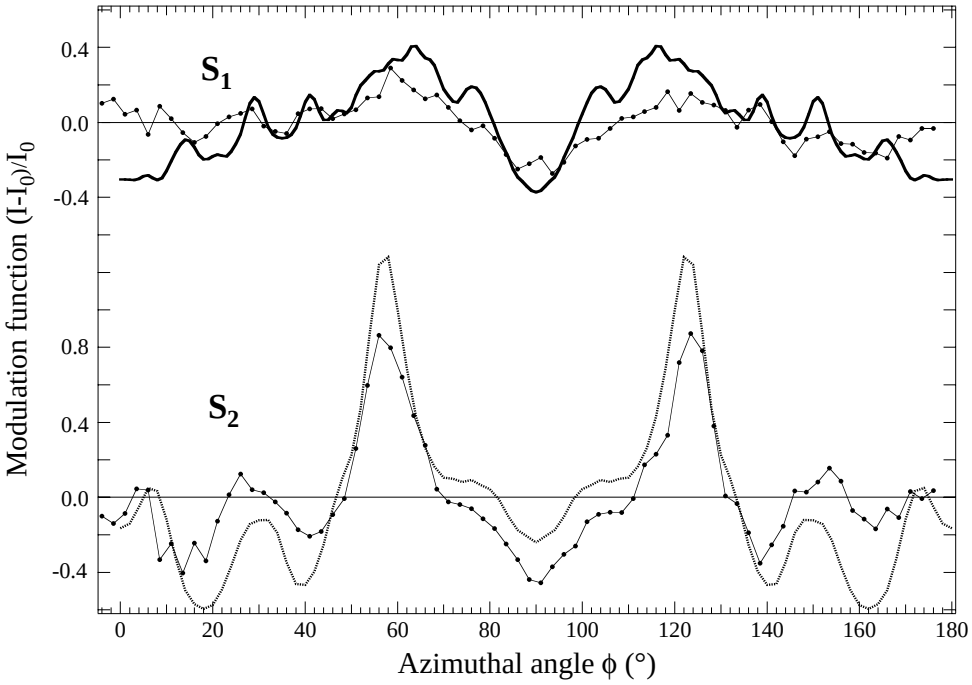

Figure 3.12: Measured (dots an thin line) and calculated (thick line) modulation function $(I - I_0)/I_0$ of first (upper) and second layer (lower) surface component for an azimuthal scan at a polar emission angle 75° off the surface normal.

apparent that the S_2 surface core level component shows pronounced maxima in the forward scattering direction and can therefore be assigned to the second layer atoms. Moreover, the simulated modulation functions, also shown in the figure, agree well with the experimental data. As a result we clearly prove that the larger Ru $3d_{5/2}$ surface core level peak, S_1, originates from the first layer atoms, while the smaller SCLS peak, S_2, stems from the second layer atoms in agreement with a simple initial state-based view. We stress that the situation is different from the Be(10$\bar{1}$0) surface where the

ordering of S_1 and S_2 is reversed.

3.2.3 Discussion

We can interpret our results using a tight-binding initial-state model which describes the SCLS only in terms of band narrowing, as explained in sect. 1.2.1 [28, 77]. In this framework, considering eq. 1.53, the SCLS is simply proportional to the narrowing of the d band caused by the bond breaking at the surface

$$SCLS \propto (\sqrt{\frac{Z_{surface}}{Z_{bulk}}} - 1) \tag{3.1}$$

where $Z_{surface}$ and Z_{bulk} are the coordination numbers of surface and bulk atoms, respectively.

The LEED I/V structural investigation of Ru(10$\bar{1}$0) [65] has reported a preference for short first interlayer termination as for Be(10$\bar{1}$0) , where on a bulk-truncated ideal hcp crystal a first-layer atom has eight nearest neighbors and a second-layer atom ten (see fig. 3.3). By using eq. 3.1 for the Ru(10$\bar{1}$0) second and first surface layers, with coordination numbers for the ideal hcp structure Z_{S_1}=8, Z_{S_2}=10 and Z_{bulk}=12 we obtain a ratio of the second to first layer SCLS equal to 0.475. This value is in very close agreement with our experimental value of 0.5±0.03, suggesting that the simple model is adequate to describe at least the relative magnitude of the SCLS for Ru(10$\bar{1}$0).

The value for the first layer shift compares also well to a recent *ab initio* calculation based on density-functional theory which, in the initial-state approximation predicts a value of about -0.48 eV [30] as shown in fig. 1.7. It needs to be noted, though, that the latter calculations have been performed assuming an fcc(110) geometry where the coordination of the first layer atoms is different from that of hcp(10$\bar{1}$0). Moreover, the authors state that care has to be taken in using initial-state calculations for 4d transition metal surfaces and that in general the screening of the core-hole in the final state has to be taken into account.

A problem arises when we look at this result in comparison to the other 4d metal surfaces. Ru(10$\bar{1}$0) is in fact the first example of such a metal where a second layer core level shift has been clearly observed. For Pd(110) and Rh(110) even larger first layer shifts of -550 meV and -660 meV, respectively, are reported [78] but no shifted component for the second layer can be found. Applying the simple model from above would, however, predict shifts of -190 meV and -230 meV for Pd(110) and Rh(110), respectively. Such shifts could not have been overlooked in the careful experiments. One reason for this problem might be that the simple model does not take into account any final state effects. For Ru(10$\bar{1}$0) this does not seem to be much of a problem: the relative shifts for the two surface components obtained from our simple model agree well with the experiment and, moreover, the

line shape parameters required in the fit are the same for bulk and surface, indicating that the screening is very similar. For the other 4*d* metal surfaces final state effects could be much more important. The first layer final state shift for Pd(110), for instance, is of the order of +200 meV [78]. A similar effect in the second layer could be sufficient to compensate the initial state shift. For Rh(110) this seems less likely since the calculated final state shifts for all surfaces are rather small [78].
Another, more likely, reason for the failure of the tight-binding model to predict the right second layer shifts for Pd(110) and Rh(110) is simply the difference between the hcp (10$\bar{1}$0) and the fcc(110) structure (see fig. 3.3 and fig. 3.13). For the short termination of hcp(10$\bar{1}$0) the second layer

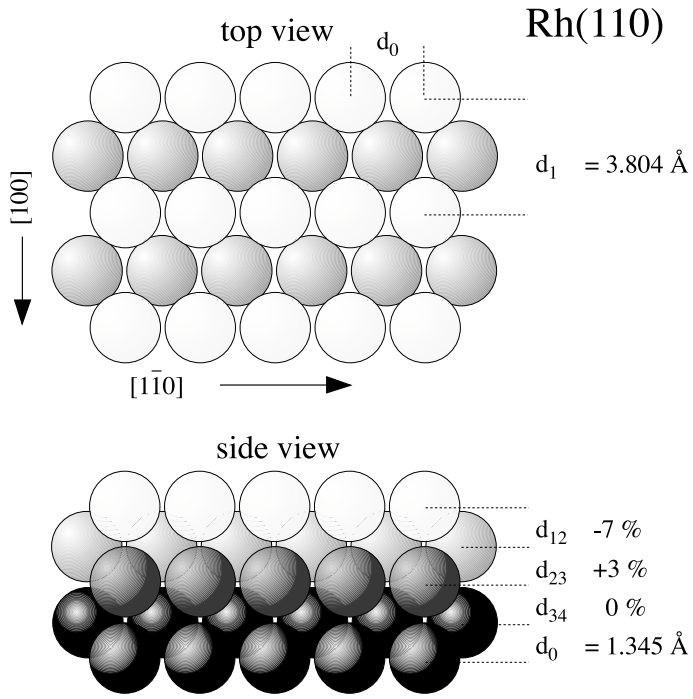

Figure 3.13: Surface structure of Rh(110) [79].

is much more surface-like then for fcc(110). The first reason for this is that the hcp(10$\bar{1}$0) second layer atoms lose two nearest neighbors while the fcc(110) second layer atoms only loose one. The second is that the first interlayer spacing normalized to the nearest neighbor distance is smaller for hcp(10$\bar{1}$0) than for fcc(110). Therefore the fcc(110) second layer atoms are embedded in a more bulk-like electron gas. In such a situation the simple tight-binding model might be inadequate. This view is consistent with the findings of Wertheim and Citrin that the same model gives a fair description for the relative magnitude of the first and second layer SCLS of W(111) but

it overestimates the shift for the third layer [77]. These speculations could easily be verified by a state-of-the-art *ab initio* calculations of the $4d$ second layer core level shifts for different structures.

3.3 Ru(0001)

The two SCLS investigations described above show that it is possible to detect and assign the SCLS of deeper layer atoms for the open $(10\bar{1}0)$ surface of Be and Ru. Moreover, as mentioned in the Be section, the Be(0001) $1s$ core level displays up to four shifted components and this unusually large number of SCLS's is due to the presence of strong surface states that penetrate into the deeper layers of Be. In the case of Ru$(10\bar{1}0)$ the two $3d$ core level shifted components are related to the narrowing of the $4d$ band of the first and second layer atoms that loose four and two nearest neighbors respectively. Now, let's see what's happening in the case of the closed packed Ru(0001) surface. Here, the first layer atoms lose three nearest neighbors while the second layer atoms are fully coordinated. Therefore, in the initial state picture, the latter atoms should not display any shift in the core level energy.
In the following we show that this is not the case because the Ru $3d_{5/2}$ core level of the Ru (0001) surface displays three components related to bulk, first and second layer. Again, as for the previous surfaces, we made the assignment of the different components following the same experimental procedure of photoelectron diffraction in the forward scattering regime. Moreover, in order to find the physical reasons of the measured SCLS we compared our experimental results to first principles calculations.

3.3.1 Experimental

The Ru(0001) crystal was prepared with the same procedure used for cleaning the Ru $(10\bar{1}0)$ surface, explained in section 3.2. After the final flash to 1500 K the sample was cooled down to 300 K in 1×10^{-7} mbar hydrogen pressure in order to remove any residual trace of oxygen from the oxygen treatment; to remove the hydrogen, the sample was briefly heated to 500 K in UHV before measurements. A very sharp (1×1) LEED pattern with low background intensity was obtained and the XPS did not show any trace of carbon, oxygen, or other contaminants.
The SCLS spectra, both in the high resolution and diffraction experiment, were acquired at a sample temperature lower than 130 K and at a base pressure of 6×10^{-11} mbar. The high resolution Ru $3d_{5/2}$ SCLS spectra were recorded at a photon beam incidence angle of 80° from the surface normal; in the used machine this leads to an electron emission angle of 40°. Three different photon energies, 352, 370 and 400 eV were used in order to change

the weight of the core level components due to diffraction and inelastic scattering effects. The combined (photon plus electron) energy resolution is estimated to have been better than 80 meV.
For the photoelectron diffraction measurements on the clean Ru(0001) surface, we used a photon energy of 500 eV, which corresponds to a kinetic energy of the Ru $3d_{5/2}$ core level of 220 eV, high enough to have strong forward scattering effects. We performed an azimuthal scan at 40° emission angle with the photon beam now parallel to the surface normal. Since at this high photon energy the cross section for photoemission is quite low, we lowered the overall energy resolution to 120 meV.

3.3.2 Results

In fig. 3.14 the three SCLS spectra of the Ru(0001) surface, measured at the three photon energies given, are shown together with the fits. We normalized the spectra at the low binding energy side and fitted them using three Doniach-Ŝunjić functions convoluted with Gaussian broadening [16]. The background was assumed to be linear. We measured and fitted the spectra, between 277.9 eV and 281.8 eV in a wider range than shown in the figure. In the fit we kept the Lorentzian width the same for the three components, letting free the asymmetry and the Gaussian width. Fitted this way, the Lorentzian width is 0.18, the asymmetry turns out to be the same for all components, 0.086, and the Gaussian width of the S_1, S_2 and bulk peak is 0.13, 0.09, and 0.08 respectively. The derived SCLS's are: $S_1 = -360 \pm 10$ meV and $S_2 = +127 \pm 10$ meV.
Among the three peaks present, the only one which can be unambiguously assigned is peak b, which belongs to the bulk. This results from the fact that when saturating the surface with CO or other adsorbates, the only peak which remained unchanged was peak b. From a simple inspection of the data it is possible to see that peak b increases at higher photon energy, consistent with a simple mean free path picture. The peak at lower binding energy, S_1, has maximum intensity at 370 eV and the component at higher binding energy, S_2, is more or less constant.
From these data it would not be possible to disentangle the various components accounting only for inelastic scattering effects. In fact, the strong modulation of the lower binding energy peak, which will be assigned to the top layer as we show in the following, is mainly due to interference effects, i.e. to photoelectron diffraction, and not to inelastic damping. Therefore we used these interference effects to find the right assignment of the peaks of the Ru $3d_{5/2}$ core level. In particular, we performed a photoelectron diffraction experiment changing the azimuthal angle ϕ at sufficiently high kinetic energy and at the appropriate polar angle θ (for the clean Ru(0001) θ=36°) to see the photo-emission intensity of the second layer strongly modulating due to the forward scattering with the first layer atoms.

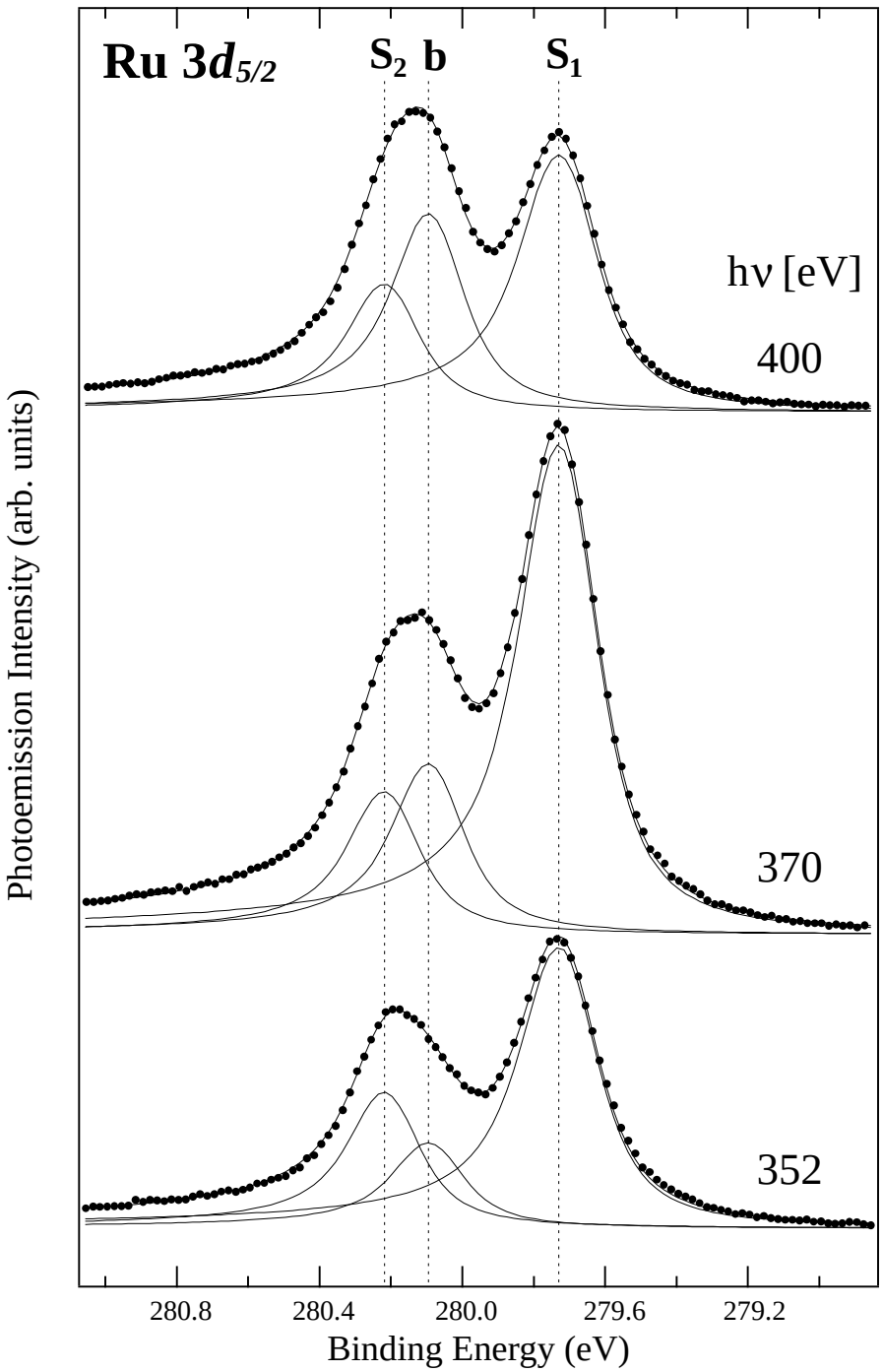

Figure 3.14: SCLS spectra of the clean surface measured at different photon energies. The result of the fit is added in the figure as a line crossing the experimental points represented by dots. The three components b, S_1, and S_2 are also added as solid lines. The energy range used to fit the data is wider than what is shown in the figure (see text).

The problem, which arises in this experiment, is that at kinetic energies high enough to have mainly forward scattering effects, i.e. higher than ≈400 eV, and low emission angle, the intensity of the photoemission from the first layers will decrease appreciably with respect to that from the bulk. This will affect much more the S_2 peak, which is very close to the bulk peak, thus making it almost undetectable.
In order to overcome this problem, we performed preliminary multiple scattering simulations of the first and second layer photoemission intensity using the MSCD package developed by Chen and Van Hove [55]. As input to the program we used the structural parameters obtained from a previous LEED I/V experiment [80]. Moreover, since the Ru(0001) surface is composed by domains rotated by 120° to each other, as shown in fig. 3.15, we summed the photoemission intensity over these domains. At the end we calculated

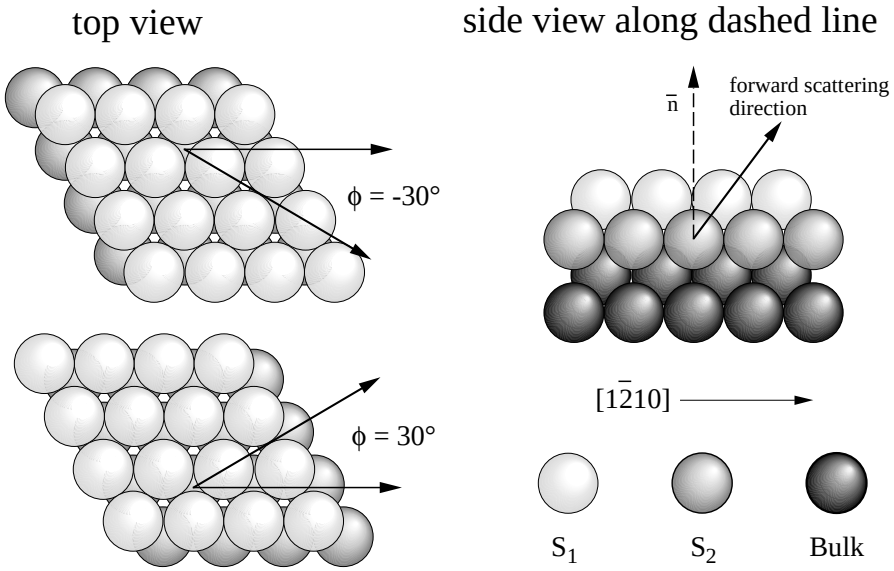

Figure 3.15: Sketch of the forwards scattering geometry for the Ru(0001) surface. In the figure are illustrated the two different domains rotated by 120° to each other.

the modulation function defined as $(I(\phi) - I_0)/I_0$, where $I(\phi)$ is the photoemission intensity, while I_0 is its average value.
From these calculations we found the best conditions to perform the photoelectron diffraction experiment. In particular, we realized that when performing an azimuthal scan at θ=40° at a kinetic energy of 220 eV, not only the first layer intensity shows pronounced modulations due to the backscattering, but furthermore these are in antiphase with those of the second layer emission in which the characteristic forward scattering peaks are present at ϕ=±30° with respect to the [1$\bar{2}$10] direction. The photoelectron diffraction experimental results together with the multiple scattering simulations are

shown in fig. 3.16. The agreement between experiment and simulation is

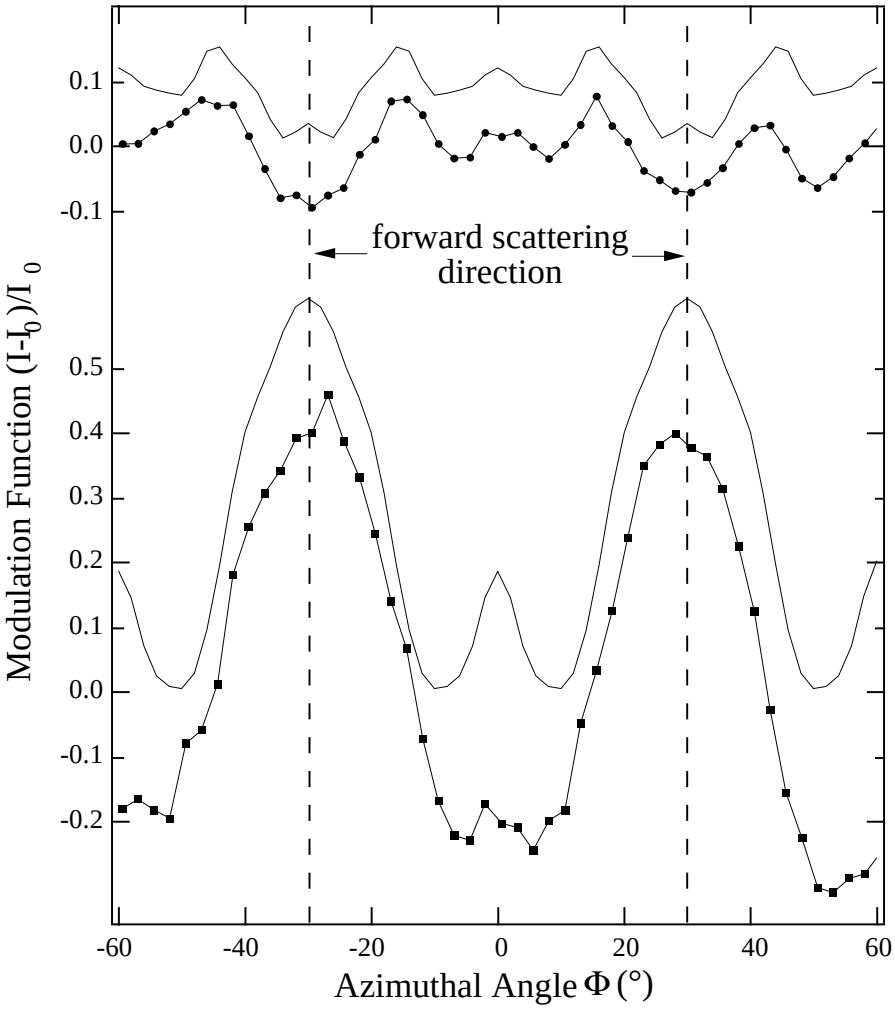

Figure 3.16: Angular dependence of the modulation function of the S_1 (open circles) and S_2 (filled squares) components shown in fig. 3.14. The S_2 component shows a clear enhancement of the intensity in the forward scattering directions, denoted by the dashed lines in the figure. The solid lines represent the results of multiple scattering simulations. These two curves have been shifted with respect to each other for display purposes.

very good, hence giving a clear answer to the question we addressed: S_1 belongs to the first layer atoms, while S_2 to those of the second layer.

3.3.3 Discussion

Having achieved an unambiguous assignment of the three experimentally detected peaks, the next step is to understand the physical reasons of these

Table 3.2: Comparison between the experimental and calculated Ru $3d$ SCLS's for the first and second layer atoms. Shown are the total shifts, as well as their decomposition into screening and initial state parts: $\Delta_{\mathrm{SCLS}}^{\mathrm{total}} = \Delta_{\mathrm{screen}} + \Delta_{\mathrm{SCLS}}^{\mathrm{initial}}$. Units are meV.

	Experiment	Total	Initial	Screening
S_1	-360	-383	-285	-98
S_2	+127	+124	+196	-72

shifts. In order to do this we compare the experimental results to density functional theory calculations of the SCLS. These calculations were performed by K. Reuter in the Fritz-Haber-Institut, Berlin, Germany, using the Full-Potential Linear Augmented Plane Wave (FP-LAPW) method (WIEN97) within the generalized gradient approximation (GGA) of the exchange-correlation functional, as explained in sect. 1.2.3. The Ru(0001) surface is modeled using a six-layer slab with a vacuum region of five Ru interlayer spacings to decouple the surfaces of consecutive slabs. The initial state and full calculation of the $3d$ SCLS's were done for each Ru atom in the outermost two substrate layers using eqs. 1.82 and 1.84 respectively. The numerical accurancy of the calculations is estimated to be of ± 30 meV. The calculations permit to decouple the contributions of initial state and final state or screening effects to the SCLS. The results of such a calculation are shown in Table 3.2.

It can be noted that the screening contribution to the SCLS is quite small for the first layer, even smaller for the second layer atoms. However, this does not imply that it could be neglected, as only the full shifts lead to the good agreement with the experimental results. Infact, the initial state contribution alone fall far out of the experimental error bars. This is even more so for the small total shifts connected to second layer Ru atoms S_2. Here, the screening correction is of the same order of magnitude as the initial state shift itself and negative in sign as for the first layer atoms.

Methfessel and coworkers have shown that final state effects at clean, true transition metal surfaces are largely due to intra-atomic d-electron screening [29, 30, 78]. Upon core excitation, the d-DOS shift to lower energies causes a valence electron from the Fermi reservoir to restore local charge neutrality by filling up formerly unoccupied d-states. Due to the lowered coordination at the surface, the local density of d-states (d-DOS) is narrower in energy compared to the d-DOS of a bulk atom. Because the total number of states in a band is conserved, already in the simplest rectangular d-band model with a constant d-DOS [81] one would then expect the d-DOS value at and

above the Fermi level to be enhanced compared to the bulk situation. This can be appreciated in fig. 1.6. In turn, this enhancement implies that the core hole be more efficiently screened at the surface, which in our present sign convention leads to a negative screening correction, i.e. towards higher kinetic energies. It has to be noted that in the case of a less than half full d-band the d-DOS is shifted down in energy due to the narrowing and hence a negative initial state contribution to the SCLS results. However, the enhancement of the d-DOS at and above the Fermi level nevertheless leads to a negative screening contribution.
In fig. 3.17 the real self-consistent 4d-DOS, calculated inside the muffin tin spheres for the Ru(0001) surface and the bulk, is shown. Compared to the

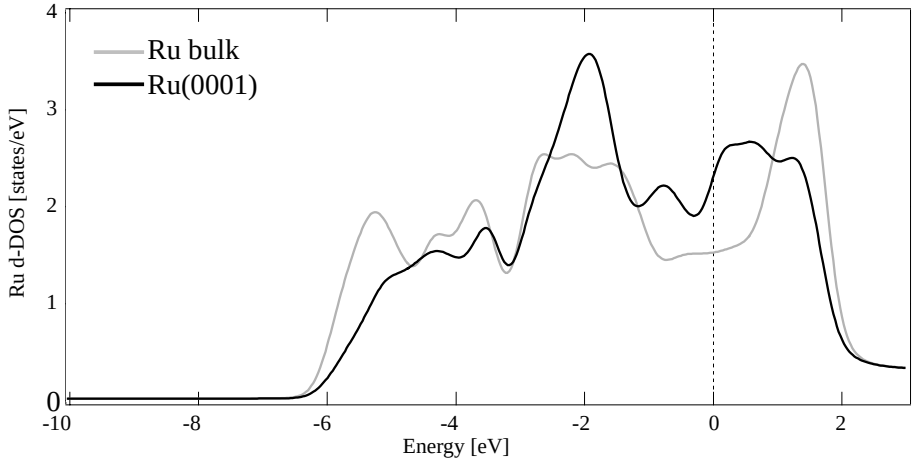

Figure 3.17: Calculated 4d-DOS for bulk Ru atoms (solid line) and for first layer Ru(0001) atoms. The energy zero is at the Fermi level.

bulk situation, the first layer d-DOS is indeed narrower in energy and in the energy range at and above the Fermi level it is strongly enhanced. Consequently, negative screening contributions are found for the top layer atoms. Having subtracted off the final state effect from the total SCLS's, we are now in a position to discuss the initial state contribution, i.e. the change in the local (near nucleus) electrostatic field (see below). For clean transition metals, these shifts are well understood in terms of the narrowing of the surface valence d-band due to the lowered coordination, as explained in sect. 1.2.1 [24]. This narrowing induces a positive SCLS for the early and a negative SCLS for the late transition metals. This trend involving a sign change across the series is well confirmed by a number of experimental and theoretical studies [13, 24, 29, 69, 78], into which the derived negative $\Delta_{\mathrm{SCLS}}^{\mathrm{initial}}$ for the top layer Ru(0001) fits nicely.
In order to quantify the d band shift and relative width change, let's consider the first and second moment of the valence 4d-band for the top layer

atoms and for the bulk. From this calculation it turns out that the 4d-band at the surface is 12% narrower than that of the bulk and its center of gravity is hence shifted by $\approx$ 0.2 eV to higher energies which accounts for the calculated initial state shift of table 3.2.
Let us focus now on the second layer shifts. Here, the S_2 type atoms display relatively large shifts of $\approx$ 200 meV towards higher binding energy. Evaluating again the first and second moment of the d-DOS for the second layer atoms, it can be seen that the width has increased by 5% with respect to the bulk value together with a corresponding shift of the 4d-band center to lower energies, which gives rise to their positive SCLS's. This is quite unexpected because the second layer Ru atoms always have the same number of nearest neighbours as in the bulk. In this respect it is interesting to notice that the S_2 atoms have first layer neighbours which are not fully coordinated and which hence have somewhat unsaturated bonds. We thus argue that the first layer atoms will most likely reinforce their backbond to the second layer atom below, which will then experience stronger binding than in the bulk situation. Note that this is also reflected in the contraction of the first layer distance with respect to the bulk [82, 83].

3.4 Conclusions

In this chapter we have presented the SCLS studies performed on the clean Be(10$\bar{1}$0), Ru(10$\bar{1}$0) and Ru(0001) surfaces.
We have started with Be(10$\bar{1}$0) because this surface is particularly suitable for the quantitative understanding of SCLS's due to the high number of shifted components present in the Be 1s core level. In particular, we have found that our experimentally determined SCLS's of Be(10$\bar{1}$0) are in good agreement with first principles calculations only when the assignment is such that the second layer gives a stronger SCLS than the first layer. We have confirmed this novel and unusual assignment in a straight forward way using high resolution angle-scan photoelectron diffraction. The reason of this unexpected behaviour is that the physics leading to the core level shifts is an involved interplay between initial and final state effects. In any experiment dealing with surface core level shifts caution should be taken as to the assignment. The experimental procedure outlined here can be extended to other systems once the geometric structure of the surface is known.
We have then moved to the Ru(10$\bar{1}$0) surface where we have found that the 3$d_{5/2}$ surface core level spectrum exhibits three components, as opposed to the findings for the other 4d transition metals. Photoelectron diffraction measurements have shown here that the larger SCLS is linked to the first layer atoms. Simple considerations and the line shape parameters obtained from fitting the spectra suggest that final state effects are not very important in this case. We suggest that the reason why second layer core level shifts are

observed here and not on the other $4d$ surfaces lies mainly in the structural difference between hcp($10\bar{1}0$) and fcc(110). A simple tight-binding view of the SCLS which works for hcp($10\bar{1}0$) might fail for fcc(110) because there the second layer atoms are too bulk like.
Finally we have studied the close-packed Ru(0001) surface where the second layer atoms are fully coordinated. Also in this case, and contrary to what one would expect, the second layer atoms give rise to a shifted component in the Ru $3d_{5/2}$ core level spectra towards higher binding energy with respect to the bulk component. We used the high energy resolution photoelectron diffraction approach in order to make the assignment of the measured shifts to the corresponding substrate atoms. We obtain very good agreement between the experimentally determined SCLS's and first principles calculations. The theoretical approach permits to separate the total SCLS's into initial and final state contributions. The latter are mainly due to an enhanced intra-atomic $4d$-electron screening while the initial state shifts are connected to a varying width of the Ru valence $4d$ band. We observe a band narrowing for the top layer atoms which have reduced coordination with respect to the bulk, and a band broadening of the $4d$ band of the atoms of the second layer, because of the reinforced bond to the top layer atoms. This last effect is also reflected in the contraction of the first interatomic distance, as observed from previous studies.

Chapter 4

Thermal expansion via SCLS

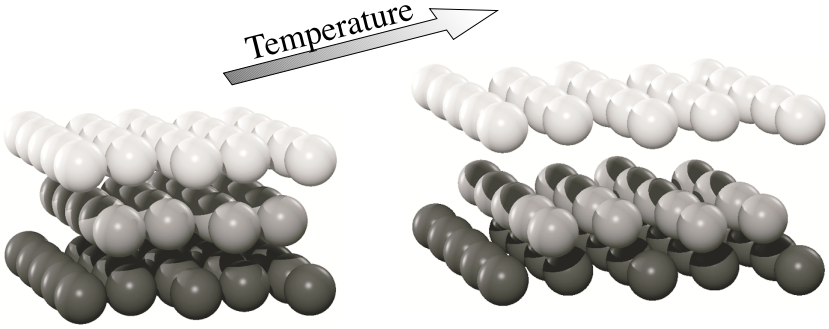

Figure 4.1: Effect of a temperature increase on the Be(0001) surface. The three topmost layers are shown with different grey scale. Upon heating the first interlayer distance is strongly expanded while the distance between second and third layer slightly contracts. These effects are exaggerated in the drawing for displaying purpose. The corresponding behaviour of the SCLS is explained in sect. 4.2.

The previous chapter dealt with the issues associated with the presence of more than one shifted component in the core level spectra of the low index surfaces of Be and Ru. The most notable result in this sense is that a good description of the SCLS's can be achieved only when theoretical calculations are performed that take into account initial and final state effects in the photoemission process. In this case the measured shifts can be reproduced with high accurancy by first principles calculations. In order to avoid vibrational broadening of the core level peaks which would prevent a detailed and precise measurement of the SCLS's, the samples were kept at a constant, low temperature (120 K) during the experiments.
Now, let's see what happens when the temperature increases. Obviously the peaks broaden but what about the SCLS's?

In order to understand the possible temperature effects on the SCLS we consider the structural changes of a solid upon heating (see fig. 4.1). Thermal expansion can take place due to the anharmonicity of the interatomic forces. In fact, for a harmonic interatomic potential a temperature change should affect just the vibrational amplitudes and not the mean positions of the atoms. Thus, the observed expansion upon heating can be attributed to the presence of anharmonicity of normal modes of lattice vibrations. Only recently has it become possible to correctly describe the bulk thermal expansion of simple metals within the quasiharmonic approximation [84, 85].
At the surface of a solid the situation is much more involved than in the bulk because the surface is formed by breaking the symmetry of the solid along a certain direction, and lowering the coordination of surface atoms. Therefore the thermal motion of the surface atoms should be larger and presumably with enhanced anharmonicity in the interlayer potential. For this reason, as the temperature is increased, this anharmonicity can lead to large anisotropic vibrations, more pronounced at the outermost layer, which results in a change of the interlayer separation. This phenomenon currently receives a lot of attention both from the theoretical [85, 86, 87] and the experimental [87, 88] side.
Since the SCLS is directly related to the bond between atoms, and therefore to the structure, changing the distances between different layers should change also the SCLS.
In this chapter we show that this is the case both for the $3d_{5/2}$ SCLS of Rh(100) and the $1s$ SCLS of Be(0001). In particular in this latter case we show how the comparison of the temperature behaviour of the measured SCLS's with theoretical calculations can be used to find the thermal expansion of the Be(0001) surface.

4.1 Rh(100)

The SCLS is strictly related to the differences in the electronic and geometrical structure of the atoms in the first and in deeper layers of a solid. The availability of synchrotron radiation has prompted a large number of experimental studies on $4d$ transition metals [89, 90, 91, 92, 93, 94, 95], while a complementary effort has been devoted by theoreticians to an attempt of reproducing the experimental results and interpreting the nature of this phenomenon [29, 30, 69, 78, 96].
The important point outlined in such calculations is that even small variations of the structural parameters can sensitively affect the SCLS's. As an example, the theoretical work of Andersen *et al.* [78] predicts that the transition metal $3d$ SCLS decreases as the first inter-layer distance increases. Due to the extreme difficulties of measuring SCLS variations for these core levels which are very small, an experimental confirmation of this effect has

never been provided so far.
The temperature dependance of the Rh $3d_{5/2}$ core level of the Rh(100) surface is the subject of the present section.

4.1.1 Experimental

The Rh(100) sample was cleaned by repeated sputtering, annealing and oxidation-reduction cycles [97]. Surface cleanness from carbon and oxygen was checked by measuring the C1s and O1s signals (detection limit of 0.005 ML). The high-energy resolution photoemission measurements were performed using a photon energy of 398 eV with an overall energy resolution of 65 meV.
A sequence of spectra of the $3d_{5/2}$ Rh(100) region was measured as a function of the sample temperature, according to the following procedure. The sample was brought to the selected temperature, then a photoemission spectrum was acquired in about 90 s and finally the sample was flashed to 620 K. This procedure prevents CO, H_2 or H_2O surface contamination from the residual chamber atmosphere, which would reduce the SCLS, as previously shown [91, 92, 93, 95].

4.1.2 Results

Figure 4.2 shows a Rh$3d_{5/2}$ core level photoemission spectrum acquired at 20 K. As previously reported [92] the higher binding energy (BE) peak arises from the atoms in the bulk while the lower BE peak originates from the first atomic layer. Spectrum decomposition into bulk and surface components has been performed by fitting the data using two peaks with Doniach-Sunjic (DS) lineshape [16]. The two DS peaks, which were allowed to have different α and Γ, were convoluted with Gaussians in order to account for the experimental, phonon, and any possible inhomogeneous broadening. A linear background was also added to the fit.

The result of the fitting procedure is shown in fig. 4.2 as a solid line. Individual peaks are also shown as dotted curves. The value of the SCLS we find, 0.655±0.005 eV, as well as the values of the lineshape parameters reported in the figure caption, are in good agreement with previous experimental results [91, 92, 93, 95]. In our case however, the Gaussian widths are much lower, as a combined consequence of the higher resolution and lower temperature of our experiment.
The values of the α and Γ parameters obtained from the low temperature spectrum have been fixed in order to fit the data at the higher temperature. Besides the BE's of the two peaks, only the gaussian widths have been used as free parameters in a least-square analysis, accounting for the expected increase in phonon broadening.

The set of spectra measured as a function of the sample temperature from

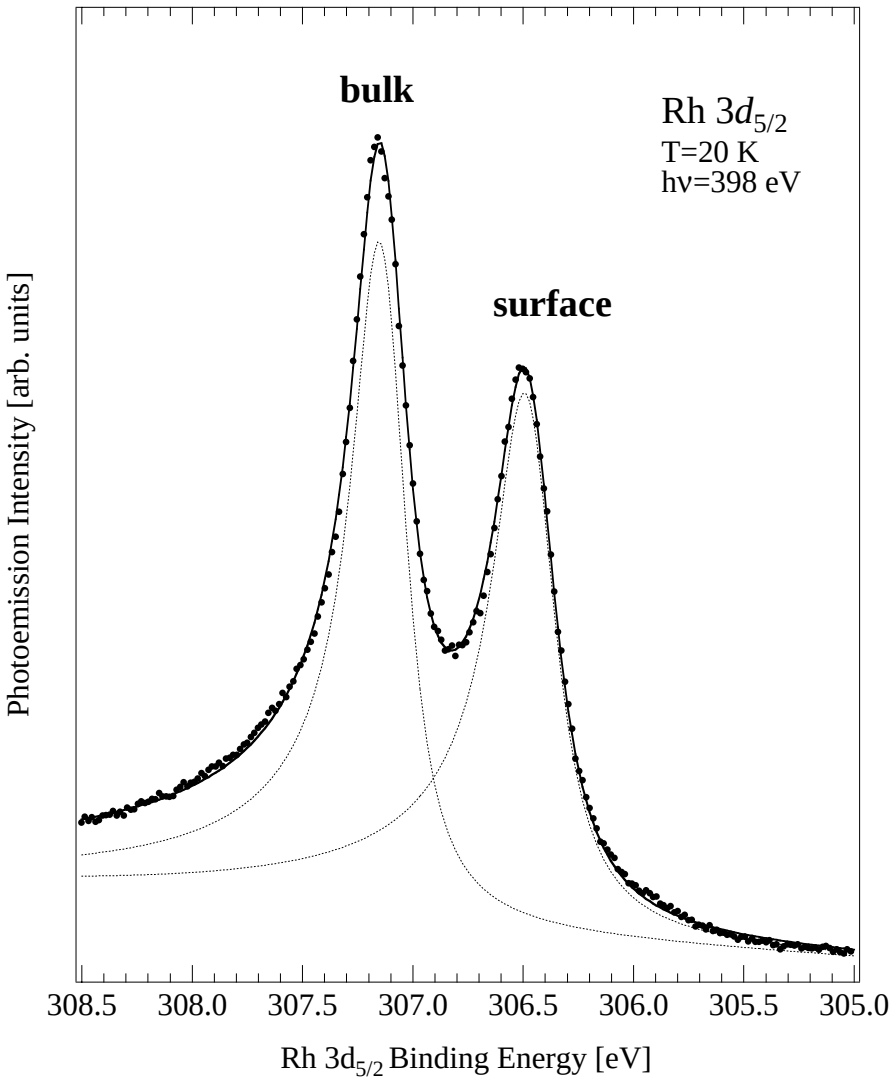

Figure 4.2: Photoemission spectrum of the Rh(100) $3d_{5/2}$ core-level measured at 20 K (photon energy of 398 eV). Full circles indicate experimental data; the fit is shown as a solid line while dotted lines represent the bulk and surface components. Fit parameters: α_{bulk}=0.18, Γ_{bulk}=0.22 eV, α_{surf}=0.17 and Γ_{surf}=0.27.

20 K to 970 K is plotted in fig. 4.3. As a result of the fitting procedure two effects can be distinguished. First, both the bulk and surface components shift to lower binding energies as the temperature increases. The bulk peak BE changes by ≈55 meV between 20 K and 970 K, while the surface-peak shifts by ≈25 meV. As a consequence the temperature dependent SCLS, which is plotted in fig. 4.4, decreases by ≈30 meV between 20 and 970 K.

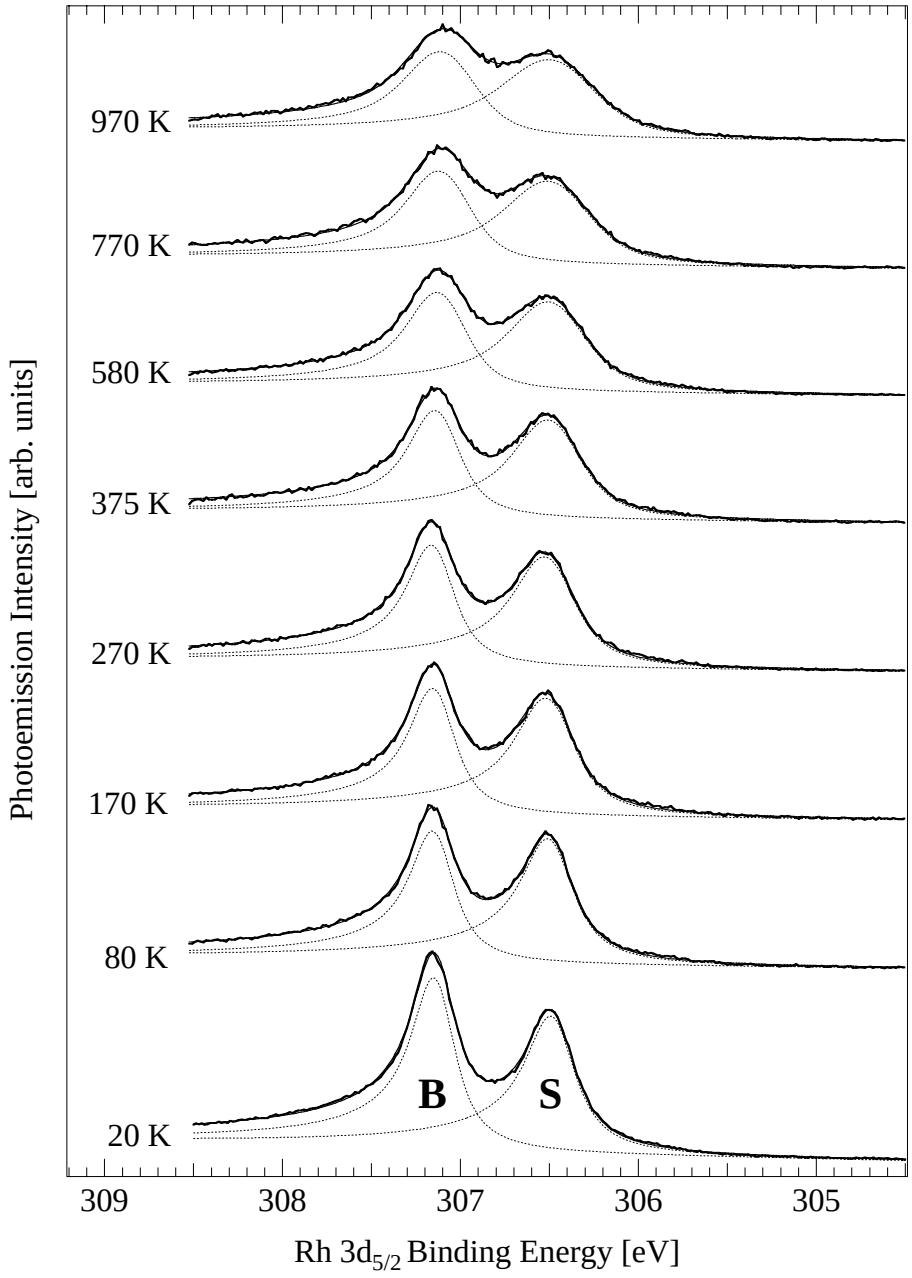

Figure 4.3: Photoemission spectra and corresponding fits of Rh(100) $3d_{5/2}$ core-level measured at temperatures ranging from 20 K to 970 K (photon energy of 398 eV).

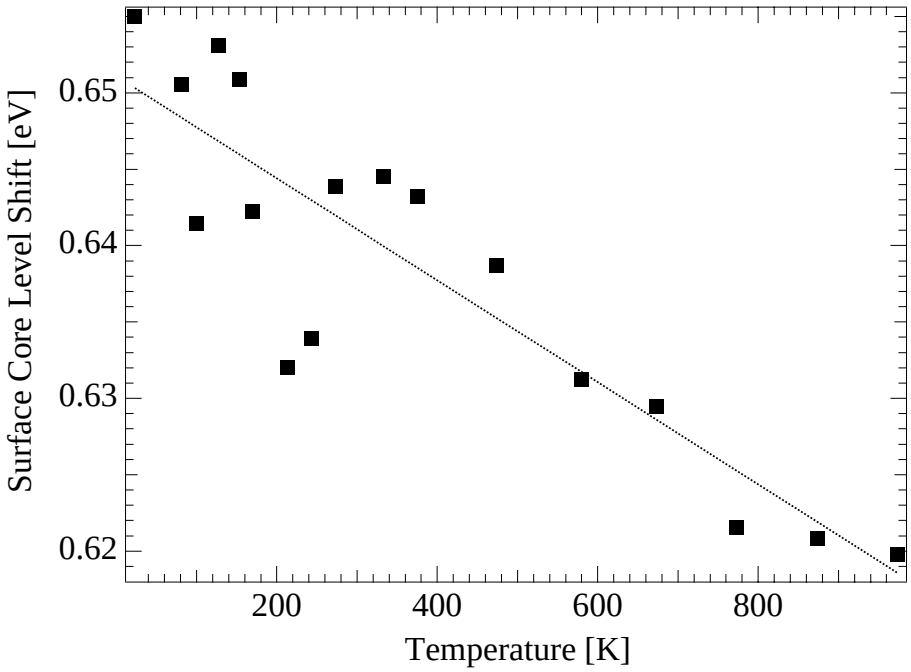

Figure 4.4: Temperature evolution of the Rh(100) $3d_{5/2}$ Surface Core Level Shift.

Secondly, both the surface and bulk components increase their width as the temperature rises.
The width includes two different contributions, namely the experimental resolution and the phonon broadening. The latter is shown for our data in fig. 4.5, where the square of the gaussian width for the surface and bulk peaks is plotted against the sample temperature after subtraction of the experimental resolution. At 20 K the total gaussian width is about the same for the two components, but for higher temperatures the surface peak width grows more rapidly than the bulk one.
We checked that the decrease of the SCLS is a genuine experimental result and not an artifact of the fitting procedure. Figure 4.6(a) shows the residual of two fits of the highest temperature data (T=970 K). In one case the SCLS was kept constant and equal to the values determined at low temperature (top) and in the other the SCLS was left free to vary (bottom). It is clear that only in the latter case is the experimental data reproduced satisfactorily. Morevover the chi-square of the fit of the highest temperature spectrum (fig. 4.6(b)) shows a clear minimum at 0.620 eV, a value which is significantly lower than that obtained for the 20 K spectrum.

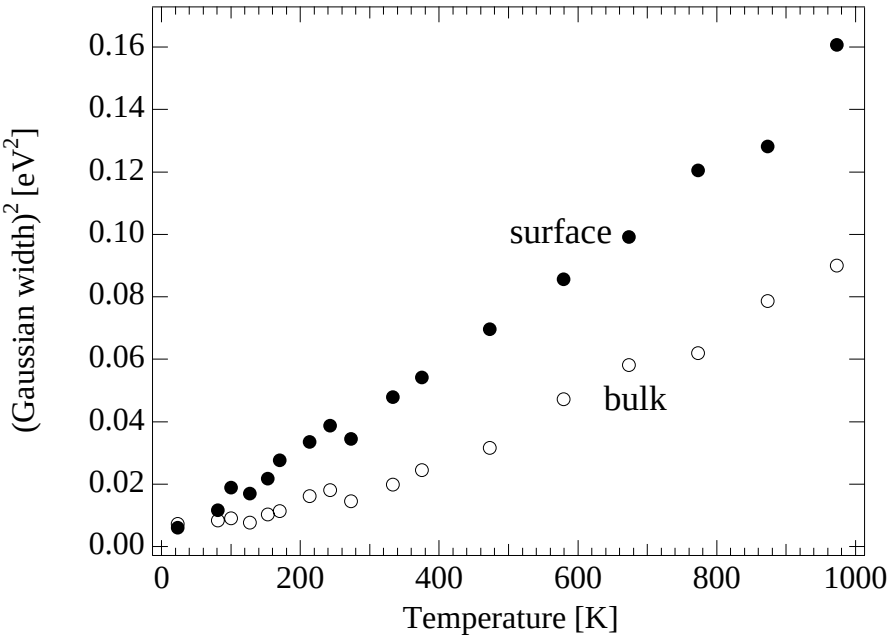

Figure 4.5: Temperature evolution of the square of the intrinsic gaussian width of the Rh(100) $3d_{5/2}$ core level, after quadratic subtraction of the intrumental resolution.

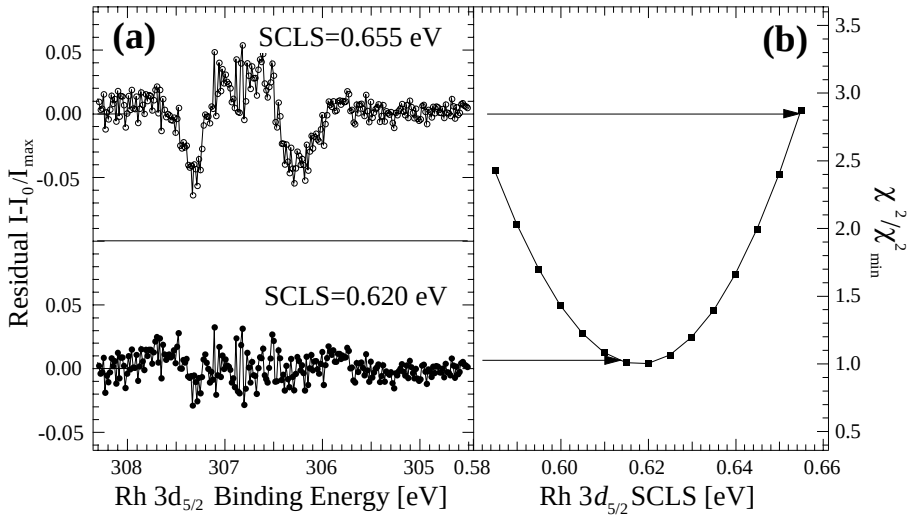

Figure 4.6: (a) Residuals of the fits of the Rh(100) $3d_{5/2}$ core level spectrum measured at 970 K: (bottom) SCLS as a free parameter; (top) SCLS constrained at the value obtained for the 20 K spectrum. (b) Goodness of the fits (chi-square) as a function of the Surface Core Level Shift.

4.1.3 Discussion

The observed temperature dependence of the SCLS can be understood by taking into consideration the different anharmonicity of the surface and bulk interatomic potentials. Because of the lower symmetry, the anharmonicity at the surface is expected to be larger than that in the bulk, and therefore the first interlayer spacing increases with the temperature more than in the bulk. Indeed in a recent theoretical study Xie and Scheffler [98] predict for the Rh(100) surface that the surface relaxation $\Delta d_{12}/d_0$ goes from -2.5% at 0 K to -0.5% at 600 K, with a surface thermal expansion coefficient that at 300 K is 5 times larger than in the bulk. At 770 K, where on the basis of the above mentioned theoretical results the surface relaxation is expected to be approximately 0%, we measured a SCLS of 0.62 eV.
This value is in extremely good agreement with the result of first-principles calculations by Andersen *et al.* [78], who predict a SCLS of 0.62 eV for $\Delta d_{12}/d_0$=0%. Moreover, they calculated also that a larger SCLS, as we measure at lower temperatures, corresponds to contracted first interlayer distances. Our data therefore clearly support the theoretical predictions that there is an inward relaxation of the Rh(100) surface at room temperature, in contrast to the most recent LEED IV study which suggests an outward relaxation ($\Delta d_{12}/d_0$=+1.0±0.6%) [99].
Further information about the bulk and surface interatomic potentials could in principle be obtained by analyzing the observed gaussian broadening of the photoemission peaks. The higher slope of the square of the surface gaussian broadening with respect to the bulk one (see fig. 4.5) is an evidence of the existence of enhanced vibrations at the surface [100].
The presence of anharmonicity in the interatomic potentials though cannot be revealed directly in a simple way from the gaussian width data. Deviation from the temperature dependent linear behavior predicted by a theory based on the Debye model has previously been taken as evidence of the presence of anharmonicity in the potential energy surface (PES) [101]. This conclusion however has to be considered with care, as the cited theory assumes also that the shape of the inter-atomic potential for the final state ionised atoms and the initial state neutral ones is the same, and only the equilibrium distances change [102].
Using a different approach Theis and Horn [103] have shown that a deviation from the linear behavior does not necessarily require the existence of anharmonicity in the initial state PES, but can also be due to the presence of a quadratic coupling term in the Hamiltonian, i.e. a change in the force constant between the initial and final state PES. Further theoretical investigations, where the actual shape of the PES for both the initial and final state is considered, are needed in order to clarify this point.
The results of the present work also show that in general care must be taken when comparing experimental SCLS with theoretical predictions if low tem-

perature experimental data is not available.
Finally it is worth considering the role of the magnetic ordering which was recently experimentally demonstrated on this surface [104] in the change of SCLS. Calculations show [86] that the magnetic and non magnetic states of this surface are degenerate, while the electronic structure is strongly influenced by changes in the interplanar and intraplanar atomic distances. For this reason we believe that an interpretation of the present data which neglects magnetic effects is appropriate.

4.2 Be(0001)

The surface relaxation of metals has been the subject of many experimental studies. Many structural investigations using Low Energy Electron Diffraction and Photoelectron Diffraction have been published showing different results. There is nowadays no clear consensus neither on the magnitude nor on the direction of the relaxation of many systems. One of them is the Be(0001) surface.
A recent Low Energy Electron Diffraction (LEED) investigation [105] measured an anomalously large thermal surface expansion, 6 times larger than the bulk. The top-layer outward relaxation increased from +3.1 % to +6.7 % (with respect to the corresponding bulk distance) upon raising the temperature from 110 K to 700 K, yielding a first-to-second interlayer coefficient of thermal expansion $\alpha_{12} = (d_{12})^{-1}(\partial d_{12}/\partial T) = 70 \times 10^{-6}$ K^{-1}, 6 times the bulk value of 12 $\times 10^{-6}$ K^{-1}.

However, a subsequent density functional perturbation theory study [85], in which the free energy of the system was calculated from full vibrational dispersions, found an increase of the first-to-second layer distance of only 1.1% in the same temperature range, much smaller than the LEED result. At the same time the calculation correctly reproduced the bulk thermal expansion and the adequacy of the quasiharmonic approach for the surface was directly checked comparing with a first principles molecular dynamics simulation [85]. Thus we are left with the puzzling situation that the arguably most advanced calculation to date leads to a worse agreement with the experimental data than a much simpler approach. If the LEED results are correct, this would mean that some essential physics of the surface thermal expansion is not yet included in the state-of-the-art calculations.

These far-reaching consequences are based on a complex LEED analysis which necessarily involves problematic approximations. In this section, we present a novel, independent, approach to determine the thermal expansion of Be(0001). Our results confirm the anomalously large thermal expansion of the surface and establish Be(0001) as a firm experimental standard for advances in theoretical understanding.
Our strategy is to measure the binding energy of the surface state at the

$\bar{\Gamma}$ point of the surface Brillouin zone and the values of the surface core level shifts (SCLS) as a function of temperature. These data are then compared to calculated values for different geometries in order to determine the temperature-dependent interlayer distances.

4.2.1 Experimental

The Be(0001) surface was cleaned by cycles of Ar^+ sputtering at 670 K and annealing to 720 K. The sample was heated by a filament mounted behind it. During the measurements the heating current was chopped in order to avoid a possible influence of the magnetic field on the photoemission spectra. Surface order and cleanliness were checked by LEED and core level photoemission, respectively.
The Be 1*s* core level measurements were taken for photon energies between 126 and 134 eV at normal photoelectron emission and with 40° photon incidence. The combined analyzer and monochromator energy resolution was 60 meV. The surface state data has been taken with 95 eV photons in the same geometry and with a total energy resolution of 100 meV.

4.2.2 Results

The calculations have been carried out by S. de Gironcoli in SISSA, Trieste, Italy, with the PWSCF package [106], within the local-density approximation [40, 75], using separable pseudopotentials [107] and planewave basis sets up to an energy cut-off of 22 Ry. Technical details and the Be pseudopotential were the same used as in previous works on beryllium [85, 108]. In the study of the electronic surface state a repeated slab geometry with a 16-layer Be slabs separated by a ∼25 a.u. thick vacuum region (equivalent to 8 atomic layers) to decouple the surfaces, was adopted .
Be 1*s* core excitation energies in different surface layers were calculated from first-principles including final-state effects following the procedure of Ref. [109]. The error induced by the choice of a pseudopotential approach in the calculation of the core-level binding energy is of the order of 10 meV. A much smaller error is expected for the core-level *shifts*. From the comparison of the SCLS computed on super-cells with 12 or 16 Be layers and 1×1, 2×2 and 3×3 in-plane periodicity, the periodicity error is estimated to be less than 20 meV in the 12-layer 3×3 slab.

As a first attempt to discriminate between the two suggested thermal expansions [85, 105], we have examined the temperature dependence of the surface state binding energy at the center of the Brillouin zone, $\overline{\Gamma}$. In fig. 4.7 the experimental results are compared to the theoretical results obtained assuming the large thermal expansion reported in Ref. [105] and the small expansion reported in Ref. [85]. Our experimental data are clearly in much better agreement with the LEED results of Ref. [105]. However, the number

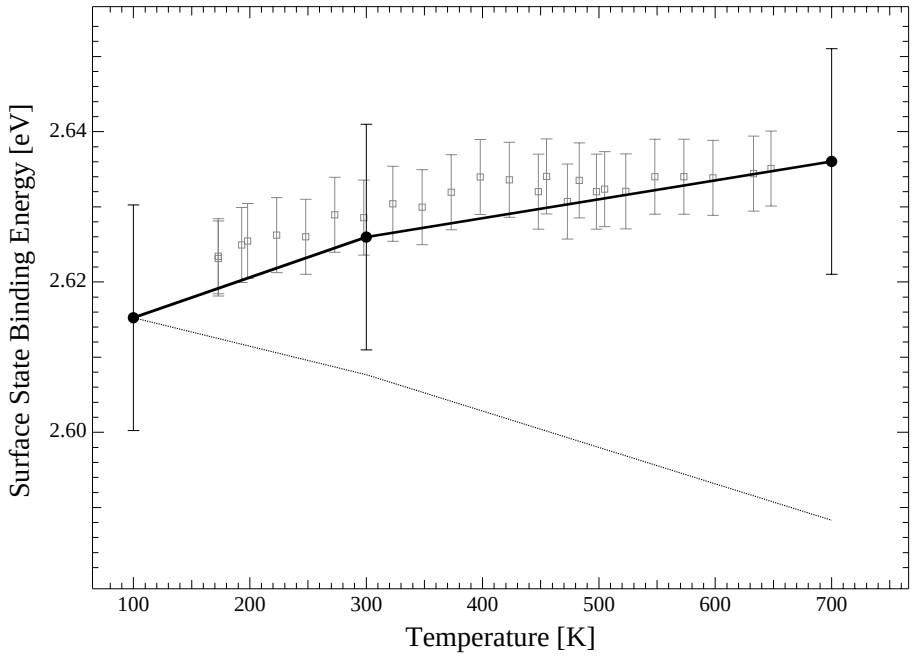

Figure 4.7: Temperature dependence of the surface state binding energy at $\overline{\Gamma}$ and a comparison with the calculated binding energies using the geometry determined by LEED in ref. [105] (solid line) and by first-principles calculations in ref. [85] (dotted line).

of layers involved in the surface expansion is large and the determination of the energy position of a single electronic surface state is not sufficient to fully constrain the multilayer relaxation pattern and to provide a clear-cut answer to our question.

A more detailed analysis is based on a measurement of the temperature-dependent Be 1s core level spectrum. This contains five components, which stem from the inequivalent surface, sub-surface and bulk atoms [110]. Therefore it gives us the opportunity to obtain information about the first layers separately. Fig. 4.8 shows six Be 1s spectra selected from the set measured at hν=134 eV and at 18 temperatures ranging from 173 K to 648 K. The five components of the spectra are emphasized in the 173 K spectrum. The high binding energy peak (B) originates from the bulk atoms, while the other four components (S_1, S_2, S_3, and S_4) arise from the four outermost atomic layers.
We fitted the data with five Doniach-Sunjic (DS) functions [16], convoluted with Gaussians to account for the instrumental, inhomogeneous and phonon broadening. In order to disentangle the various components in the spectra, we have measured the low temperature Be 1s spectrum using the same procedure as in Ref. [110], i.e. at 126, 130 and 134 eV photon energies, thus

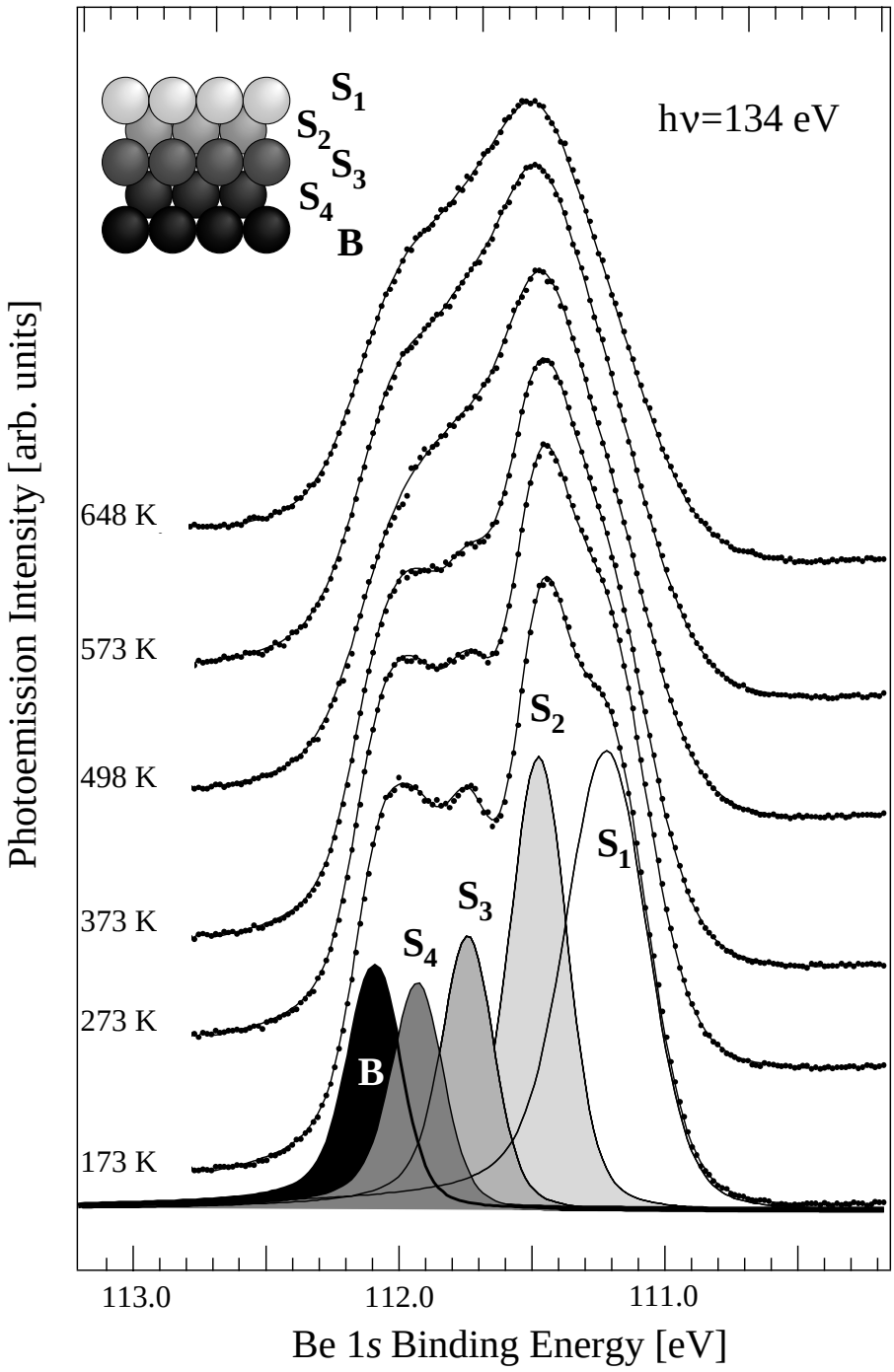

Figure 4.8: Be 1*s* core levels spectra from Be(0001) measured at temperatures ranging from 173 K to 648 K.

changing the relative weight of the different components. From the fit of the whole data set we obtained SCLS of 152±15, 317±5, 606±3 and 863±4 meV towards lower binding energy for S_4, S_3, S_2 and S_1 respectively, in close agreement with the previous results [110, 111]. Then we fitted the spectra measured at different temperatures and photon energies treating the binding energy position of the various components as free parameters except for the S_4 shift that was fixed at 152 meV from the bulk peak. All other lineshape parameters were fixed to the values found in the low temperature case, save the Gaussian widths that were left free to vary in order to mimic the vibrational broadening of the core-level lineshape.

It has to be noted that in a recent high-resolution core level photoemission investigation, Andersen *et. al.* [111] have shown that the Be 1*s* spectrum measured at 100 K contains internal fine structure caused by intrinsic excitation of a narrow band of optical phonons. Each surface core level component, apart for S_1, is composed by n replicas with an energy splitting of about 58 meV, which corresponds to the average energy of the excited phonon. In order to exclude any possible error in the analysis of the core level spectra, the temperature changes in the population of each phonon component have been calculated [112] according to ref. [113]. The resulting curves display the experimentally observed fine structure and once convoluted with a gaussian which describes our experimental resolution, and fitted to DS lineshape, indicate that the error in the peak position induced by the choice of a gaussian vibrational lineshape is less than 5 meV over the temperature range (173-648 K) of our measurements, thus justifing the procedure we used.

In fig. 4.9 and in Table 4.1 we report the experimental results for the temperature dependence of the different surface core level shifted peaks. While the SCLS corresponding to the first (S_1) and second (S_2) layer atoms decrease with temperature, the shift related to S_3 increases. The table also shows the calculated SCLS for a truncated bulk geometry at zero Kelvin, confirming the assignment of the peaks to the correct layers. In the temperature range investigated here the temperature dependence of the measured SCLS is approximately linear with slopes of -0.138 ± 0.010, -0.086 ± 0.006 and $+0.065 \pm 0.018$ meV/K for S_1, S_2 and S_3, respectively.

In order to interpret these findings and extract information about the temperature dependent surface geometry, the effect of the surface relaxation on the core-level shifts was theoretically studied.

The thermal expansion of Be(0001) can be split into two parts: *i*) an *homogeneous* expansion of the whole crystal according to the bulk thermal expansion coefficients that define for each temperature the two bulk *hcp* lattice parameters, $a(T)$ and $c(T)$, and *ii*) a *surface* expansion described by the percentual variation of the interlayer separation with temperature , scaled to the bulk interlayer separation at that temperature, $\lambda_{n,n+1} = d_{n,n+1}/d_{bulk}$, with $d_{bulk} = c(T)/2$. Since vibrational broadening does not significantly shift the peaks, the binding energy (BE) of a core hole in the n-th surface

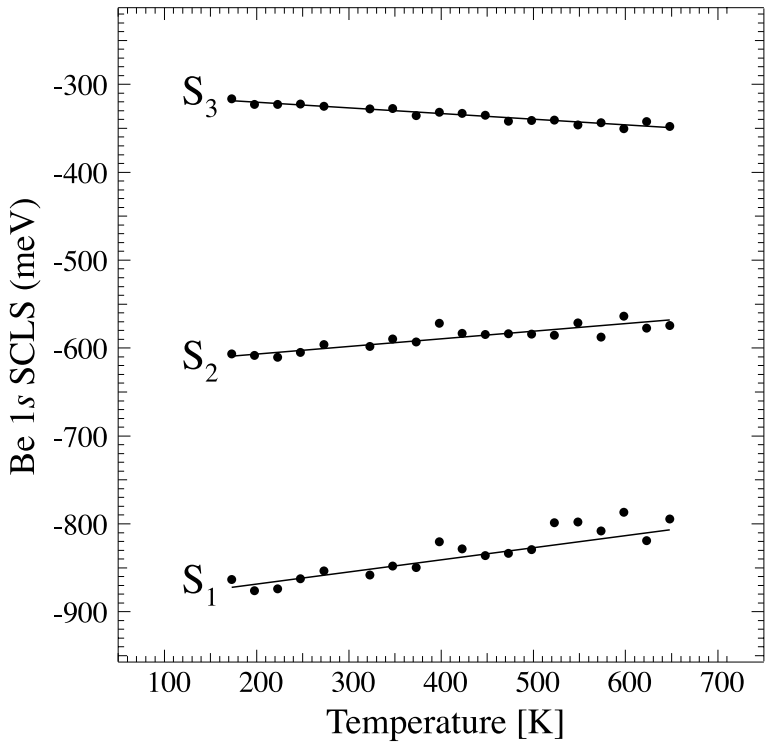

Figure 4.9: Be 1s SCLS's as a function of temperature. The S_4 component is not displayed. It was fixed at -152 meV from the bulk peak (see text). The temperature dependence of the measured SCLS is approximately linear (straight lines between the data points) with slopes of -0.138 ± 0.010, -0.086 ± 0.006 and $+0.065 \pm 0.018$ meV/K for S_1, S_2 and S_3, respectively.

layer at a finite temperature can be obtained from a static calculation in the expanded geometry:

$$BE_{S_n}(T) = BE_{S_n}(a(T), c(T), \{\lambda_{m,m+1}(T)\}). \tag{4.1}$$

The next step is to calculate the dependence of each SCLS, on the variation of any interlayer separation (d_{12}, d_{23}, ..). This dependence is remarkably linear for the expected interlayer variations and the full result can thus be obtained from the following expansion:

$$BE_{S_n}(T) = BE_{S_n}(a(T), c(T), \{\lambda^0_{m,m+1}\}) +$$

$$\sum_l \frac{\partial BE_{S_n}(a(T), c(T), \{\lambda^0_{m,m+1}\})}{\partial \lambda_{l,l+1}} (\lambda_{l,l+1}(T) - \lambda^0_{l,l+1}) \tag{4.2}$$

where the first term corresponds to the BE computed from the bulk thermal expansion only (the $\lambda^0_{n,n+1}$'s are the scaled interlayer separations obtained

Table 4.1: Measured surface core level shifts for several temperatures, and theoretical shifts for the relaxed surface slab homogeneously scaled with the bulk thermal expansion, *i.e.* the first term in the r.h.s. of Eq. (4.2) (energies in meV).

		S1	S2	S3	S4	S5
Expt.						
	173 K	-863	-607	-317	-152	—
	273 K	-854	-596	-325	-152	—
	373 K	-849	-593	-336	-152	—
	498 K	-829	-584	-341	-152	—
	573 K	-808	-587	-344	-152	—
	648 K	-794	-574	-345	-152	—
Theory:						
	a_{0K}	-898	-610	-282	-111	-30
	a_{300K}	-891	-607	-280	-110	-30
	a_{700K}	-866	-597	-277	-109	-30

from the static equilibrium) and the needed first order derivative of the core level BE in the n-surface layer is simply obtained from the change of the total force acting on the top l surface-layers of the slab when an atom in the n-th layer is excited.
In Table 4.2 we report the value of the derivatives (in meV per percentual variation of $\lambda_{n,n+1}$) calculated for the static equilibrium. Very similar values

Table 4.2: Theoretical results for the change in S_n SCLS position induced by a +1% variation in the l-th interlayer separation ($\lambda_{l,l+1} = d_{l,l+1}/d_{bulk}$). Values in meV.

$\frac{\partial BE_{S_n}}{\partial \lambda_{l,l+1}} \times 100$	S_1	S_2	S_3	S_4	S_5
λ_{12}	**9.0**	**10.3**	-3.0	-1.6	-0.9
λ_{23}	-0.9	**9.8**	**10.5**	-2.6	-1.0
λ_{34}	-0.5	-1.8	**11.3**	**12.6**	-1.3
λ_{45}	-0.1	-0.1	-0.5	**14.3**	**14.8**
λ_{56}	0.0	0.4	0.7	0.5	**15.8**

are obtained for homogeneously expanded slabs up to 700 K. From Table 4.2 it can be seen that the dilation of any interlayer separations $d_{n,n+1}$ (or $\lambda_{n,n+1}$) affects mainly the SCLS in the n-th and $(n+1)$-th surface layers while its contribution is only minor for excitations in other layers. Therefore *the*

temperature dependence of individual SCLS provides rather local information on the surface thermal expansion.

4.2.3 Discussion

We are now in a position to use the experimental temperature dependence of the SCLS in combination with Eq. (4.2) to determine the surface expansion. From the measured average slopes of the SCLS temperature dependence, subtracting the contribution due to the homogeneous expansion of the slab and solving the linear system in Eq. (4.2), we obtain the variations of $\lambda_{n,n+1}$, in the temperature range from 300 to 700 K where both experimental and theoretical SCLS variations are safely linear. In this temperature range we got $\Delta\lambda_{12} = 3.2 \pm 0.6\%$, $\Delta\lambda_{23} = -0.9 \pm 0.6\%$ and $\Delta\lambda_{34} = -0.7 \pm 0.8\%$.
As no experimental information is available on the fourth and deeper layer SCLS temperature dependence, we have compared the results in two cases: *i)* homogeneous expansion for these inner layers or *ii)* no temperature variation of their SCLS. Although the computed thermal expansion for the deeper layers are different in the two cases, the results for the three outer layers are not affected. The quoted errorbars reflect the experimental errorbars and assume a 10% relative uncertainty in the theoretical values of the derivatives in Eq. (4.2), accounting for about one third of the final errorbars.
From these results surface-layer dependent coefficients of thermal expansion can be obtained as

$$\alpha_{n,n+1} = (d_{n,n+1})^{-1}(\partial d_{n,n+1}/\partial T) = (\lambda_{n,n+1})^{-1}(\Delta\lambda_{n,n+1}/\Delta T) + \alpha_{bulk}.$$

The final results are 88±15, -10±15 and -6±20 $\times 10^{-6}$ K^{-1}, for α_{12}, α_{23} and α_{34} respectively.
These results are in very good agreement with the LEED experimental determination [105] for the first-to-second layer expansion, where a 70±30 $\times 10^{-6}$ K^{-1} expansion has been reported. According to our present study and at variance with the positive expansion reported in Ref. [105], the second interlayer distance experiences a small but significant thermal contraction. We wish to stress that although the two structural determinations agree within their respective errorbars the present study provides much tighter bounds on the temperature dependence of interlayer separations.
As a final check of our results, the temperature dependent surface state binding energy was recalculated after including the results of the expansion from the core-level study in the surface state theoretical calculations. The total resulting shift of 8.3 meV is again in close agreement with the experimental surface state photoemission determination (7.2 meV), even closer than the result obtained considering the structural data of the LEED experiment (10.0 meV).
A satisfactory theoretical understanding of the large thermal expansion in Be(0001) remains to be reached. A couple of comments may be of interest.

The present study shows that at least two (and maybe more) surface layers show an anomalous behavior, whose interplay could be non trivial. While in the theoretical study of Be(0001) surface thermal expansion of ref. [85] only the relaxation of the topmost layer was considered, more recently the thermal multilayer relaxation of Mg($10\overline{1}0$) has been successfully reproduced [87]. Further, the very large surface electron-phonon coupling in Be(0001) is peculiar of this system and may play a role in determining the surface relaxation at high temperature. This has not been considered in previous studies and deserves further analysis.

4.3 Conclusions

In this chapter we have shown how the temperature affects the SCLS's for two systems, the Rh(100) and the Be(0001) surface.
For the first system, in which the $3d_{5/2}$ SCLS displays just one shifted component related to the top layer atoms, the SCLS decreases on increasing the temperature. The effect was interpreted in terms of a higher anharmonicity of the inter-atomic potential of the surface atoms, in agreement with theoretical predictions.
For the Be(0001) case, we have determined the thermal expansion of the first three interlayer spacings by a novel approach which is based on the coupling of SCLS measurements with first principles calculations. Our results are in good agreement with an earlier LEED study and the anomalous thermal expansion of the first-to-second interlayer spacing on Be(0001) is therefore a well-established fact. Moreover the availability of many components in the Be1s SCLS spectra allowed to determine the surface-layer dependent coefficients of thermal expansion with better accuracy than the LEED experiment: while the first interlayer distance strongly expands upon heating, the distance between the second and third layer slightly contracts. On the other hand, our results do not agree with a highly sophisticated calculation of the first interlayer spacing and this is particularly worrying since the same calculation reproduces the thermal expansion of the bulk correctly. As a possible reason, we suggest that the inclusion of several variable layer spacings in the theory might improve the result.

Chapter 5

Adsorbate induced SCLS

Figure 5.1: Oxygen adsorption on Ru(0001). The Ru atoms of the first layer bound to no, one, two and three oxygen atoms are characterized by different grey scales. The oxygen atoms sit in the hcp adsorption site, with one Ru atom underneath. A detailed explanation of the effect of the oxygen adsorption on the SCLS is given in sect. 5.2.

The subject of SCLS's of clean metal surfaces at low as well as variable temperature was discussed in chapters 3 and 4. It was found that the SCLS's can be resolved for both first and second layer atoms, and that small changes in the geometric structure are reflected in the SCLS's. So far we have not discussed the influence of chemisorbed species on SCLS's.
In the presence of an adsorbate some metal surface atoms change their chemical environment and their coordination and we expect the SCLS's of the neighbouring surface atoms to be modified mostly on those directly bound to the adsorbate. Indeed, if this is so the SCLS's contain considerable information on the chemical state of the adspecies and involved surface atoms.
In order to explore this aspect of SCLS's, which have already been used for elucidation of different bonding configurations in adsorbate systems [13], we have studied the SCLS's induced by oxygen adsorption on Rh(111) and Ru(0001).

Why Oxygen?

The interaction of oxygen with transition metal surfaces is of considerable interest. Apart from its model character for adsorbate-substrate interactions, it is important because of its involvement in catalytic reactions such as CO oxidation, used e.g. for the decontamination of automobile exhaust gases. Moreover, oxygen adsorption on metal surfaces can result in simple adlayer creation, subsurface oxygen penetration, or oxide formation, depending markedly on the oxygen partial pressure, substrate temperature and surface crystallographic orientation of the particular metal. Therefore, significant effort has been made in the last decades to investigate this model process, both from experimental and theoretical points of view.
Oxygen chemisorption on transition metal surfaces is largely discussed in terms of strong covalent bonding between the O $2p$ states and the metal valence d-band, accompanied by an unspecified, but noticeable charge transfer from the substrate to the electronegative adsorbate. However, it is not clear which part of the total electron density could or should be assigned to which atom, so that a clearcut distinction between charge transfer and polarization is not possible [114, 115].
In this context, theoretical concepts have been developed that try to partition a calculated total electron density into contributions from individual atoms [116, 117, 118, 119]. Yet, it would also be useful to have an experimentally accesible quantity, which gives information about the nature of the chemical bond or which would even help to quantify the amount of charge transferred.

As core levels are relatively compact and are generally assumed not to take part in the bonding itself, SCLS's provide such local probe of the changes in the electrostatic potential of a substrate atom in different environments.

5.1 O/Rh(111)

Over recent years, several experimental studies under UHV conditions and low temperatures on the surface crystal structure of low coverage phases of chemisorbed oxygen on Rh(111) have been reported, using primarily low-energy electron diffraction (LEED), scanning tunnel microscopy (STM) and X-ray photelectron diffraction (XPD) [120, 121, 122, 123, 124, 125, 126, 127, 128].
Theoretical work using density-functional theory (DFT) calculations has also been recently reported, which have predicted that an O adlayer with a (1×1) periodicity and coverage $\Theta = 1.0$ ML can form on Rh(111) [129, 130]. Recently, it has been demonstrated that indeed a full monolayer of chemisorbed O can be prepared at room temperature on Rh(111) by using an atomic O beam [131]. Moreover, under particular temperature and pressure conditions the formation of subsurface oxygen species has been

observed, when the 1 ML oxygen adlayer is nearly completed [132].
The *qualitative* difference between a high-coverage oxygen adsorbate phase, namely a high coverage on the surface plus subsurface oxygen, and an oxidized Rh(111) surface is unclear. In this context it is of particular importance to identify and characterize the intrinsic differencies of the O-metal bonding as a function of the chemical environment.
In order to clarify this point, we have studied the oxygen induced Rh3d SCLS for the O/Rh(111) system. We have then compared our experimental results with density functional theory calculations that allow to separate the initial and final state effects and estimate their relative importance. These calculations, which already reproduce with high accuracy the SCLS's of clean surfaces (see sect. 3.1 and 3.3), are found to be equally accurate when dealing with the SCLS's of an adsorbate covered surface.

5.1.1 Experimental

The high-resolution core level photoemission experiments have been performed using a VSW 150 mm 16 parallel channels hemispherical electron energy analyser operated with a pass energy of 5 eV and 20 eV for the Rh3$d_{5/2}$ and O1s core level measurements, respectively. The monochromator energy resolution was varied from 30 to 200 meV, corresponding to a total instrumental resolution in the range of 80-250 meV, depending on photon energy (390 and 650 eV). LEED optics was used to detect the $p(2 \times 2)$ and $p(2 \times 1)$ long-range ordered structures formed upon oxygen adsorption on the surface at room temperature. The ambient background pressure in the chamber was in the range of $8{\times}10^{-11}$ mbar, dominated by hydrogen.
The Rh(111) sample used in the experiments was oriented within 1° and mechanically polished. The following procedure was used for sample cleaning. Initially the surface was cleaned using Ar^+ sputtering at room temperature, annealing at 1300-1350 K, and oxygen treatments at 800-1100 K in order to remove the carbon. Hydrogen reduction at 400-700 K was then used to remove the oxygen. The surface temperature (300 K during measurements) was monitored using two K-type thermocouples spot welded to the sides of the crystal and controlled using a Eurotherm programmable temperature device. We want to point out that the saturation coverage for O_2 exposure below 50 Langmuir is found to be 0.5 ML; (1x1) oxygen structures of 1.0 ML can be obtained on Rh(111) only by dosing NO_2 or atomic oxygen [131]. Rh3$d_{5/2}$ and O1s core level spectra binding energies have been calibrated with respect to the Fermi energy.

5.1.2 Results

In Fig. 5.2 the Rh $3d_{5/2}$ core-level spectra for the clean Rh(111) surface, $p(2 \times 2)$-O/Rh(111) ($\Theta = 0.25$ ML) and $p(2 \times 1)$-O/Rh(111) ($\Theta = 0.5$ML)

ordered structures measured at 300 K, are displayed. The clean spectrum exhibits two well resolved peaks: the lower binding energy peak is attributed to the Rh atoms of the first substrate layer while the higher binding energy component to atoms in the deeper layers, i.e. in the bulk.

In order to evaluate quantitatively the surface core-level shifts, we performed spectral decomposition into bulk and surface components by fitting the data using two peaks with Doniach-Šùnjić (DS) lineshape [16]. The two DS peaks, which were allowed to have different singularity index, α, and Lorentzian width, Γ, were convoluted with Gaussians in order to account for the experimental, phonon and inhomogeneous broadening. We also included a linear background into the fit.

The result of the least-squares analysis is shown in fig. 5.2 as a solid line through the measured points, and the bulk and surface components are also shown. Within the accuracy of the analysis, the SCLS we find for the clean surface, 485±20 meV, as well as the values of the lineshape parameters, reported in the figure caption, are in good agreement with previous experimental findings by Andersen et al. [78]. We decided the number of components to be used in the fits of the spectra at 0.25 and 0.5 ML on the basis of the known structural models [125]. At 0.25 ML, the model proposed for the $p(2\times2)$ structure, displayed in fig.5.2, involves two inequivalent first substrate layer Rh atoms, one not bonded to oxygen adatoms (A) and one directly bonded to a single oxygen adatom (B). Only type-A atoms are present in the clean surface.

The $p(2 \times 1)$ structure is also formed by two different types of surface Rh atoms (see fig. 5.2): the first type is bonded to one oxygen adatom and in a first approximation can be considered as being in a similar chemical environment as atoms B of the $p(2\times2)$ structure; the second type (C) forms two bonds with oxygen adatoms. To each of these three Rh species (A, B, and C) we associated differently shifted core-level components in the fits. This interpretation is corroborated by the theoretical calculations that we used to interpret our experimental findings. Such an assignment, based on the different adsorbate to metal atom coordination numbers has been previously made for the interpretation of measured SCLS's for the CO/Pd(110) [133] and O/Ru($10\bar{1}0$) systems [134].

Best fits were obtained with a SCLS of -485 ± 20, -140 ± 20 and $+295\pm20$ meV for the type-A, B and C Rh atoms, respectively. Note that this classification contains a slight simplification because only the coordination of the Rh atoms considered is taken into account and possible differences in the local geometrical environment due to the presence of oxygen are ignored. However, the theoretical shifts discussed below indicate that the differences introduced by these effects are small compared to those between type-A, B and C atoms. In principle the intensity ratios of the different Rh components should correspond to the relative amounts of Rh atoms bonded to no, one and two O adatoms, respectively, but photoelectron diffraction effects

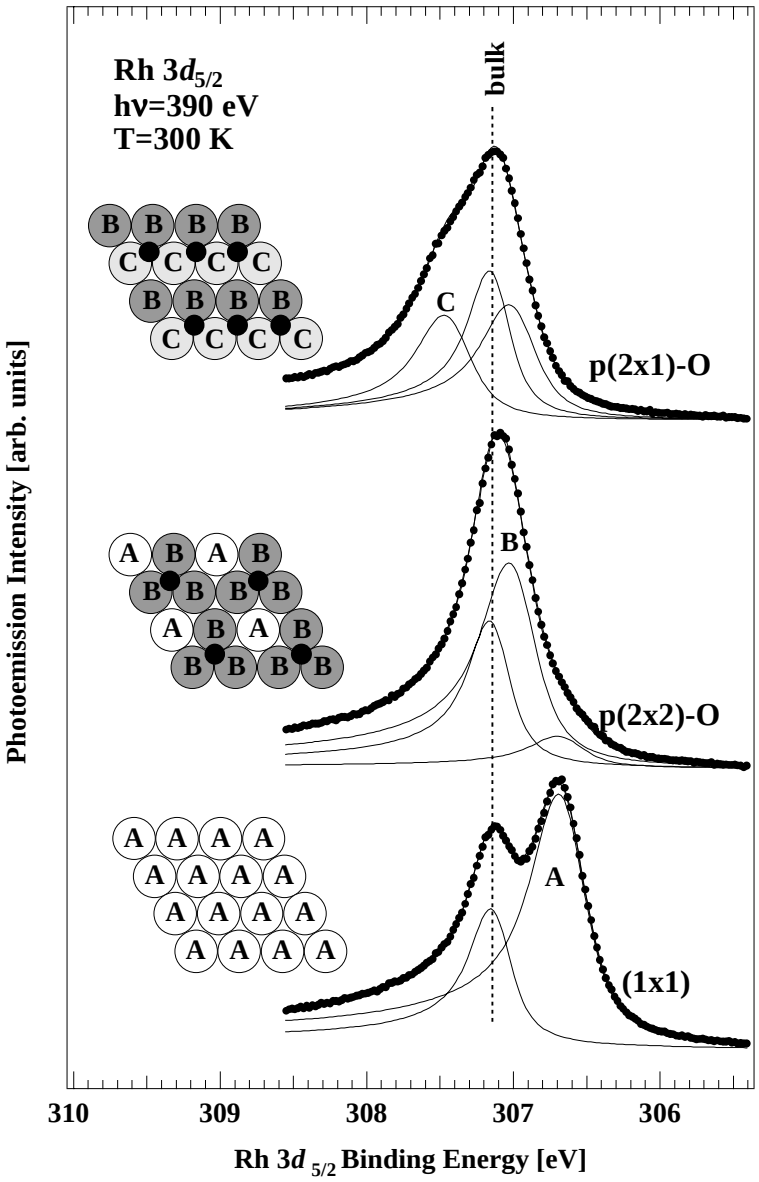

Figure 5.2: Decomposition of Rh $3d_{5/2}$ core-level photoemission spectra of the clean Rh(111) surface and its evolution as a function of oxygen coverage. Dots are experimental data and full lines between dots are the fits. The individual surface and bulk components are also shown. A is the peak associated to Rh surface atoms which are not bound to oxygen. B and C are the peaks associated to Rh atoms coordinated to one and two O adatoms, respectively. Insets: Structural models for the two O-covered structures at 0.25 and 0.5 ML; small black circles, O adatoms. Fitting parameters are $\Gamma = 0.22$ and 0.27 eV, $\alpha = 0.19$ and 0.26, and Gaussian broadening = 0.22 and 0.26 for bulk and surface peaks, respectively.

Table 5.1: Rh 3*d* SCLS's (meV) at the (111) surface as obtained from the transition-state theory and from the initial-state model as a function of the O-coordination or type, given in parentheses (see fig.5.3). The third column shows the difference and gives the screening or final-state contribution to the shifts.

Coverage	O-coordination		Full calc.	Initial-state	Final-state
Clean	0	(A)	−459	−385	−74
0.25	0	(A)	−609	−544	−65
	1	(B)	−85	−75	−10
0.50	1	(B)	−116	−106	−10
	2	(C)	+391	+378	+13
1.00	3	(D)	+939	+801	+138

might in general affect the intensity of the different components.
We have also measured the O 1*s* core-levels corresponding to the 0.25 ML and 0.5 ML oxygen structures. Our data show that the $p(2\times2)$ to $p(2\times1)$ core-level shift is -110 ± 30 meV.

5.1.3 Discussion

Let us now compare the experimental results to the calculated shifts.
The SCLS calculations were performed by M. V. Ganduglia-Pirovano in the Fritz-Haber-Institut, Berlin, Germany, using the theoretical approach adopted to calculate the SCLS's of Ru(0001) (see sect. 3.3). The Rh(111) surface is modeled using a supercell approach, where a seven layer (111) Rh slab with a vacuum region corresponding to six interlayer spacings was used. Oxygen atoms are adsorbed on both sides of the slab. The calculated atomic geometries (interlayer spacings, bond lengths, and lateral displacements) at 0.25 and 0.5 ML are in excellent agreement with the results of previous LEED I-V analyses. The tests of the accuracy of the calculated SCLS's show that the errors induced by the numerical approximations assumed in the theoretical calculations, ($\sim\pm20$ meV), are of the same order as the experimental error.
The results for the Rh 3*d* initial-state SCLS's and from the full calculation for atoms at the Rh(111) surface layer as a function of O coverage (up to 1 ML coverage) are shown in fig. 5.3 and Table 5.1. The final-state contributions to the shifts are displayed in fig. 5.4.
The comparison of our experimental SCLS's, measured up to 0.5 ML coverage, with the theoretical calculations for the Rh 3*d* shifts of the surface layer atoms as a function of O coverage (see fig. 5.3) indicates that there is no doubt that Rh atoms bonding to none, one, or two O atoms, can easily

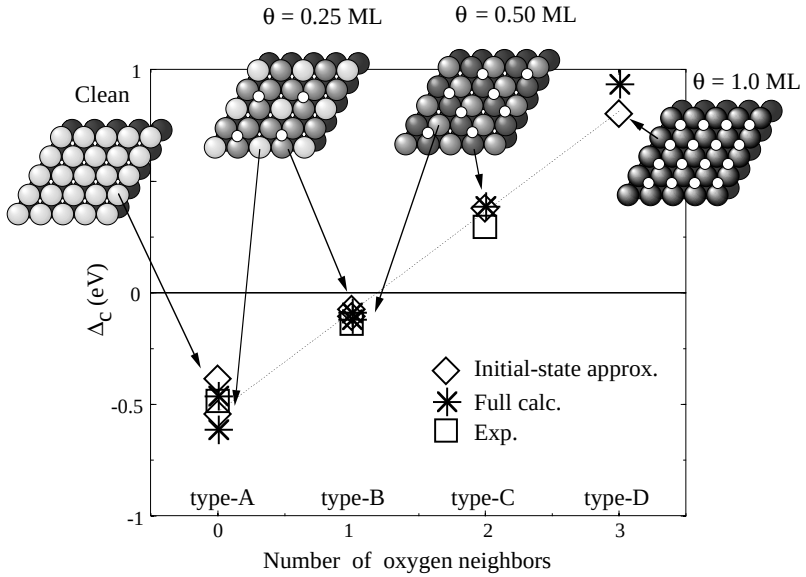

Figure 5.3: Initial-state and full calculation for the Rh 3*d* shifts at the Rh(111) surface as a function of their coordination to O adatoms for the clean and O covered surfaces. Insets: Structural models (small white circles are the O adatoms). Comparison between calculated and measured values is shown for the clean, $p(2\times2)$-O ($\Theta = 0.25$ ML), and $p(2\times1)$-O ($\Theta = 0.50$ ML) phases.

be distinguished by their 3*d* binding energies.
On closer examination, however, there are some quantitative differencies between calculated and measured values of the SCLS's. For the oxygen covered surfaces, the largest difference is ~ 0.10 eV for the type-C atoms, while for type-B atoms it is a factor of two smaller. While this is quite good agreement, we have to say that the small differences between experimental and theoretical results can also be due to the finite temperature of the measurements (T=300K). As shown in sect. 4.1 the SCLS of the clean Rh(100) surface decreases when the surface temperature increases, because of the expansion of the first interlayer distance. Moreover, the fitting procedure strategy is completely independent of the theoretical results and assumes three distinguishable components in order to limit the number of free parameters.
A further confirmation of the assignment of the peaks to the correct Rh atoms comes from the calculation of the initial and final-state contributions to the Rh 3*d* SCLS's for all Rh atoms underneath the surface layer, i.e. of the second substrate layer (see Table 5.2). The experimental positions of the Rh 3*d* levels (relative to bulk) as a function of O coverage up to 0.5 ML and the results of the full transition-state theory calculation for the shifts at the

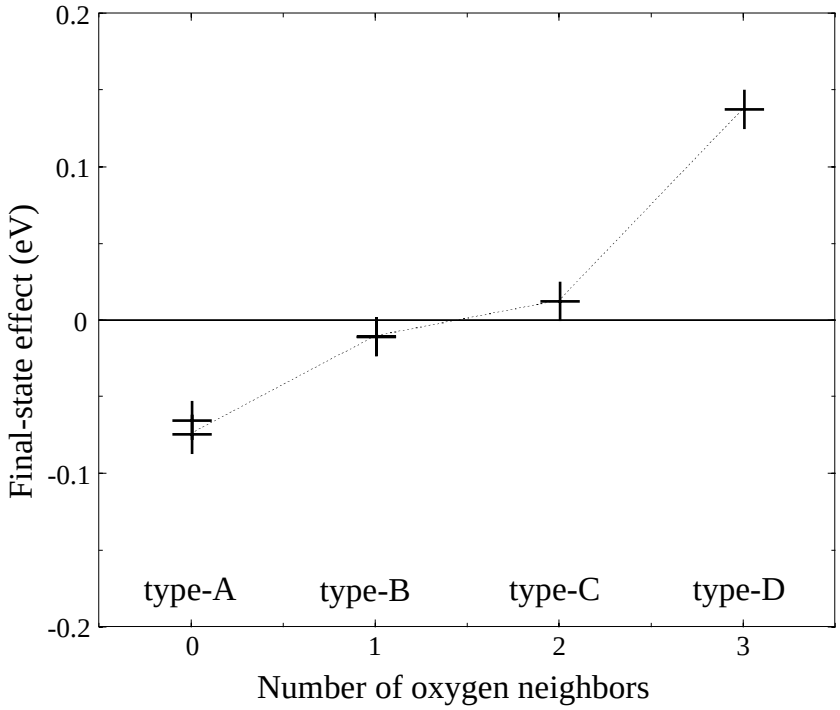

Figure 5.4: Calculated final-state contribution to the Rh 3*d* shifts at the Rh(111) surface as a function of their coordination to O adatoms.

two outermost substrate layers are schematically compared in fig. 5.5. The shift experienced by the 3*d* core-levels of the second substrate layer atoms in the clean Rh(111) surface is one order of magnitude smaller than that of the surface atoms and remained experimentally unresolved.

Table 5.2: The Rh 3*d* surface core-level shifts (meV) of second substrate layer atoms of the clean and O-covered Rh(111) surfaces within the transition-state theory and from the initial-state model as a function of coverage. The third column shows the difference and gives the screening contribution to the shifts. For the 0.25 and 0.50 ML phases, from the two inequivalent second layer atoms, only the value which is non-negligible is listed (see text).

Coverage	Full calc.	Initial-state	Final-state
Clean	+67	+96	−29
0.25	−150	−164	+14
0.50	−155	−173	+18
1.00	−217	−216	~ 0

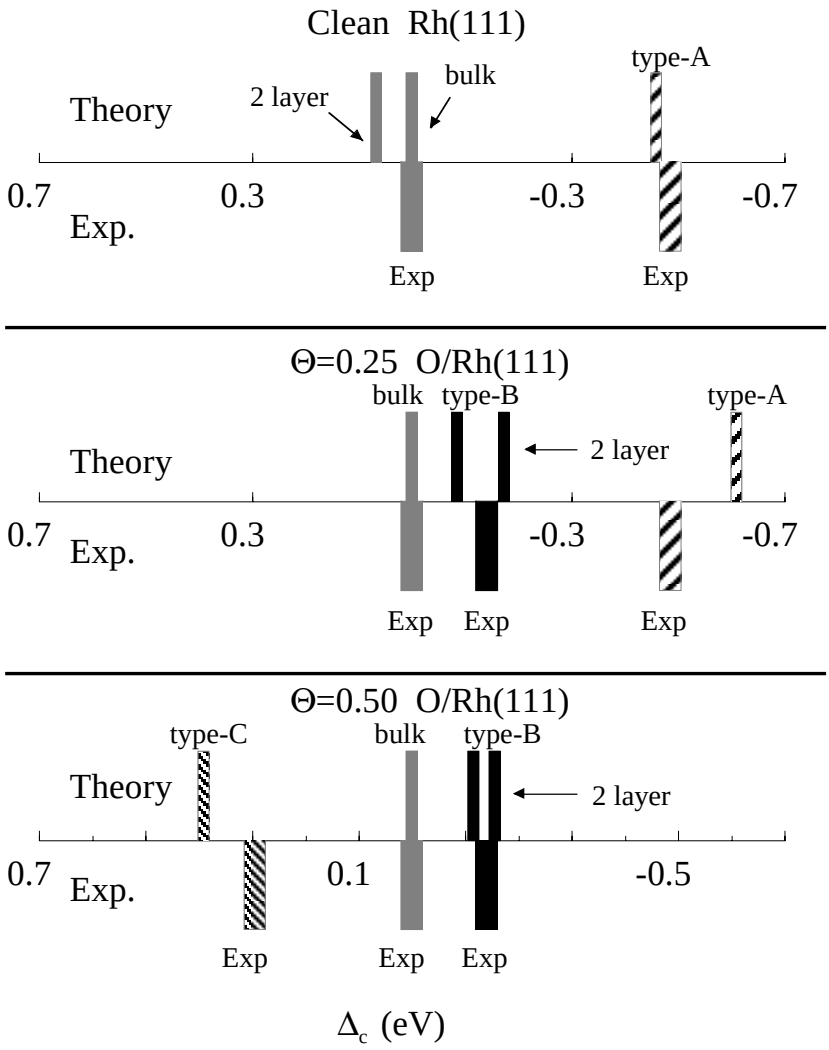

Figure 5.5: The experimental positions of the Rh 3*d* surface levels relative to the bulk ones, for the clean and O-covered surfaces (Exp.), and the full transition-state theory calculation for the shifts at the surface and the layer beneath (Theory). For the second substrate layer atoms, only the shifts which are different from zero are shown (see text). The different patterns in the lower panels indicate the different experimentally resolved positions as a function of coverage. In the upper panels, the labels indicate from which atoms the shifts originate and the lines which remained experimentally unresolved have the same pattern.

For the O-covered surfaces, there are two inequivalent Rh second layer atoms at both 0.25 and 0.50 ML coverages, respectively. The calculations indicate that for each coverage only one kind has a sizeable shift and the other co-

incides with the bulk peak. The corresponding non-negligible full shifts are -150 meV (0.25 ML) and -155 meV (0.50 ML). Although the magnitude of these shifts is sizeable, they remain experimentally unresolved as they are superimposed to the measured type-B atoms surface peak.
The calculated full shifts at the second substrate layer atoms of the $p(2 \times 2)$ and $p(2 \times 1)$ structures differ by only 65 and 39 meV from those of the type-B Rh surface atoms at the same coverage, respectively (see Table 5.1). The most notable result of fig. 5.5 is that our experimental spectra resolve the main features of the oxygen induced shifts and the agreement between experimental and theoretical data is not only qualitatively very good but also quantitatively satisfactory.

Initial-state effects

We can now discuss the initial and final state contributions to the SCLS's upon oxygen adsorption. For the clean Rh(111) surface, the calculated SCLS is -459 meV, thus in good agreement with the experimental value of -485 ± 20 meV. The screening contribution to this value is -74 meV. These values are in line with earlier measurements and DFT-LDA results [30, 78]. The fact that the initial-state SCLS is negative for Rh surfaces is qualitatively well understood in terms of the narrowing of the $4d$-band.
The results presented in fig. 5.3 and Table 5.1 clearly demonstrate that there is a strong oxygen coverage dependence of the initial-state contribution to the SCLS's. The lowest energy structures at all coverages are phases with O adatoms at the fcc hollow sites [130]. On the basis of the calculations, the difference in Rh $3d$ shifts of the clean Rh(111) surface and the type-A atoms of the $p(2 \times 2)$-O/Rh(111) phase is ~ 150 meV. Differences in the screening of the core hole are negligible. LEED analyses and DFT-GGA calculations have shown that oxygen adsorption induces buckling and a substantial overall expansion of the first interlayer spacing [125, 130]. The reason for the calculated 150 meV difference is thus related to changes in the crystal structure. However, this difference is small compared to that between type-A and type-B atoms.
The initial-state contribution to the SCLS's of type-B Rh sites of the $p(2 \times 2)$ structure is -75 meV, i.e. their $3d$ levels are bound more strongly by 310 meV relative to those of the clean surface atoms (see Table 5.1).
The higher, 0.50 ML coverage, $p(2 \times 1)$ structure contains type-B and type-C Rh atoms (see fig. 5.3). The initial-state SCLS's are -106 meV and $+378$ meV, respectively. The shift for the type-B atoms differs by 31 meV from that in the 0.25 ML phase. The small difference reflects again that the atoms are similar but not identical due to the slightly modified local geometry. However, larger shifts towards higher binding energies are obtained for type-C atoms, which are completely absent in the 0.25 ML phase.

At the highest coverage of 1.0 ML there is only one kind of Rh sites (type-D), namely Rh atoms coordinated to three O adatoms. The core levels are shifted to even larger binding energies.
The initial-state results given in fig. 5.3 show a quasilinear correlation of the shifts and the number of the coordinated O atoms. This initial-state trend is expected from the chemisorption of electronegative species on metal surfaces. Because electron withdrawing, O adatoms reduce electron-electron repulsion in the core of their Rh nearest neighbors and the potential at the surface changes relative to the bulk. This surface potential shift (SPS) acts on the surface d-band as well as on the core electrons and is more attractive with increasing coverage.
In fig. 5.6 the spherically symmetric part of the surface potential shift $\Delta V(r) = V^{\rm surf}(r) - V^{\rm bulk}(r)$ together with $r^2|R_{3d}(r)|^2$ and $r^2|R_{4d}(r)|^2$, is shown. We see that $\Delta V(r)$ is almost constant in the region sampled by the

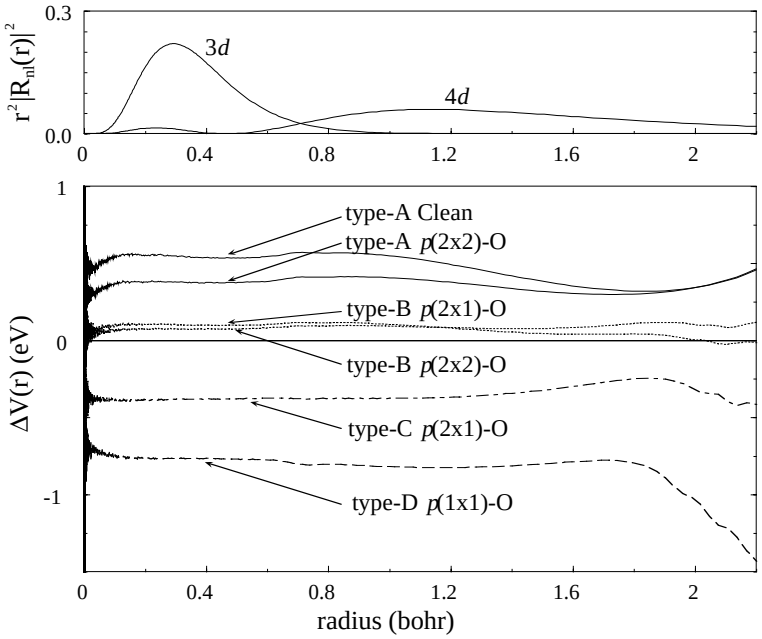

Figure 5.6: Surface potential shift SPS, $\Delta V(r)$, for all surface Rh atoms at the coverages considered. Type-A atoms are not bound to oxygen. B, C and D are Rh atoms coordinated to one, two or three O adatoms, respectively. Radial solutions $r^2\,|R_{nl}(r)|^2$, $nl = 3d$ and $4d$ within the muffin-tin sphere of 2.2 bohr in the bulk.

$3d$ core electrons. For this reason, the numerical values of the initial state SCLS's are nearly equal to $-4\pi \int \Delta V(r) r^2 |R_{3d}(r)|^2 dr$. The potential shift is repulsive for those surface atoms which are not bound to O (type-A). Adsorption of oxygen induces large changes in the SPS; increasing the O coverage leads to more attractive potentials at the surface. The behavior

of the potential shifts and the initial-state trend as coverage increases correlate with the calculated increase of the work function as a function of O coverage, which reflects an oxygen induced inward dipole moment, i.e. with the negative charge at the vacuum side of the surface [130]. Thus, the gross behavior of the initial-state shifts can be taken as a fingerprint of the electronegativity of oxygen. The Rh $3d$ binding energy increases by about 0.3 eV per oxygen bond.
Figure 5.7 displays the density of states per atom projected onto the d orbitals (d-DOS), $n_d(\epsilon)$, for all surface and bulk atoms. For the clean surface

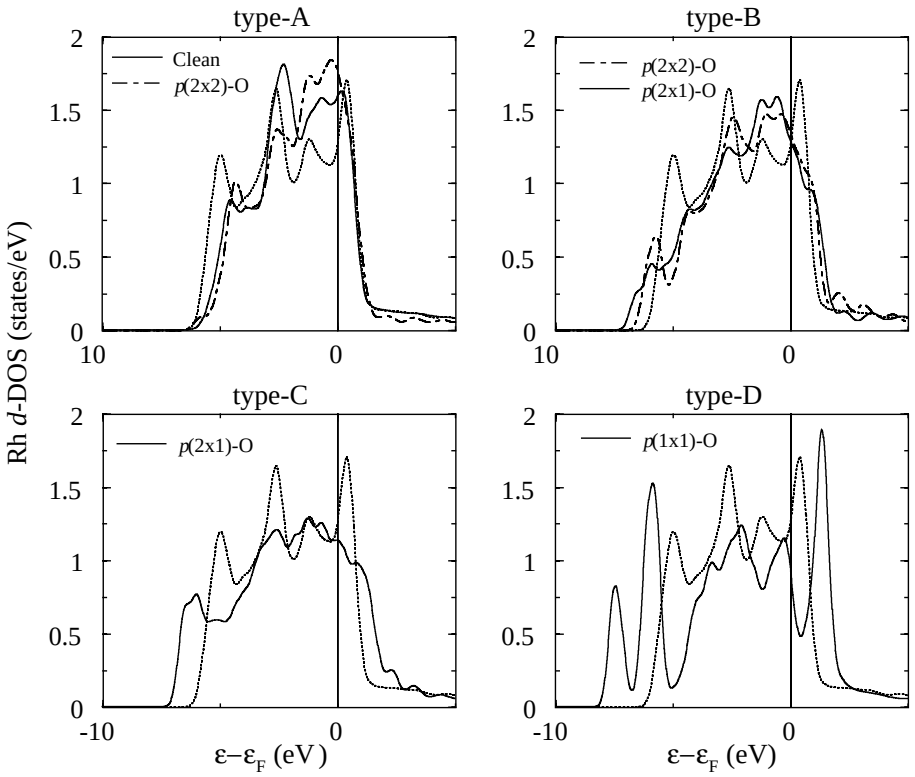

Figure 5.7: Projected density of states per Rh atom onto the $4d$ orbitals for all surface atoms at the coverages considered (initial-state calculations). Type-A atoms are not bound to oxygen B, C and D are Rh atoms coordinated to one, two or three O adatoms, respectively. The dotted lines correspond to Rh bulk.

and type-A atoms of the $p(2 \times 2)$-O structure a narrower and displaced (towards lower binding energy) d-DOS is clearly visible. In comparison with the type-A surface atoms, the d-DOS for type-B, C, and D atoms is broader (relative to the bulk). The calculated shift in the center of gravity $\Delta C_d = -[\epsilon_d^{\rm surf} - \epsilon_d^{\rm bulk}]$ of the d DOS and the initial-state shifts are shown in fig. 5.8. These results show that the initial-state SCLS's and the shift

in the center of gravity of the d DOS follow the same trend but they are not equal. The reason of this is that the $4d$ orbitals are quite broad and

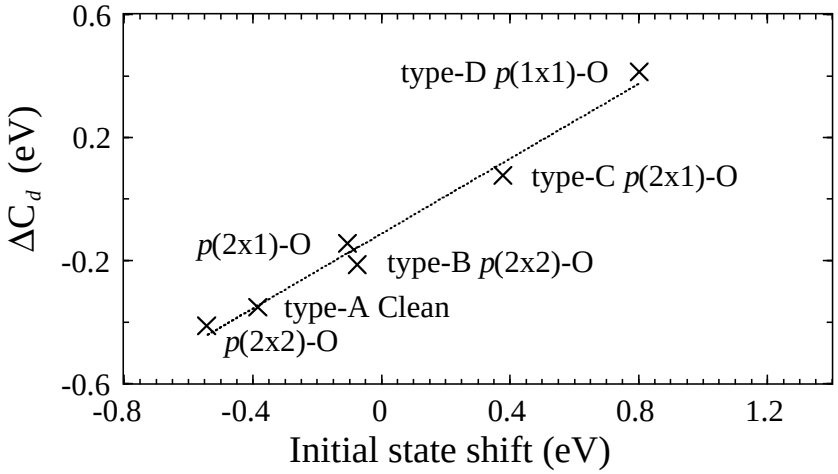

Figure 5.8: Calculated shift of the d-band center between the self-consistent bulk and surface d bands and the initial-state core-level shifts.

sample a potential shift little different from that sampled by the $3d$ orbitals (see fig. 5.6). The qualitative correlation between ΔC_d's and initial-state shifts reflects that the shift of the d-band and the SCLS's arise from the same oxygen induced surface potential shifts as experienced by the d states and core states, respectively.

Final-state effects

The final-state contributions to the SCLS's are shown in fig. 5.4. The magnitude of the screening contribution is small compared to that of the initial-state shift. This, however, does not mean that this term can be neglected since its magnitude amounts in some cases up to $\sim 15\%$ of the full shift, and in general tends to improve the agreement to the measured SCLS's (see Table 5.1). We note, however, that the *sign* of the initial-state and that of the full transition-state theory SCLS's is always the same; in general, even this does not hold necessarily [135]. Thus final-state effects, while not insignificant, do not appear to be the dominant factor responsible for the Rh $3d$ SCLS's considered.
Looking into more detail at this contribution it is seen that it changes sign as the oxygen coverage increases (see fig. 5.4). The sign change of the final-state contributions to the shifts can be qualitatively explained by tracing it back to the oxygen induced changes to the $4d$ band. Comparing the projected densities of states per Rh atom onto the $4d$ orbitals for a bulk and surface atom at the clean Rh(111) surface, one observes the higher density

of high-lying localized d-states about the Fermi level (see fig. 5.7). For the adlayer systems, however, the screening at the surface becomes worse upon increasing O coverage. In fact, at a coverage of 1.0 ML it is positive and largest in magnitude (see fig. 5.4). The screening of a Rh $3d$ core-hole created at high oxygen covered surfaces is less efficient because of the oxygen induced decrease of d-states around the Fermi level localized at the respective atom (see fig. 5.7).

O 1s core level shift

Together with SCLS's we have also measured the O $1s$ core level for the $p(2 \times 2)$-O and $p(2 \times 1)$-O structures. This peak should significantly shift if the adsorption site changes at increasing coverage [4, 5]. In contrast to the Rh $3d$ shifts, the O $1s$ spectra show only minor changes, i.e. a shift of -110 ± 30 meV. Also in this case theoretical calculations have been performed which predict a full shift of -34 meV (initial-state -10 meV) between the $p(2 \times 2)$-O and $p(2 \times 1)$-O structures, with the oxygen always sitting in the same fcc adsorption site. Moreover, the calculation of the O $1s$ binding energy shift between the fcc and the hcp sites at a coverage of 0.25 ML gives 0.36 eV, with the binding energy for fcc sites shifted towards lower values.
From the comparison of our experimental result with that of the calculations we conclude that the adsorption site remains the same at increasing coverage. In this case this is the only information that can be extracted from the measurement of the adsorbate core level.

5.2 O/Ru(0001)

In the previous section we have shown how the SCLS's of the Rh(111) surface change upon oxygen adsorption. In particular we have found satisfactory agreement between the experimantal results and first principle calculations for the $p(2 \times 2)$ and $p(2 \times 1)$ oxygen ordered adlayers.
In the present section we investigate the O interaction with the Ru(0001) surface by measuring again the SCLS's, with the aim to compare the chemisorption behaviour of the two surfaces. Further, on Ru(0001) four different ordered O adlayer structures are formed, which span the coverage range from zero up to one monolayer (ML) and are all extensively characterized by LEED experiments [82, 83, 136, 137] and DFT calculations [138]. Hence, a much larger experimental data base is available compared to the O/Rh(111) work, which allows to assess much better the agreement between measured and calculated SCLS's.
The four ordered oxygen overlayers, which we have prepared and studied besides the clean surface, already presented in sect. 3.3, are the $p(2 \times 2)$

[82], the $p(2\times1)$ [83], the (2×2)-3O [136] and the (1×1)-O [137] structure. In all phases, the O atoms sit in hcp hollow sites and the Ru atoms can have up to three O neighbours as shown in fig. 5.9. As will be shown in the following, the Ru $3d_{5/2}$ core level spectra are composed of several peaks, which have to be assigned to certain bonding situations of the corresponding Ru atoms. From the aforementioned work on O/Rh(111) of section 5.1, we expect the SCLS's of the first layer atoms to depend primarily on the number of directly coordinated O atoms. The nomenclature that we use to name each of these atoms (and their corresponding SCLS) is derived from this fact and is described in fig. 5.9.
If the number of nearest neighbour O atoms is indeed the ruling quantity for the first layer peaks, the assignment of the O-induced components in the spectra is straightforward, because each such peak should be present in two of the considered phases. As shown in fig. 5.10, O-induced components at approximately equal positions appear indeed each time at two coverages, so that recurrently working down from the (1×1)-O, the S_1(3O), S_1(2O), and S_1(1O) peaks can directly be assigned.
As far as it concerns the assignment of the S_1 and S_2 peaks which are both present in the spectrum of the clean surface and of the $p(2\times2)$ phase, it has been achieved on experimental grounds using photoelectron diffraction, as shown in section 3.3.
Once the measurement and the assignment of the various SCLS components has been accomplished, they can be compared with the theoretical results. As the latter allow to separate the final state contribution from the total shift, we are then in a position to discuss the connection of the initial state shift with the nature of the chemical bond.

5.2.1 Experimental

The procedure used for cleaning the Ru(0001) crystal was the same as that described in section 3.3.1.
The SCLS spectra were acquired at a sample temperature lower than 130 K and at a base pressure of 6×10^{-11} mbar, using the double pass electron energy analyser (see sect. 2.2). All data shown for the series of SCLS's as a function of oxygen coverage were measured in one single run for maximum comparability, but were in good agreement with a partial data set obtained earlier using a VSW 150 mm electron energy analyser with 16 channels parallel detection [139].
Before doing the SCLS measurements, the different oxygen structures were defined by observing the intensity of the $(\frac{1}{2},\frac{1}{2})$ spot in the LEED pattern induced by the oxygen adsorption. The fully developed three structures up to 0.75 ML show maxima in the intensity of the extra spots while dosing oxygen when the layer corresponds to 0.25, 0.50 and 0.75 ML coverage. Since the LEED apparatus is mounted in the experimental chamber we could in

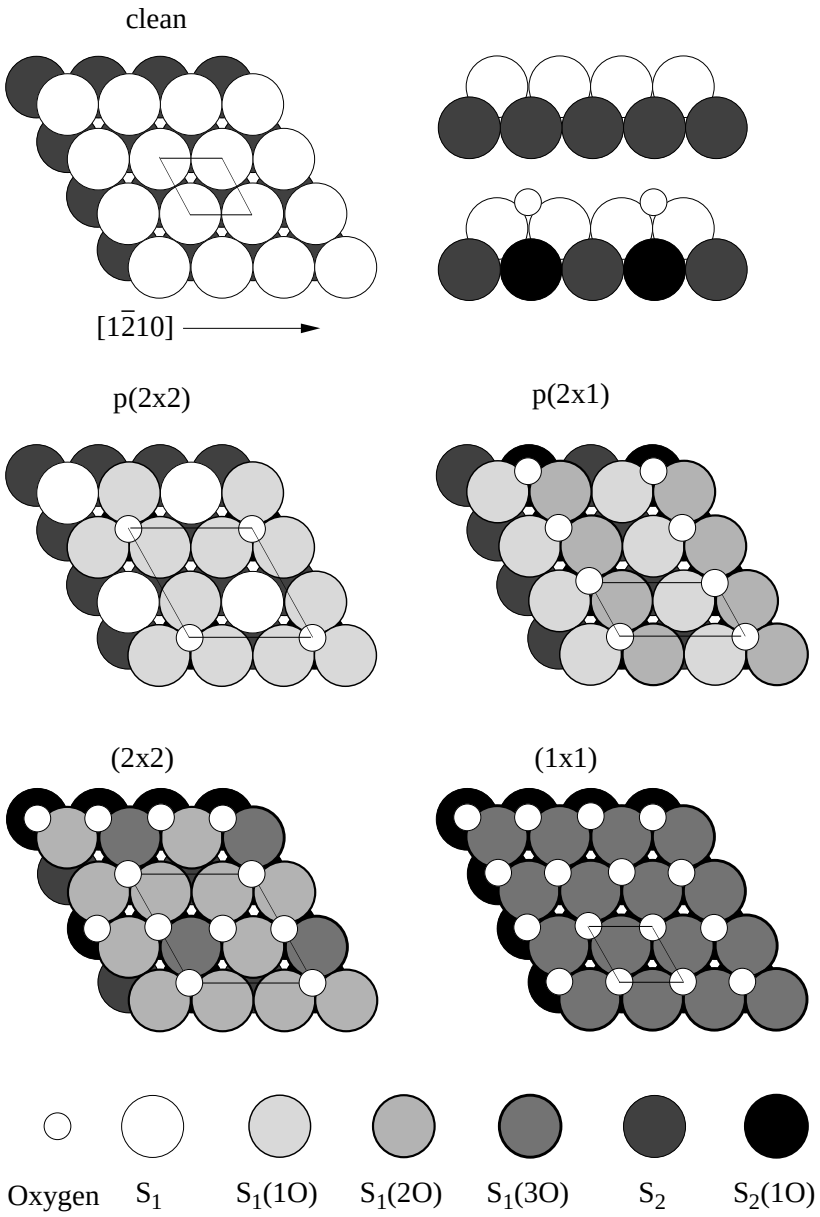

Figure 5.9: Periodic oxygen adlayer structures on the Ru(0001) surface with increasing coverage. S_1, S_1(1O), S_1(2O) and S_1(3O) are first layer Ru atoms bound to no, one, two, and three oxygen atoms, respectively. S_2 and S_2(1O) are second layer atoms with no and one oxygen atom directly above on the surface, respectively. The bulk b includes all deeper layer Ru atoms. The top right panel shows side views of the clean Ru(0001) surface as well as of the $p(2 \times 1)$ structure.

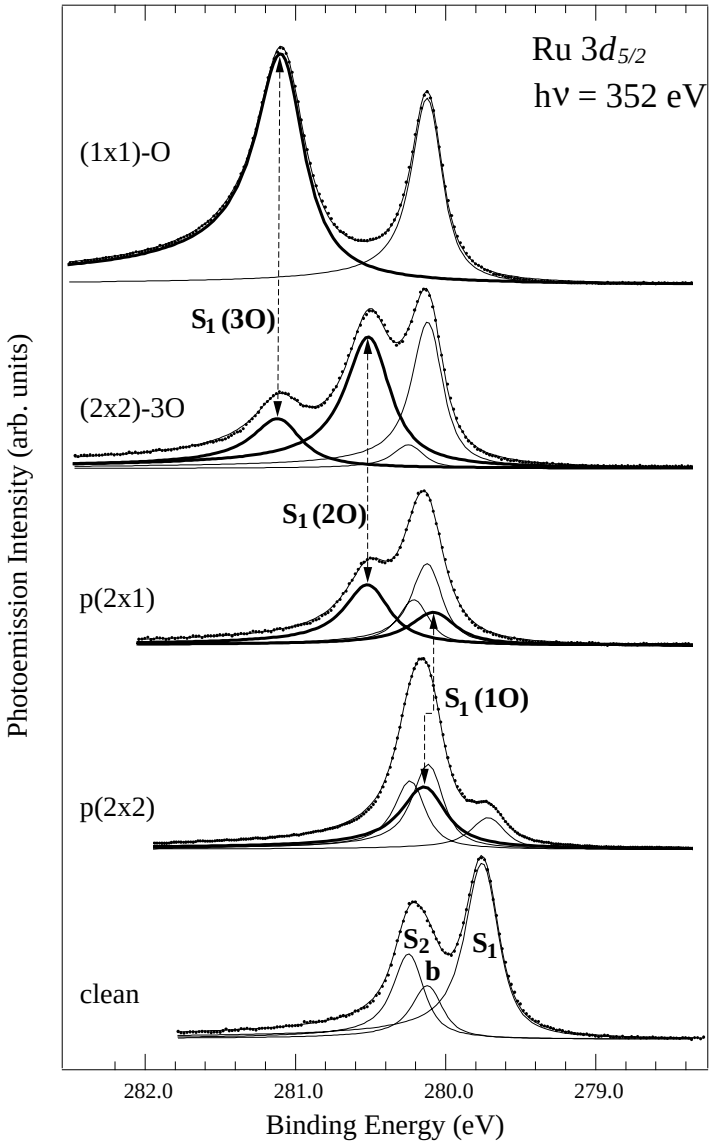

Figure 5.10: Ru $3d_{5/2}$ core level spectra for the clean surface and the four oxygen structures. The dots represent the experimental results, while the line in between is the result of the fit. The spectra were measured at a temperature lower than 130 K. The components used in the fit are added in the figure. The curves with the thin line denote the "clean" components (S_1, S_2), while the thicker lines are the oxygen related components, S_1(1O), S_1(2O), and S_1(3O), corresponding to first layer Ru atoms bonded to one, two and three oxygen atoms respectively (cf. fig. 5.9). The dashed lines with arrows denote the presence of each of these components in two different structures.

this way monitor the correct dose of oxygen in order to obtain the desired structure. The coverage was also checked by measuring the O_{1s} intensity. Comparison of the LEED to the XPS data shows that the O_{1s} signal measured at 650 eV photon energy is not much affected by diffraction effects; it therefore gives a good estimate of the relative coverage.
The $p(2\times2)$ structure was obtained by exposing the clean Ru(0001) surface to 0.7 Langmuir (nominal) of oxygen at 373 K, and subsequent brief heating to 670 K. The $p(2\times1)$ structure was obtained by dosing onto the $p(2\times2)$ additional 3.5 Langmuir at 373 K, followed again by brief heating to 670 K. As reported in the previous works, flashing at 670 K after the doses is needed to achieve perfect order of the superstructure. The (2×2)-3O structure was obtained by dosing oxygen for 600 seconds with the channel plate doser at a distance of $\sim$ 10 mm from the sample, with a pressure in the chamber of 1.5×10^{-6} mbar at a sample temperature of 600 K. The resulting O_{1s} intensity corresponded to 0.85 ML. In order to remove the excess oxygen the sample was briefly heated to 1060 K; the resulting coverage was 0.77 ML. The (1×1)-O structure was obtained by dosing NO_2 3 times, 800 seconds each, with the doser (pressure in the chamber 5×10^{-8} mbar), at a sample temperature of 600 K. A very sharp (1×1) LEED pattern resulted.
The high resolution Ru $3d_{5/2}$ SCLS spectra were recorded at a photon beam incidence angle of 80° from the surface normal which results in an electron emission angle of 40°. Three different photon energies, 352, 370 and 400 eV were used in order to change the weight of the core level components due to diffraction and inelastic scattering effects. The $p(2\times2)$ structure was measured only at 352 eV. The analyser was operated at 5 eV pass energy with an entrance slit of 2 mm. The overall energy resolution is estimated to have been better than 80 meV.

5.2.2 Results

A. SCLS analysis

In fig. 5.10 the SCLS spectra measured at 352 eV are shown, together with the fits and the various components. We fitted the data using Doniach-Sunjic functions convoluted with Gaussian broadening [16]. The background was assumed to be linear. In order to get physically meaningful results from the fits it was necessary to put constraints on some parameters of the fitting function as many components have significant overlap. The three spectra at different photon energy of a certain structure (except for the $p(2\times2)$) were hence fitted together with identical parameters, leaving free only the intensities of the core level components. In this way the line shape parameters found (Gaussian and Lorentzian width, as well as the asymmetry parameter) are more reliable. We employed two strategies to assign the

various peaks to the differently coordinated Ru atoms in the surface.

strategy (i)

This is an independent experimental assignment, which uses only the structural knowledge of the various O phases as described above.

The fitting procedure adopted assumes the $S_2(1O)$ component to be indistinguishable from the bulk in all the fits. This assumption rests on the spectrum for the (1×1)-O phase, where the bulk and $S_1(3O)$ are far from each other and the clear-cut two peak spectrum with small overlap in between does not justify a third component hidden under either peak at first glance, cf. fig. 5.10.
The approach used to fit the data was the following:

1) First the (1×1)-O structure was fitted, for which only two components were assumed to be present which must be bulk and the $S_1(3O)$. In this way we found the line shape parameters of the bulk (L = 0.175, α = 0.085, G = 0.11) and the $S_1(3O)$ (L = 0.31, α = 0.150, G = 0.11) peaks.

2) Then we fitted the clean surface. In this case three components are present: S_1, S_2 and bulk. We kept the asymmetry parameter and the Lorentzian width for all components at the values found previously for the bulk in the (1×1)-O, and we let free the Gaussian width of the S_2 and S_1. The Gaussian width of S_2 turns out to be 0.11 eV, the same as for the bulk, while that of S_1 is 0.13 eV. The assignment to first and second layer atoms, shown in fig. 5.10, has been corroborated by independent SCLS-photoelectron diffraction experiments as described in section 3.3.

3) Next we fitted the spectra at 352 eV of the $p(2 \times 2)$ in order to determine the parameters of the $S_1(1O)$ peak (L = 0.30, α = 0.085, G = 0.11). These parameters are not as accurate because of the strong overlap of this peak with that of the bulk and the other peaks present.

4) Then we fitted the $p(2 \times 1)$ spectrum in order to determine the parameters of the $S_1(2O)$ component (L = 0.30, α = 0.085, G = 0.11). The parameters for this peak are not as accurate as for the $S_1(3O)$, but are definitely more accurate than those of the $S_1(1O)$.

5) Finally we fitted the $(2 \times 1)3O$ using the line shape parameters found previously for the various components.

strategy (ii)

This relies partially on information from the theoretical calculations, the main difference being the inclusion of (small) non-zero shifts of the $S_2(1O)$ peak, which was neglected in strategy (i) to avoid overfitting. As will be shown in the following, approach (ii) improves the quantitative agreement between theory and experiment, yet we argue that approach (i) was also important in order to assure that both, measurement and calculation, lead

independently to the same conclusions.
The approach used to fit the data was the following:

1) The clean surface was fitted first. In the fit we kept the Lorentzian width the same for the three components, letting free the asymmetry and the Gaussian width. Fitted this way, the Lorentzian width is 0.18, the asymmetry turns out to be the same for all components, 0.086, and the Gaussian width of the S_1, S_2 and bulk peak is 0.13, 0.09, and 0.08 respectively. The quality of the fit was slightly better than that of the fit of the clean surface using the first strategy, while the derived SCLS's were almost the same: $S_1 = -360$ meV and $S_2 = +127$ meV.

2) Then we tried to fit the (1×1)-O structure fixing for the bulk peak the same line shape parameters found for the clean surface and assuming that only two components, bulk and $S_1(3O)$, are present. In line with the theoretical prediction, the bad quality of the fit rendered it necessary to fix a third non-zero component, $S_2(1O)$, at slightly lower binding energy than the bulk peak. We fixed for this new peak the same line shape parameters as for the bulk. By fitting the (1×1)-O structure with these three peaks instead of two, the parameters of the $S_1(3O)$ do not change with respect to the first fitting strategy. The bulk and the $S_2(1O)$ components show similar intensities. The SCLS for $S_1(3O)$ and $S_2(1O)$ turn out at 920 meV and -60 meV respectively, both now in excellent agreement with the theoretical values.

3) Similarly, we tried to add a non-zero $S_2(1O)$ peak close to the bulk region for all other structures, but the results were meaningless since too many peaks are present in a small energy range.
The SCLS values, obtained adopting the two strategies (i) and (ii) are collected in Table 5.3. The error bars shown in the table were estimated from the quality of the fits when changing the SCLS in this energy range. Therefore, possible errors related to the oxygen coverage are not included in the table.

B. Comparison with theory

Let's see now how the experimental SCLS's values compare with the theoretical calculations. As for the clean Ru(0001) surface, the density functional theory calculations of the SCLS's were performed by K. Reuter in the Fritz-Haber-Institut, Berlin, Germany, employing the same computational code. The Ru(0001) surface is modeled using a six layer slab, and O is adsorbed on both sides to preserve mirror symmetry. A vacuum region corresponding to five Ru interlayer spacings ($\approx$11Å) was employed to decouple the surfaces of consecutive slabs in the supercell approach. Within a (2×2) surface unit cell, the positions of all O adatoms and Ru atoms in the outer two substrate layers were fully relaxed for all coverages considered. The resulting adsorption geometries are in very good agreement with existing LEED data

Table 5.3: Measured SCLSs of the Ru $3d_{5/2}$ level at all coverages in meV. Positive shifts reflect a more strongly bound core level at the surface compared to the bulk. The nomenclature for the different substrate atoms (S_1, S_2 etc.) follows that of fig. 5.9. In strategy (i) the value of the S_2(1O) was set to 0 for all the structures, while only for the (1×1)-O its value was obtained by fitting strategy (ii).

	strategy (i)	strategy (ii)
clean, S_1	-366 ± 10	-360 ± 10
clean, S_2	$+125 \pm 10$	$+127 \pm 10$
$p(2 \times 2)$, S_1	-400 ± 20	
$p(2 \times 2)$, S_1(1O)	$+20 \pm 30$	
$p(2 \times 2)$, S_2	$+120 \pm 30$	
$p(2 \times 1)$, S_1(1O)	-50 ± 30	
$p(2 \times 1)$, S_1(2O)	$+390 \pm 10$	
$p(2 \times 1)$, S_2	$+88 \pm 30$	
(2×2)-3O, S_1(2O)	$+387 \pm 20$	
(2×2)-3O, S_1(3O)	$+980 \pm 10$	
(2×2)-3O, S_2	$+127 \pm 30$	
(1×1)-O, S_1(3O)	$+960 \pm 10$	$+920 \pm 10$
(1×1)-O, S_2(1O)	0	-60 ± 10

[82, 83, 136, 137], as well as with earlier DFT pseudo-potential calculations [138].

The initial state and full SCLS's are given by eqs. 1.82 and 1.84, respectively. (2×2) supercells were used to surround each ionized atom (with half an electron missing) with neighbours possessing the normal core configuration and kept the fully relaxed ground state geometry fixed. Overall charge neutrality was imposed, i.e. half an electron was added at the Fermi level. Initial state and full calculations for the $3d$ SCLS's were done for each inequivalent Ru atom in the outermost two substrate layers at all experimentally described coverages. The bulk core level position, ϵ_c^{bulk}, was calculated using a ten layer bulk slab inside the same supercell as used for the surface calculations. The numerical accuracy of the calculations is estimated to be ± 30 meV, which is of the same order as the experimental error.

The SCLS's were calculated for both (1×1) phases using also the local density approximation (LDA) for the exchange-correlation functional [140]. The S_1 and S_2 of the clean surface, as well as the S_2(1O) of the (1×1)-O phase are found to lie within ± 10 meV of the values obtained with the GGA. On the other hand, the SCLS of the threefold O coordinated first layer

atom S_1(3O) changed by 101 meV, significantly worsening the agreement with the experimental value. This finding is related to an improved description within the GGA, which – as deduced from the remarkable agreement between experiment and theory reported below – seems to allow a highly accurate determination of the quantity of interest to our study.

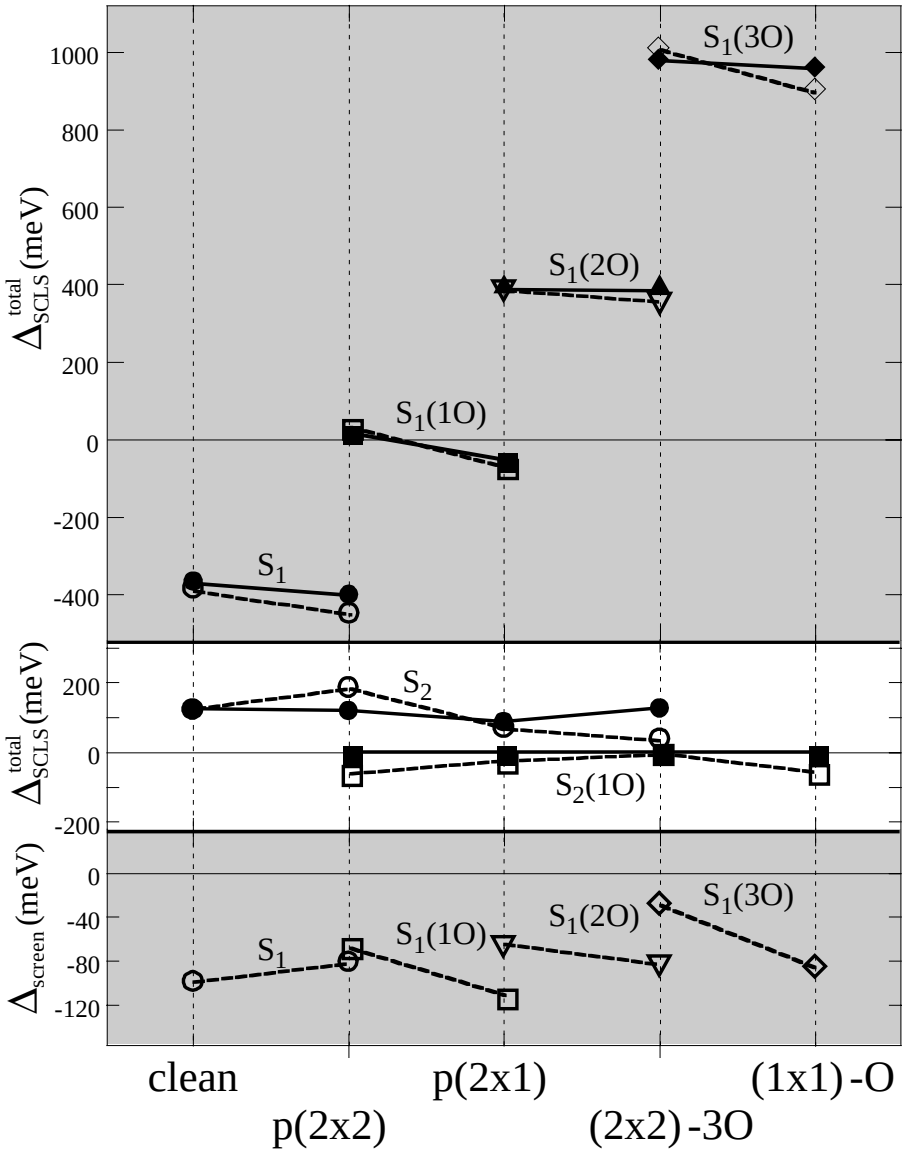

Figure 5.11: Comparison of the calculated SCLS's (open symbols) with the experimental results (filled symbols) obtained by fitting strategy (i). The top panel represents the SCLS's of the first substrate layer Ru atoms, while the middle panel displays the SCLS's of the second layer ones. The bottom panel displays the screening contribution to the total first layer shifts.

Figure 5.11 shows a comparison between the calculated and the measured SCLS's. It is immediately obvious that almost all theoretical and experimental shifts fall within their mutually assigned error bars, reflecting the consistency between both data sets we aim at. While still showing a good semi-quantitative agreement, only the following shifts do not meet this requirement: S_2 and S_2(1O) in the $p(2\times 2)$, S_2 in the (2×2)-3O, as well as S_1(3O) and S_2(1O) in the (1×1)-O. The disagreement in the S_2(1O) shifts is not surprising, as this component was neglected in the original experimental data analysis (strategy (i)) in order to avoid overfitting. After the theoretical calculations had predicted non-vanishing S_2(1O) shifts particularly for the $p(2\times 2)$ and the (1×1)-O phases, we reanalyzed the experimental data set including this component (strategy (ii)). This was unambiguously possible in the case of the (1×1)-O phase with its clearly separate bulk and surface peaks. The resulting value of $S_2(1\mathrm{O}) = -60 \pm 10$meV agrees perfectly with the theoretical $S_2(1\mathrm{O}) = -53 \pm 30$meV, bringing now also the calculated and measured S_1(3O) peak into consistency (theory: $+899 \pm 30$meV, exp: 920 ± 10meV). Unfortunately, the crowding of peaks around the bulk peak in the $p(2\times 2)$ phase did not allow to add yet another component to the fitting procedure. Hence, we were not able to resolve the small discrepancy for the S_2(1O) peak in this phase.
This leaves only the S_2 components in the $p(2\times 2)$ and in the (2×2)-3O. As just discussed, the experimentally derived value for the $p(2\times 2)$ could be affected by neglecting the S_2(1O) peak in the fitting procedure. Additionally, we measured this structure only at 352 eV, and furthermore probably the error bar of the measured SCLS is bigger due to the presence of many peaks in a very small energy range. This can then certainly account for the small difference of 67 meV between calculated and measured shift. Yet, these reasons do not apply in the case of the (2×2)-3O, where theory predicts a vanishing S_2(1O) shift and which was measured at three photon energies. Here, however the weight of the S_2 component is quite small compared to the others, thus increasing the error in the experimental determination of its position. Under these circumstances we do not consider the small difference of 88 meV between theoretical and experimental shift to reflect a significant inconsistency. In conclusion, we hence find both data sets to be fully compatible with each other.

5.2.3 Discussion

Screening effects

While a main idea behind the study of SCLS's is to gain an understanding of the electronic and structural environment of atoms at the unperturbed surface, i.e. before the core excitation, the measured shifts comprise an additional component, which is due to the different screening capabilities of the

Table 5.4: Calculated Ru $3d$ SCLS's for the first layer atoms at various coverages. Shown are the total shifts, as well as their decomposition into screening and initial state parts: $\Delta^{\text{total}}_{\text{SCLS}} = \Delta_{\text{screen}} + \Delta^{\text{initial}}_{\text{SCLS}}$. The rightmost column contains the initial state shifts as obtained for Ru bulk truncated geometries. Units are meV.

	Total	Screening	Initial (relaxed)	Initial (bulk-trunc.)
clean, S_1	-383	-98	-285	-338
$p(2\times 2)$, S_1	-448	-80	-368	-407
$p(2\times 2)$, S_1(1O)	+36	-65	+101	+42
$p(2\times 1)$, S_1(1O)	-67	-111	+44	-12
$p(2\times 1)$, S_1(2O)	+395	-62	+457	+454
(2×2)-3O, S_1(2O)	+362	-80	+442	+476
(2×2)-3O, S_1(3O)	+1010	-27	+1037	+1088
(1×1)-O, S_1(3O)	+899	-85	+984	+1072

core-ionized system at the surface and in the bulk [24]. In fact, this screening capability is closely related to the electronic hardness and the surface chemical activity (see e.g. Stampfl et al. [141] and references therein); thus, also this information is of significant interest. Fortunately, the theoretical calculations provide the possibility to subdivide the total (measured) shifts into the initial state and the additional final state (i.e. screening) contributions.

Table 5.4 lists these components for all first layer atoms at the coverages considered. We see that the magnitude of the screening correction is rather small compared to the overall trend in the initial state shifts. Although it leads to an enhanced difference in the total shifts of equally coordinated Ru atoms particularly in the case of the S_1(1O) and S_1(3O) atoms, it still does not overshadow the clear dependence on the number of direct O neighbours (cf. fig. 5.11). Note that especially in the case of the small total shifts corresponding to singly O-coordinated Ru surface atoms, the screening contribution is even larger in magnitude than the initial state shift.

The final-state effect on the SCLS's of the clean surface have been already discussed in sect. 3.3.3. In presence of oxygen we observe that the screening correction for the S_2(1O) is even bigger (≈ 100 meV) than that for the S_2 component of the clean surface and, similar to the trend found for the first layer atoms always negative in sign (cf. Table 5.5). As all initial state S_2 and S_2(1O) are found to be positive, frequent sign changes are hence introduced by the screening contribution. Consequently, in the measurement the second layer shifts can lead to small peaks in close vicinity on *either side* of

Table 5.5: Calculated Ru 3*d* SCLS's for the second layer atoms at various coverages. Shown are the total shifts, as well as their decomposition into screening and initial state parts: $\Delta^{\text{total}}_{\text{SCLS}} = \Delta_{\text{screen}} + \Delta^{\text{initial}}_{\text{SCLS}}$. Units are meV.

	Total	Screening	Initial
clean, S_2	+124	-72	+196
$p(2\times2)$, S_2	+187	-19	+206
$p(2\times2)$, S_2(1O)	-57	-82	+25
$p(2\times1)$, S_2	+72	-34	+106
$p(2\times1)$, S_2(1O)	-21	-96	+75
(2×2)-3O, S_2	+39	-44	+83
(2×2)-3O, S_2(1O)	+3	-35	+38
(1×1)-O, S_2(1O)	-53	-83	+30

the bulk peak, which will be hard to resolve experimentally. As is apparent from the two fitting procedures employed in the present experimental analysis, this can then indirectly also influence the assessment of the larger first layer shifts. Given that the latter are typically the ones of primary interest, special care with respect to this point should therefore be exerted in the experimental data analysis.

In order to explain the behaviour of the screening contribution to the SCLS's we compare in fig. 5.12 the real self-consistent 4*d*-DOS, calculated inside the muffin tin spheres for the two limiting phases of the considered coverage range, i.e. the clean and the (1×1)-O surface. We see that, despite the widening of the *d*-band caused by the O adsorption, in close vicinity of the Fermi level the (1×1)-O phase shows an enhancement of the 4*d*-DOS with respect to the clean surface. This enhancement prevails also for all O covered surfaces. Consequently, since the final state effects at transition metal surfaces are due to intra-atomic *d*-electron screening, as described in the theory by Methfessel outlined in sect. 3.3.3, negative screening contributions are found throughout the whole coverage sequence.

It is interesting to compare this situation to the work for O adlayers on Rh(111) described in sect. 5.1. There, a sign change in the screening contribution was found (see Table 5.1 and fig.5.4), with the lower coverage surfaces screening again better than the bulk, but the higher O-covered surfaces screening worse (cf. fig. 5.13). This is connected to the fact that in Rh, which is situated just right of Ru in the periodic system, the Fermi level is located at a different position in the 4*d*-band. Above that position, the *d*-DOS is lowered so strongly upon O adsorption that it eventually falls below the value of the bulk *d*-DOS and thus induces the sign change in the screening correction (cf. fig. 5.7). In Ru on the other hand, this lowering

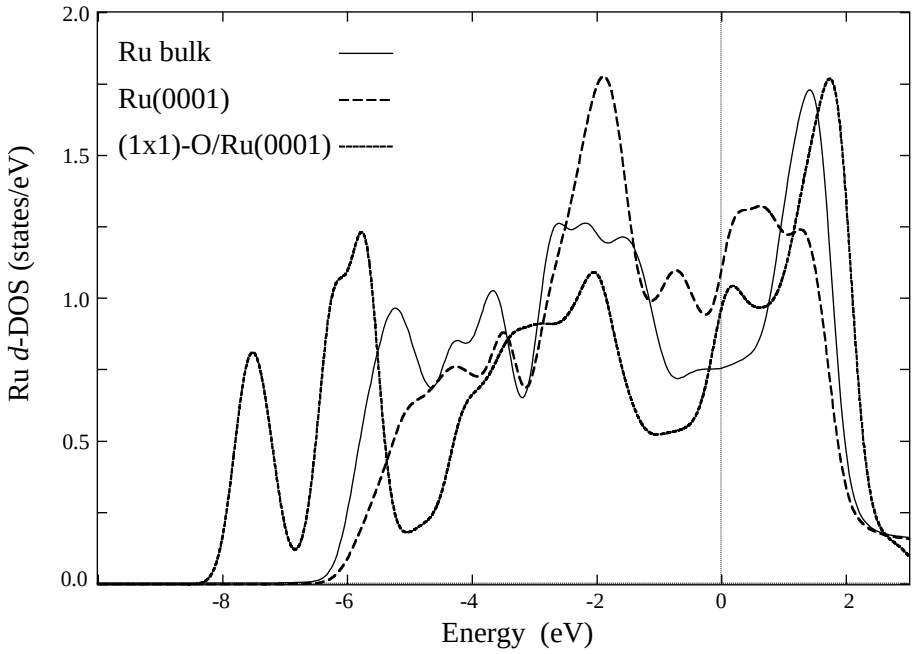

Figure 5.12: Calculated 4*d*-DOS for bulk Ru atoms (solid line) and for first layer Ru(0001) atoms of the clean (dashed line) and (1×1)-O covered surface (dotted line). The energy zero is at the Fermi level.

never reaches the bulk *d*-DOS (cf. fig. 5.12), so that the screening remains negative in sign throughout.

Initial state shifts

Once the final state effect contribution to the SCLS's is known, it is possible to discuss the oxygen induced initial state contribution. Upon O adsorption, the O 2*p* level interacts with the localized Ru 4*d* states, causing the formation of bonding and antibonding states close to the lower and upper edge of the valence 4*d*-band respectively (cf. fig. 5.12) [115]. The ensuing increased width of the valence band requires then again an adjustment of the center of gravity of the band in order to maintain local charge neutrality. This adjustment moves the band downwards in energy and the corresponding attractive contribution to the Kohn-Sham potential is reflected in more and more positive SCLS's with increasing O coverage. Further, as the width is connected to the formation of bonds, which obviously scale with the number of directly bound O atoms, similar SCLS's result for equally O coordinated Ru atoms.

In order to determine the 4*d*-band shift $\Delta C_{4d} = \epsilon_{4d}^{\mathrm{bulk}} - \epsilon_{4d}^{\mathrm{surf}}$ and relative width changes, $\Delta W = W^{\mathrm{surf}}/W^{\mathrm{bulk}} - 1$ between bulk and surface atoms, the first and second moment of the valence 4*d*-band for each first layer atom

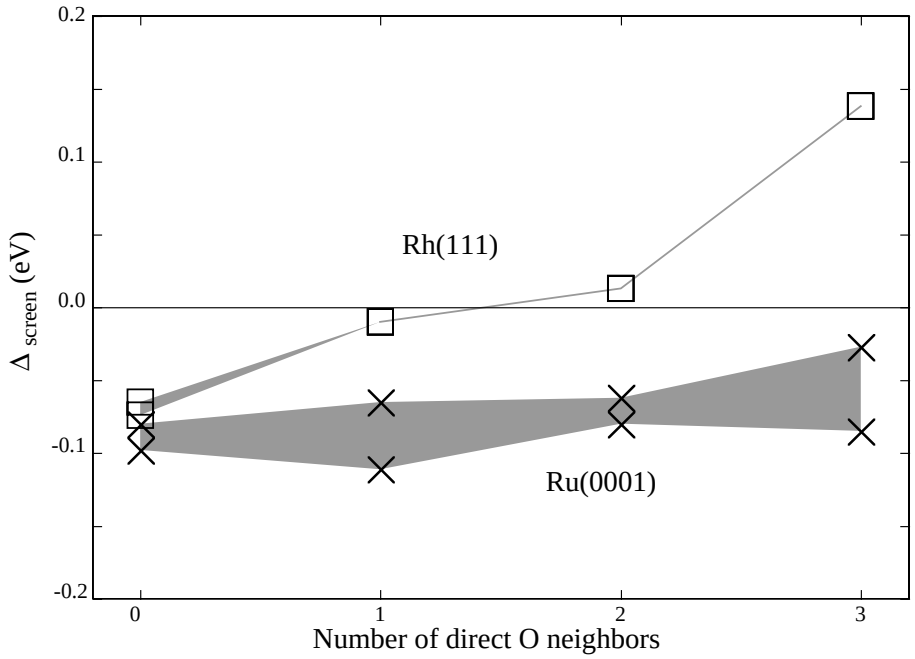

Figure 5.13: Comparison of the screening contribution, Δ_{screen}, for O/Ru(0001) (crosses) and O/Rh(111) (boxes) as a function of the number of directly coordinated O atoms. The shaded area is drawn to guide the eye.

at the coverages considered, have been evaluated. As shown in Table 5.6, the width of the d band increases when going from the not O coordinated S_1 atoms, which possess a band which is 12% narrower than the bulk one, and correspondingly is shifted by ≈ 0.2 eV to higher energies (cf. fig. 5.12), to the threefold O coordinated $S_1(3\text{O})$ atoms that have a 29% wider band than bulk Ru atoms, with its center of gravity hence shifted by ≈ 0.5 eV to lower energies (cf. fig. 5.12).

To gain a *qualitative understanding* in how far the observed shift of the center of gravity is due to the different band width, the simplistic rectangular d-band model, i.e. a box of constant d-DOS [81] was used. The resulting shifts, $\Delta\tilde{C}_{4d}$, are given in the middle column of Table 5.6 and match very well the ones obtained directly from the first moment of the real d-DOS. This confirms that the main driving force behind the observed $4d$-band shift, first up in energy for the clean surface and then increasingly down in energy with increasing O coordination, is indeed the notion to preserve local charge neutrality while the d-band width changes.

The shift of the d-band center is accompanied by a corresponding shift of the Kohn-Sham potential, which in turn is felt by the core electrons and gives rise to the initial state contribution to the SCLS's. In fig. 5.14 the spherically

Table 5.6: Shift of the center of gravity, ΔC_{4d} in meV, and relative change in the width, ΔW, of the Ru valence $4d$-band for all first layer atoms at the coverages considered with respect to the bulk situation. Additionally shown in the middle column is the shift of the center of gravity resulting from a simple rectangular d-band model as described in the text.

	ΔC_{4d}	$\Delta \tilde{C}_{4d}$ (model)	ΔW
clean, S_1	-200	-200	-12%
$p(2\times 2)$, S_1	-180	-180	-11%
$p(2\times 2)$, S_1(1O)	0	+30	+2%
$p(2\times 1)$, S_1(1O)	-20	+50	+3%
$p(2\times 1)$, S_1(2O)	+140	+220	+13%
(2×2)-3O, S_1(2O)	+160	+250	+15%
(2×2)-3O, S_1(3O)	+480	+480	+29%
(1×1)-O, S_1(3O)	+410	+480	+29%

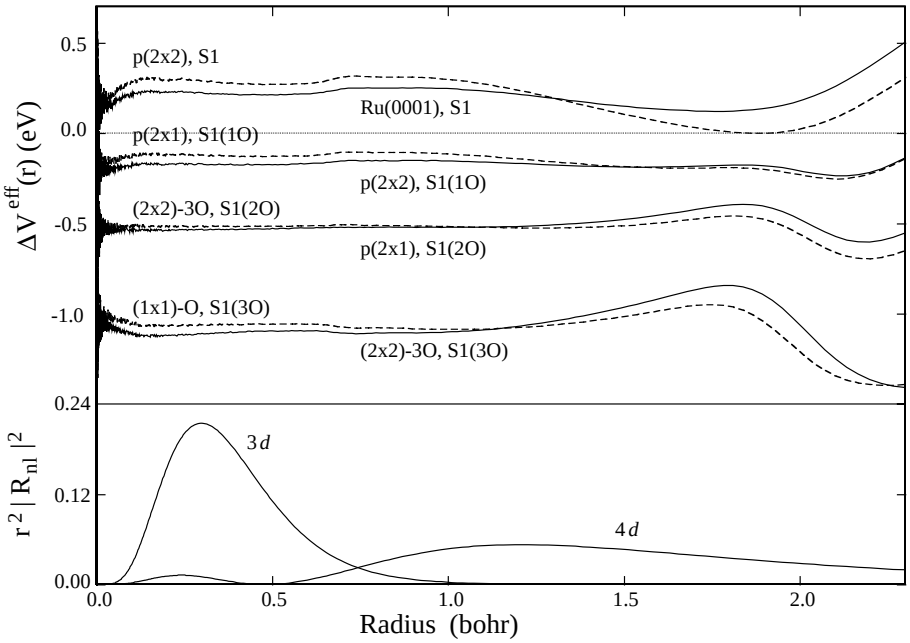

Figure 5.14: Top panel: Potential shift, $\Delta V^{\mathrm{eff}}(r)$, inside all first layer Ru muffin tin spheres for the various coverages considered. Bottom panel: Radial part of the wavefunction, $r^2\,|R_{nl}(r)|^2$, for the $3d$ and $4d$ orbitals of bulk Ru.

symmetric part of this potential shift, $\Delta V^{\rm eff}(r) = V^{\rm eff}_{\rm surf}(r) - V^{\rm eff}_{\rm bulk}(r)$, is shown as a function of the radial distance, $r = |\mathbf{r}-\mathbf{R}|$, from the nucleus at $\mathbf{R}$. The shift is primarily related to the number of directly coordinated O atoms, starts with positive shifts (more repulsive potential) for the S_1 type atoms and turns into more and more negative shifts for the S_1(1O), S_1(2O) and S_1(3O) atoms (more attractive potential). Interestingly, $\Delta V^{\rm eff}(r)$ is always almost constant up to about ≈ 1.2 bohr away from the core. Yet, this is the region seen by the $3d$ core electrons, as exemplified by the extension of the $3d$ radial wavefunction for bulk Ru also plotted in fig. 5.14. To first order [96],

$$\Delta^{\rm initial}_{\rm SCLS}(3d) \approx -4\pi \int dr\, \Delta V^{\rm eff}(r) r^2 |R_{3d}(r)|^2 \qquad (5.1)$$

holds. Given that $\Delta V^{\rm eff} \approx const$ in the region of the $3d$ orbital and the radial wavefunction is normalized, $\Delta^{\rm initial}_{\rm SCLS}(3d) \approx -\Delta V^{\rm eff}$ results. Of course, an analogous relation to eq. (5.1) holds also for all other deeper lying core levels which then display roughly similar shifts [29]. Obviously, this is not the case for the $4d$ valence band, which as shown in fig. 5.14 has a much larger radial extension. The magnitude of the shift of the center of gravity of the $4d$-band, C_{4d}, and of $\Delta^{\rm initial}_{\rm SCLS}$ will not be similar, while their overall trend is, as is indeed found when comparing the values given in Table 5.6 and Table 5.4 respectively.

Having established the relation between the measured SCLS and the local bonding, at least to the degree as it is reflected in the valence d-DOS, let us focus now on the second layer shifts. Here, only the S_2 type atoms of the clean and $p(2\times 2)$ phase display relatively large shifts of ≈ 200 meV, whereas the shifts of all other second layer atoms remain very small (cf. Table 5.5). Evaluating again the first and second moment of the d-DOS for these atoms, we indeed find only the widths for these two S_2 atoms increased by 5% with respect to the bulk value together with a corresponding shift of the $4d$-band center to lower energies, which gives rise to their positive SCLS's. Yet, while the increased width in the case of the first layer atoms can be explained in terms of binding to more and more O atoms, the second layer Ru atoms do not feel the presence of oxygen and always have the same number of nearest neighbours as in the bulk. In this respect it is interesting to notice that only the two mentioned S_2 atoms have first layer neighbours which are not yet bound to any O atom at all and which hence have somewhat unsaturated bonds. We thus argue that these still clean first layer atoms act like on the clean surface reinforcing their backbond to the second layer atom below, which resembles an increase of the coordination of the S_2 atoms giving a dilated d-DOS. Note that this is also reflected in the contraction of the first layer distance with respect to the bulk, which is found only for the lower O coverage phases [82, 83]. Judged from the width of the d-DOS, cf. Table 5.6, any Ru atom that has established bonds to at least

one O atom will not show an enhanced backbond tendency anymore, which explains why all other second layer atoms display a more or less bulk-like *d*-DOS width and consequently very small SCLS's.

SCLS's and charge transfer

Let's discuss now the relation between SCLS's and charge transfer.
In the simplest view, charge transfer off (onto) an atomic site leads to a more attractive (repulsive) potential, thereby causing a shift in the core level towards higher (lower) binding energy. In the case of chemisorption of an electronegative species like oxygen, one would hence expect each time more positive SCLS's for the higher O coordinated Ru first layer atoms, $S_1(1O)$, $S_1(2O)$, and $S_1(3O)$ respectively, as we indeed observe. Yet, despite this qualitatively correct trend, the question remains whether the SCLS's could further be used to better quantify the amount of charge actually transferred. Related to this is then also the question whether the total adsorbate-induced shifts could really be attributed solely to charge transfer.

Recent theories of SCLS's [19, 142, 143] have tried to separate the total shift into additional factors apart from charge transfer, namely an environmental and a configurational contribution. The former is viewed as arising from embedding the atom into the delocalized valence charge density of all neighbouring atoms. The ensuing overlap of these valence orbitals onto the atomic site influences the Kohn-Sham potential at the nucleus of the core ionized atom and thus contributes to the shift. Note that such a contribution obviously scales with the number of neighbours, i.e. in our case with the number of directly coordinated O atoms. The configurational contribution, on the other hand, arises in transition metals from the hybridization of the valence *d*-band with *sp* states below and above the Fermi level. The latter orbitals are much more diffuse, i.e. the corresponding charge is on average further away from the nucleus. Hence, a slight redistribution of electrons among these levels at the surface can then also influence the potential. For the particular case of ionic adsorbates on metals, also the polarization of the surface, which tries to screen the adsorbate electric field, has been discussed [114, 143].

Correspondingly, the total observable shift would then be the net result of all these (partially canceling) contributions. This argument was e.g. employed to explain the very small negative shifts observed for alkali metal adsorbates on W(110) in contrast to the large positive shifts caused by O/W(110) [19, 142, 144]. Neglecting any other contribution apart from charge transfer, one would in this case infer a much lower ionicity of the electropositive alkali metals compared to the electronegative oxygen [144]. Yet, this picture was contradicted by the more refined analyses taking also environmental and configurational contributions into account [19, 142]. In any case, although all these concepts like charge transfer, covalent bonding

or polarization are without doubt useful for our understanding, one has also to admit that they are somehow arbitrary (at least to a certain degree): Whether the build-up of charge between a surface atom and an adsorbate is called covalent bonding or polarization of the metallic charge in response to the adsorbate; or whether the overlap of valence orbitals onto other atomic sites is already called charge transfer or not is simply a matter of taste. In view of the analysis presented in the following, the very large shift of +1269 meV between the S_1 atoms of the clean surface and the threefold O coordinated S_1(3O) of the (1×1)-O phase is simply the consequence of the strong interaction of the O $2p$ orbitals with the metal $4d$ valence band, which gives rise to bonding and anti-bonding states widening the band. That this goes hand in hand with the sequential build-up of charge between the adsorbate and the Ru surface atom can be seen in fig. 5.14, where the surface potential shift shows a more and more pronounced inflection in the region further than ≈ 1.7 bohr away from the nucleus. Interpreting this to a certain degree as charge transfer to the O atoms would make the core-level analysis compatible with the continuous increase of the work function upon O adsorption [138] and with calculated charge difference density distributions. Yet, a clear assignment of how much charge is really transferred cannot be made on these grounds.

As a conclusion, we point out that SCLS's certainly are a sensitive probe of the local electronic structure around an atom, yet they intricately depend on the details of the interaction present in the system, which has to be properly analyzed for each specific case to understand the observed shifts. Therefore it does not make much sense to compare magnitudes of SCLS's arising in chemically different systems. On the other hand, within one type of chemistry, as e.g. in our case with the same adsorbate on the same substrate only at different coverages, the SCLS's may indeed be used to further describe the bonding situation – even in the more conceptual language of charge transfer.

In this view, the equal spacing of ~ 400 meV between SCLS's of increasingly higher O-coordinated Ru atoms (S_1, S_1(1O), S_1(2O), and S_1(3O)) suggests that the type of bonding remains the same throughout the whole coverage range studied, or in other words, that the (unspecified) amount of charge transferred to each O atom remains approximately constant. This interpretation is corroborated by an almost unchanged O_{1s} core level position to within ± 20 meV. In particular there is no indication of a qualitatively different chemisorption behaviour between the low coverage ($p(2 \times 2)$ and $p(2 \times 1)$) and the high coverage ((2×2)-3O and (1×1)-O) phases, that could explain the long-time believed, but only apparent saturation coverage of $\Theta = 0.5$ ML in UHV [83, 145]. As was already concluded in previous studies, this saturation arises therefore solely by kinetic hindrance of the O_2 dissociation process [137, 138]. Note, that a similar picture was derived in a recent experimental study on the O/W(110) system, which also exhibited

O-coordination dependent SCLS's up to $\approx$ 1 eV for the threefold coordinated W atoms [146].
Apart from this large scale trend, the SCLS's reflect also more subtle details of the bonding situation. This can be seen in the differences in the shifts for equally coordinated atoms present at two coverages; e.g. the shifts for the S_1(1O) type atoms in either the $p(2 \times 2)$ or the $p(2 \times 1)$ phase differ by 57 meV (cf. Table 5.4). These small variations can be due to a small redistribution of the charge at the two coverages, which one may interpret as a slightly different ionicity of the bond caused by the increased repulsion in a denser adsorbate mesh. Alternatively, they could be caused by the small differences in the atomic geometries of the two phases.
In order to develop a feeling for the separate magnitudes of these two, interrelated effects, let's focus on the SCLS's calculated for an artificial bulk truncated Ru surface with the increasing number of O atoms always sitting in hcp sites at a fixed height corresponding to the one deduced for the $p(2\times2)$ relaxed geometry. The related shifts are stated in Table 5.4, indicating that the geometrical changes induced by the adsorbate do amount to small shifts up to about 90 meV. Still, the differences between equally coordinated Ru atoms (now in completely identical nearest-neighbour surroundings for both phases) remain of the same order as before, reflecting now solely the slight charge rearrangement caused by the different adsorbate mesh at the two coverages.
In this respect we further note, that this sensitivity of the SCLS's to geometrical differences can also be used to ascertain e.g. the adsorption site. The calculated $\Delta^{\text{total}}_{\text{SCLS}}$ for O in fcc sites on the surface differ by $\approx 100 - 200$ meV from the ones shown in Table 5.4 and are always far outside the experimental error bar. The S_1(3O) shift of a (1×1)-O fcc phase would e.g. be at +718 meV. If there was a significant amount of O sitting in fcc sites at this coverage, it would certainly show up as a shoulder in the experimental spectrum. That this is not the case, cf. fig. 5.10, proves that the experimental (1×1)-O phase is nearly perfect hcp, despite the small binding energy difference between both hollow sites [137, 138].

O on Ru(0001) and Rh(111)

Finally, it is interesting to compare the O/Ru(0001) SCLS's to the ones found for O/Rh(111) described in sect. 5.1 (same adsorbate, similar transition metal substrates).

Fig. 5.15 displays the calculated initial state shifts sorted according to the number of directly coordinated O atoms. Apart from the different SCLS's of the clean surfaces caused by the different 4*d*-band filling [24], it is immediately obvious that both materials display almost the same relative O-induced shifts in the whole coverage range considered. The conclusion from these data is hence in line with the one of preceding DFT studies con-

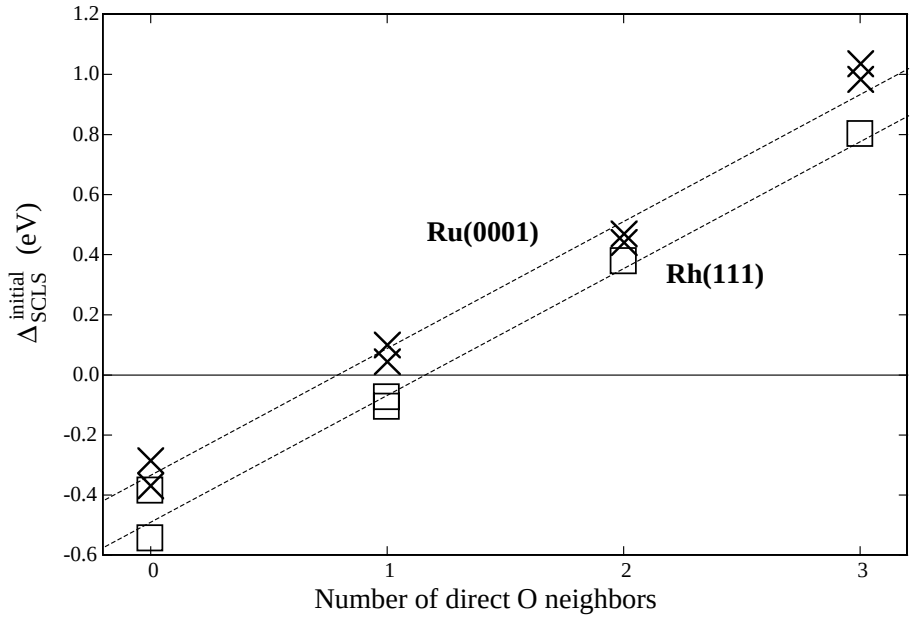

Figure 5.15: Comparison of the initial state shifts, $\Delta_{\mathrm{SCLS}}^{\mathrm{initial}}$, for O/Ru(0001) (crosses) and O/Rh(111) (boxes) as a function of the number of directly coordinated O atoms. The lines are drawn to guide the eye.

cerning the adsorption energetics [130, 138], which apart from the different adsorption site (hcp and fcc on Ru(0001) and Rh(111) respectively) found no qualitative difference in the on-surface O chemisorption behaviour. In particular, in this coverage range there is no hint towards a different catalytic behaviour of both materials at higher O partial pressures [147, 148], which hence presumably arises from different oxidation characteristics only after O has started to penetrate into the sample.

5.3 Conclusions

In this chapter we have presented the SCLS studies of oxygen chemisorption on Rh(111) and Ru(0001). For the first system we have performed SCLS experiments on the $p(2\times2)$ and $p(2\times1)$ structures while for the second, four oxygen ordered adlayer structures which form in UHV have been studied, namely the $p(2\times2)$, $p(2\times1)$, (2×2)-3O and (1×1)-O.
We find a clear dependence of the SCLS on the number of nearest neighbour O atoms for both systems. Moreover we obtain very good agreement between the experimentally determined SCLS's and first principles calculations, which confirms that within the GGA the latter are able to describe this quantity with high accuracy.
Using the theoretical approach, it was possible to separate the total SCLS's

into initial and final state contributions. We found that the screening properties of both surfaces are different in that the Ru(0001) surface is always able to screen the created core hole better than the bulk while the Rh(111) surface screens better only for the low coverage O phases. For both metals the initial state shifts are connected to a varying width of the valence $4d$ band either due to the reduced coordination of the atoms at the surface or to the interaction with the O $2p$ level which causes the formation of bonding and antibonding states widening the band. As the width of the band is connected to the formation of bonds, which scale with the number of directly bound O atoms, similar SCLS's result for equally O coordinated Rh and Ru atoms. The almost linear increase of $\Delta_{\mathrm{SCLS}}^{\mathrm{initial}}$ for increasingly higher O coordinated metal atoms suggests that the type of bonding remains roughly the same over the considered coverage sequence up to the full monolayer, which may be interpreted as an almost constant amount of charge transferred to each electronegative O atom. These findings confirm that both surfaces show a qualitatively similar on-surface chemisorption behaviour.

These results show that a combined experimental and theoretical determination of SCLS's provides valuable insight into the O-metal interaction in different chemical environments.

Conclusions and outlook

In this thesis, the properties of the core level shifts arising between surface and bulk atoms, so-called Surface Core Level Shifts (SCLS's), of bare and adsorbate covered metal surfaces have been investigated. The SCLS's are found to be a rich source of chemical and structural information that can be gained by comparing the experimental results to theoretical calculations. For the systems investigated here, the latter reproduce with high accuracy our experimental SCLS's thus demonstrating that the physical principles governing the SCLS's are well understood. This is due both to the reliability of the calculations as well as to the big advancement in the experimental equipment that allows now to measure SCLS's with very high accuracy.

The most important results of this work are summarized in the following. A more detailed summary of the various SCLS's aspects investigated here can be found in the conclusions of chapters 3, 4, 5.

(1) The SCLS is an interplay between initial state (before ionization) and final state (due to the presence of the core hole) effects. The separation of the two effects can be achieved only on theoretical grounds. The agreement between theory and experiments is really good only if both effects are represented well in the calculations.

(2) When dealing with SCLS's that present more than one shifted component, care must be taken in their assignment to certain atoms. SCLS's of this type are present even in the core level spectra of simple systems like clean metal surfaces. In these cases the SCLS's belong to different atomic layers. We have successfully applied for such systems the high energy resolution photoelectron diffraction approach to distinguish between the SCLS's of first and second layer atoms. Moreover we propose to extend this experimental procedure to other systems for which the surface geometry is already known.

(3) The SCLS's are sensitive to subtle changes of the geometric structure around the emitting atom like the case, for example, for surface thermal expansion. We have developed a new approach for the determination of the multilayer thermal expansion based on the coupling of SCLS measurements, taken at different temperatures, to SCLS theoretical calculations, performed on structures with different relaxations.

(4) The SCLS's are sensitive also to the changes of the chemical environ-

ment due to the presence of an adsorbate on the surface. We have found that the SCLS's are modified only on those substrate atoms directly bound to the adsorbate. This is a big advantage because, once a SCLS has been ascribed to a certain substrate atom, it allows to follow the kinetics of adsorption of a defined chemical species on the surface measuring the related SCLS's, which provide a complementary and useful information to the measurement of the core levels of the adsorbate. This is even more important when the adsorbate core levels are not measurable like for H and He, or overlap with some levels of the substrate, like for example the C1s with the $3d_{3/2}$ core level of Ru.

This study has been limited to the SCLS's of relatively simple systems, because their understanding is a fundamental prerequisite to that of more complicated ones.
Obviously, there are many other interesting problems where the SCLS approach can be applied to advantage. For instance, it is very fruitfully applied to the study of reconstructed surfaces, or that of alloys. For both cases we have already obtained some preliminary results which will be briefly described in the following.

Reconstructed surfaces

A system which is particularly suitable to study the effect of reconstruction on SCLS's is the Rh(110) surface, because it can be prepared in the form of $(1 \times n)$ (n=2,3,4 and 5) missing rows metastable reconstructed phases, where every n^{th} close-packed [110] row is missing.
We have performed preliminary measurements of the Rh $3d_{5/2}$ core level spectra of various $(1 \times n)$ reconstructed surfaces, namely those with n=0, 2 and 4. Fig. 5.16 presents the spectra of the three phases. It can be noted that the clean surface spectrum is composed by two peaks: the higher binding energy one at 307.15 eV originates from bulk atoms, while the lower binding energy component, shifted by $\approx$ 670 meV, stems from the first layer atoms. In the 1×2 and 1×4 phases two peaks appear instead of only one surface component, both at lower binding energies with respect to the bulk peak .
For the 1×2 system the two surface components are shifted by $\approx$ 450 and $\approx$ 710 meV towards lower binding energy; they can be ascribed to different first layer atoms. In fact, the atoms in the top rows along the [110] direction are less coordinated than the atoms of the clean surface; they then should display a larger SCLS. Therefore the -710 meV SCLS should belong to these atoms. Moreover in the (1x2) structure, microscopic facets oriented along the (111) crystallographic plane are formed and part of the second layer atoms have the same local surroundings as the atoms in the first layer of the (111) surface. In fact, the SCLS of 450 meV is very similar to that found for Rh(111) of -485 meV (see sect. 5.1).

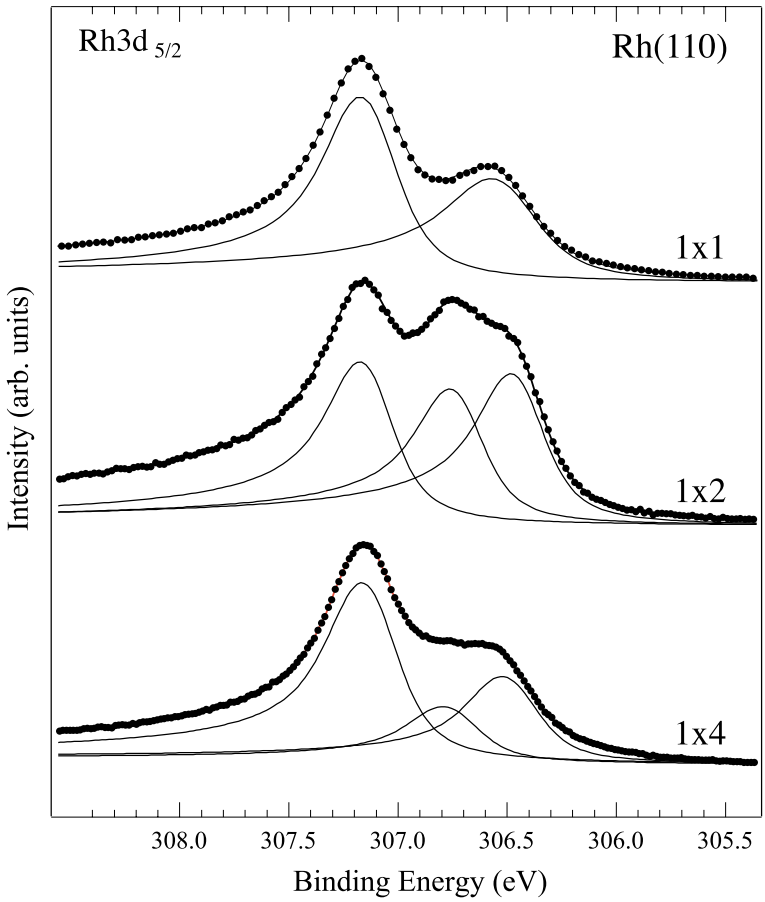

Figure 5.16: Rh $3d_{5/2}$ spectra from the clean 1×1 and 1×2 and 1×4 Rh(110) reconstructed surfaces. The different components found from the fit are also shown in the figure. The corresponding SCLS's are described in the text.

We are planning to follow the same strategy as adopted for the unreconstructed surfaces, i.e. characterize the clean reconstructed surfaces and then move on to adsorbates. In this case it will be interesting to see what is the role of the reconstruction on the adsorption process. The SCLS's look to be promising to obtain information on this question.
One can consider to push this technique even more and try to measure the SCLS's of kinks, steps or vacancies, features which belong to more realistic systems and play a role in chemisorption and catalytic processes.

Alloys

Another important branch to be explored is the study of transition metal alloys. Their fundamental importance stems from their extensive use in het-

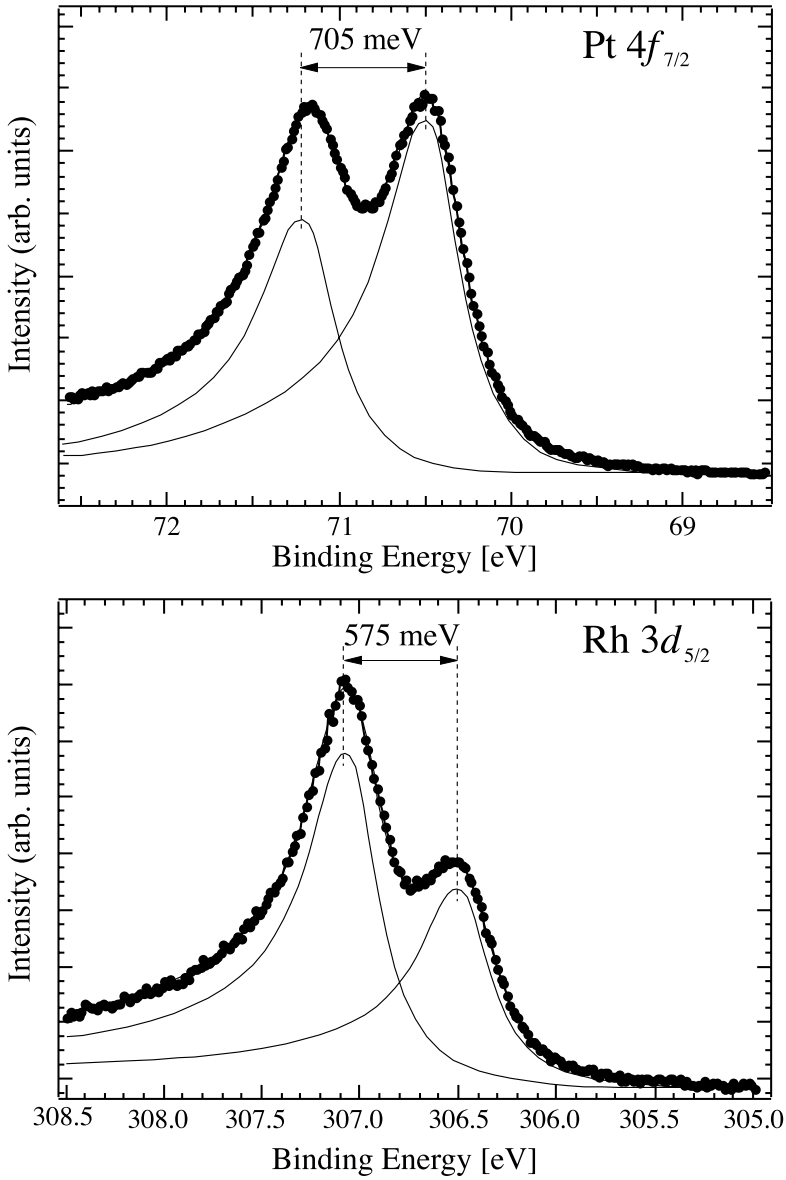

Figure 5.17: Pt $4f_{7/2}$ and Rh $3d_{5/2}$ spectra from the clean $Pt_{50}Rh_{50}(100)$ surface.

erogeneous catalysis. Therefore the knowledge of the surface composition during a chemical reaction is a fundamental prerequisite to find ways to improve their chemical activity.

In preliminary measurements we have already found that the SCLS approach is indeed very powerful to study alloys. In the particular case of the clean PtRh(100) surface it is possible to distinguish between the surface and bulk components of Rh and Pt separately (see fig. 5.17). This allows to use the

SCLS's to study the process of surface segregation, or to determine the exact surface composition during a chemical reaction taking place on the surface, like that between H_2 and O_2.
In the latter case, we have already seen that the Rh-O, Rh-2O, Rh-H, Pt-O, Pt-H etc. bonds give distinguishable components in the SCLS spectra. Following the behaviour of the different SCLS's at the various steps of the reaction we plan to quantify the oxygen and hydrogen coverages together with the relative populations of Rh and Pt on the surface. As an example we just mention that, from a first analysis of the already available data set, it is quite clear that the surface becomes Pt-enriched and the bulk is Rh-enriched at small oxygen on-surface coverages. We want to point out that this information is not as easily accessed by other techniques as it is with SCLS's.

Finally we want to stress again the wealth of quantitative information that the SCLS's contain. Hopefully, this thesis has shown that these informations can be extracted with a joint experimental-theoretical effort. The potentials offered by this technique will certainly be exploited more extensively in the future.

Bibliography

[1] A. Einstein, *Nobel Lectures in Physics*, Elsevier Publishing Company, Amsterdam (1964-1970).

[2] K.M. Siegbahn, *Nobel Lectures in Physics 1981-1990*, World Scientific Publishing Company, Singapore (1993).

[3] A. Zangwill, *Physics at surfaces*, Cambridge University Press (1988).

[4] D. Menzel, *Chemistry and Physics of Solid Surfaces*, edited by R. Vanselow (CRC Press, Boca Raton, FL, 1979), Vol. II, p. 227.

[5] N. Mårtensson and A. Nilsson, *High Resolution Core-Level Photoelectron Spectroscopy of Surfaces and Adsorbates*, Springer Series in Surface Science, Vol. 35, (1994) 65.

[6] C.S. Fadley, *Basic Concepts of X-ray Photoelectron Spectroscopy* in "Electron Spectroscopy: Theory, Techniques and Applications", C.R. Brundle and A.D. Baker, eds. (Academic Press, London, 1978), 2, p. 124 and references therein.

[7] P. Caldirola, R. Cirelli, G.M. Prosperi, *Fisica Teorica* UTET, Torino (1993).

[8] R. Manne and T. Alberg, Chem. Phys. Lett. **7**, 282 (1970).

[9] T.A. Koopmans, Physica **1**, 104 (1933).

[10] S. Hüfner, G.K. Wertheim, D.N.E. Buchanan, and K.W. West, Phys. Lett. A **46A**, 420 (1974).

[11] S. Hüfner and G.K. Wertheim, Phys. Rev. B **11**, 678 (1975).

[12] N. Mårtensson and A. Nilsson, J. Electr. Spect. Rel. Phenom. **52**, 1 (1990).

[13] W. F. Egelhoff, Surf. Sci. Rep. **6**, 253 (1987) and references therein.

[14] W. Bambynek, B. Craseman, R.W. Fink, H.U. Freund, H. Mark, C.D. Swift, R.E. Prince and P.V. Rao, Rev. Mod. Phys. **44**, 716 (1972).

[15] P.H. Citrin, G.K. Wertheim, and Y. Baer, Phys. Rev. B **16**, 4256 (1977).

[16] S. Doniach and M. Ŝunjić, J. Phys. C **3**, 185 (1970).

[17] K. Siegmahn, C. Nording, and E. Sokolowski, Proc. Rehovoth Conf. on Nuclear Structures (North-Holland, Amsterdam, 1957) p. 291.

[18] E. Sokolowski, C. Nording and K. Siegmahn, Phys. Rev. **110**, 776 (1958).

[19] P. Bagus, F. Illas, G. Paccioni, and F. Parmigiani, J. Electron. Spectrosc. relat. Phenom. **100**, 215 (1999).

[20] C. Wagner, W. Riggs, L. Davis, and J. Moulder, in Handbook of x-ray photoelectron spectroscopy, edited by G.E. Muilenberg (Perkin Elmer Corporation, Eden Prairie, Minnesota, 1979).

[21] P.H. Citrin, G.K. Wertheim, and Y. Baer, Phys. Rev. Lett. **41**, 1425 (1978) .

[22] M.C. Desonquéres, D. Spanjaard, Y. Lassailly, and C. Guillot, Solid State Commun. **34**, 807 (1980).

[23] G. Tréglia, M.C. Desonquéres, D. Spanjaard, Y. Lassailly, C. Guillot, Y. Jugnet, Tran Minh Duc and J. Lecante, J. Phys. C **14**, 3463 (1981).

[24] D. Spanjaard, C. Guillot, M.C. Desjonqueres, G. Treglia, and J. Lecante, Surf. Sci. Rep. **5**, 1 (1985) and references therein.

[25] R.E. Watson, M.L. Perlman, and J.F. Herbst, Phys. Rev. B **13**, 2358 (1976).

[26] C.S. Fadley, S.B.M. Hagström, M.P. Klein, and D.A. Shirley, J. Chem. Phys. **48**, 3779 (1968).

[27] A.R. Williams and C.D. Gelatt, Report of Workshop on ab initio One Electron Potentials, CECAM, 15 Yuly - 12 September 1975.

[28] P.H. Citrin, G.K. Wertheim, Phys. Rev. B **27**, 3176 (1983) and references therein.

[29] M. Methfessel, D. Hennig, and M. Scheffler, Surf. Sci. **287/288**, 785 (1993).

[30] M. Methfessel, D. Hennig, and M. Scheffler, Surf. Rev. Lett. **2**, 197 (1995).

[31] B. Johansson and N. Mårtensson, Phys. Rev. B **21**, (1980) 4427; Helv. Phys. Acta **56**, 405 (1983).

[32] A. Rosengren and B. Johansson, Phys. Rev. B **22**, 3706 (1980).

[33] A. Rosengren and B. Johansson, Phys. Rev. **23**, 3852 (1981).

[34] W. F. Egelhoff, Jr., Phys. Rev. Lett. **50**, 587 (1983).

[35] D. Tománek, V. Kumar, S. Holloway, and K.H. Bennemann, Solid State Comm., **41**, 273 (1982).

[36] N. Mårtensson, H. B. Saalfeld, H. Kuhlenbeck, and M. Neumann, Phys. Rev. B **39**, 8181 (1989).

[37] N. Mårtensson, A. Nilsson, J. Electron. Spectrosc. relat. Phenom. **75**, 209 (1995).

[38] J.C. Slater: *Quantum theory of matter*, Second edition 1968.

[39] P. Hohenberg and W. Kohn, Phys. Rev. **136**, B864 (1964).

[40] W. Kohn and L.J. Sham, Phys. Rev. **140**, A1133 (1965).

[41] W. Kohn. Nobel Lecture, Rev. Mod. Phys., **71(5)**, 1253 (1999).

[42] J.P. Perdew, S. Burke and M. Ernzerhof, Phys. Rev. Lett. **77**, 3865 (1996).

[43] P. Blaha, K. Schwarz and J. Luitz, **WIEN97**, *A Full Potential Linearized Augmented Plane Wave Package for Calculating Crystal Properties*, Karlheinz Schwarz, Techn. Universität Wien, Austria, (1999). ISBN 3-9501031-0-4.

[44] B. Kohler, S. Wilke, M. Scheffler, R. Kouba, and C. Ambrosch-Draxl, Comput. Phys. Commun. **94**, 31 (1996).

[45] M. Petersen, F. Wagner, L. Hufnagel, M. Scheffler, P. Blaha, and K. Schwarz, Comp. Phys. Commun. **126**, 294 (2000).

[46] J.F. Janak, Phys. Rev. B **18**, 7165 (1978); J.P. Perdew and M. Levy, Phys. Rev. B **56**, 16021 (1997).

[47] C.S. Fadley, *Synchrotron Radiation Research: Advances in Surface and Interface Science*, Vol. I: Techniques (Plenum Press, New York) 1992 and references therein.

[48] Y. Chen, F.J.G. de Abajo, A. Chassé, R.X. Ynzunza, A.P. Kaduwela, M.A. Van Hove, and C.S. Fadley, Phys. Rev. B **58**, 13121 (1998).

[49] A.P. Kaduwela, D.J. Friedman, and C.S. Fadley, J.Electron Spectrosc. Relat. Phenom. **57**, 223 (1991).

[50] S. Tanuma, C.J. Powell, D.R. Penn, Surf Interface Anal. **17**, 927 (1991); ibid **20**, 77 (1993); ibid **11**, 577 (1988).

[51] V. Fritzsche and P. Rennert, Phys. Status Solidi B **135**, 49 (1986); V. Fritzsche, J. Phys.: Condens. Matter **2**, 1413 (1990); V. Fritzsche, Surf. Sci. **265**, 187 (1992), ibid **213**, 648 (1989).

[52] J.J. Rehr and R.C. Albers, Phys. Rev. B, **41**, 8139 (1990).

[53] D. P. Woodruff and A. M. Bradshaw, Rep. Prog. Phys. **57**, 1029 (1994) and references therein.

[54] D.P.Woodruff Physica B **209**, 423 (1995); D.P. Woodruff, R. Davis, N.A. Booth, A.M. Bradshaw, C.J.Hirschmugl, K-M.Schindler, O. Schaff, V. Fernandez, A. Theobald, Ph. Hofmann and V. Fritzsche Surf.Sci. **358**, 19 (1996).

[55] Yufeng Chen and Michel A. Van Hove, http://electron.lbl.gov/mscdpack/

[56] A. Barbieri, M.A. Van Hove http://electron.lbl.gov/leedpack.

[57] A. Baraldi, M. Barnaba, B. Brena, D. Cocco, G. Comelli, S. Lizzit, G. Paolucci, and R. Rosei, J. Electron Spectr. Rel. Phenom. **76**, 145 (1995).

[58] A. Baraldi and V. R. Dhanak, J. Electr. Spectroscopy **67**, 211 (1994).

[59] L. Gori, R. Tommasini, G. Cautero, D. Giuressi, M. Barnaba, A. Accardo, S. Carrato, and G. Paolucci, Nucl. Instr. and Meth. A **431**, 338 (1999).

[60] E.E. Koch, Handbook on Syncrotron Radiation, Vol. 1a.

[61] A. Abrami et al., Rev. Sci. Instrum. **66**, 1618 (1995).

[62] L. I. Johansson, H. I. P. Johansson, J. N. Andersen, E. Lundgren and R. Nyholm, Phys. Rev. Lett. **71**, 2453 (1993).

[63] L. I. Johansson, H. I. P. Johansson, J. N. Andersen, E. Lundgren and R. Nyholm, Phys. Rev. B **49**, 17460 (1994).

[64] Ph. Hofmann, K. Pohl, R. Stumpf and E. W. Plummer, Phys. Rev. B **53**, 13715 (1996).

[65] R. Döll, L. Hammer, K. Heinz, K. Bedürftig, U. Muschiol, K. Christmann, A. P. Seitsonen, H. Bludau and H. Over, J. Chem. Phys. **108**, 8671 (1998).

[66] R. Stumpf and P. J. Feibelman, Phys. Rev. B **51**, 13748 (1995).

[67] V. M. Silkin and E. V. Chulkov, Phys. Solid State **37**, 1540 (1995).

[68] E. V. Chulkov, V. M. Silkin and E.N. Shirykalov, Surf. Sci. **188**, 287 (1987).

[69] M. Aldén , H.L. Skriver, and B. Johansson, Phys. Rev. Lett. **71**, 2449 (1993); M. Aldén, I.A. Abrikosov, B. Johannson, N.M. Rosengaard, and H.L. Skriver, Phys. Rev. B **50**, 5131 (1994).

[70] P. J. Feibelman, Phys. Rev. B **49**, 13809 (1994).

[71] P. J. Feibelman and R. Stumpf, Phys. Rev. B **50**, 17480 (1994).

[72] R. Stumpf, J. B. Hannon, P. J. Feibelman and E. W. Plummer, Proceedings Heraeus Seminar 1995, World Scientific

[73] Ph. Hofmann, R. Stumpf, V. M. Silkin, E. V. Chulkov and E. W. Plummer, Surf. Sci. **355**, L278 (1996).

[74] V. Fritzsche, Surface Science **265**, 187 (1992) and references therein.

[75] D. M. Ceperley and B. J. Alder, Phys. Rev. Lett. **45** (1980) 566 as parameterized by J. P. Perdew and A. Zunger, Phys. Rev. B **23** 5048 (1981).

[76] G. K. Wertheim and P. H. Citrin, Phys. Rev. B **30**, 4343 (1984).

[77] G. K. Wertheim and P. H. Citrin, Phys. Rev. B **38**, 7820 (1988).

[78] J. N. Andersen, D. Henning, E. Lundgren, M. Methfessel, R. Nyholm and M. Scheffler, Phys. Rev. B **50**, 17525 (1994).

[79] W. Nichtl, N. Bickel, L. Hammer, K. Heinz, and K. Muller, Surf. Sci. **188**, L729 (1987).

[80] H. Over, H. Bludau, M. Skottke-Klein, G. Ertl, W. Moritz, and C.T. Campbell, Phys. Rev. B **45**, 8638 (1992).

[81] J. Friedel, In: *The Physics of Metals*, (Ed.) J.M. Ziman, Cambridge University Press, Cambridge (1969), p. 340.

[82] M. Lindroos, H. Pfnür, G. Held, and D. Menzel, Surf. Sci. **222**, 451 (1989).

[83] H. Pfnür, G. Held, M. Lindroos, and D. Menzel, Surf. Sci. **220**, 43 (1989).

[84] A. A. Quong and A. Y. Liu, Phys. Rev. B **56**, 7767 (1997).

[85] M. Lazzeri and S. de Gironcoli, Phys. Rev. Lett. **81**, 2096 (1998).

[86] J.H. Cho and M. Scheffler, Phys. Rev. Lett. **78**, 1299 (1997); N. Marzari, D. Vanderbilt, A. De Vita and M.C. Payne, Phys. Rev. Lett. **82**, 3296 (1999).

[87] Ismail, E.W. Plummer, M. Lazzeri, and S. de Gironcoli, Phys. Rev. B **63**, 233401 (2001); M. Lazzeri and S. de Gironcoli, *ibid* **65**, 245402 (2002).

[88] J.W.M. Frenken *et al.*, Phys. Rev. Lett. **58**, 401 (1987); Y. Chao and E. Conrad, *ibid* **65**, 2808 (1990); P. Statiris *et al.*, *ibid* **72**, 3574 (1994); A.P. Baddorf and E.W. Plummer, *ibid* **66**, 2770 (1991).

[89] R. Nyholm, M. Qvarford, J.N. Andersen, S.L. Sorensen, and C. Wigren, J. Phys. Condens. Matter **4** , 277 (1992).

[90] E. Lundgren, U. Johansson, R. Nyholm, and J.N. Andersen, Phys. Rev. B **48**, 5525 (1993).

[91] A. Borg, C. Berg, S. Raaen, and H.J. Venvik, J. Phys. Condens. Matter **6**, L7 (1994).

[92] M. Zacchigna, C. Astaldi, K.C. Prince, M. Sastry, C. Comicioli, R. Rosei, C. Quaresima, C. Ottaviani, C. Crotti, A. Antonini, M. Matteucci, and P. Perfetti, Surf. Sci. **347**, 53 (1996).

[93] M. Zacchigna, C. Astaldi, K.C. Prince, M. Sastry, C. Comicioli, M. Evans, and R. Rosei, Phys. Rev. B **54**, 7713 (1996).

[94] A. Beutler, E. Lundgren, R. Nyholm, J.N. Andersen, B. Setlik, and D. Heskett, Surf. Sci. 371, 382 (1997); Surf. Sci. **396**, 117 (1998).

[95] F. Strisland, A. Ramstad, T. Ramsvik, and A. Borg, Surf. Sci. **415**, L1020 (1998).

[96] M.V. Ganduglia-Pirovano, V. Natoli, M.H. Cohen, J. Kudrnovsky, and I. Turek, Phys. Rev. B **54**, 8892 (1996).

[97] A. Baraldi, V.R. Dhanak, G. Comelli, K.C. Prince, and R. Rosei, Phys. Rev. B **56**, 10511 (1997).

[98] J. Xie and M. Scheffler, Phys. Rev. B **57**, 4768 (1998).

[99] G. Teeter, D. Hinson, J.L. Erskine, C.B. Duke, and A. Paton, Phys. Rev. B **57**, 4073 (1998).

[100] D.M. Riffe, G.K. Wertheim, and P.H. Citrin, Phys. Rev. Lett. **67**, 116 (1991).

[101] G.K. Wertheim, D.M. Riffe, and P.H. Citrin, Phys. Rev. B **49**, 2277 (1994).

[102] L. Hedin and A. Rosengren, J. Phys. F: Metal Phys., **7**, 1339 (1977).

[103] W. Theis and K. Horn, Phys. Rev. B **47**, 16060 (1993).

[104] A. Goldoni, A. Baraldi, G. Comelli, S. Lizzit, G. Paolucci, Phys. Rev. Lett. **82**, 3156 (1999).

[105] K. Pohl, J.-H. Cho, K. Terakura, M. Scheffler, and E.W. Plummer, Phys. Rev. Lett. **80**, 2853 (1998).

[106] S. Baroni, A. Dal Corso, S. de Gironcoli and P. Giannozzi, http://www.pwscf.org

[107] L. Kleinman and D.M. Bylander, Phys. Rev. Lett. **48**, 1425 (1982).

[108] M. Lazzeri, and S. de Gironcoli, Surf. Sci. **402-404**, 715 (1998); *ibid* **454-456**, 442 (2000).

[109] E. Pehlke and M. Scheffler, Phys. Rev. Lett. **71**, 2338 (1993).

[110] L.I. Johansson, P.-A. Glans, and T. Balasubramanian, Phys. Rev. B **58**, 3621 (1998).

[111] J.N. Andersen, T. Balasubramanian, C.-O. Almbladh, L.I. Johansson and R. Nyholm, Phys. Rev. Lett. **86**, 4398 (2001).

[112] S. de Gironcoli, unpublished.

[113] K.A. Maeder and S. Baroni, Phys. Rev. B **55**, 9649 (1997).

[114] J. Bormet, J. Neugebauer, and M. Scheffler, Phys. Rev. B **49**, 17242 (1994).

[115] M. Scheffler and C. Stampfl, *Theory of Adsorption on Metal Substrates*, In: Handbook of Surface Science, Vol. 2: Electronic Structure, (Eds.) K. Horn, M. Scheffler. Elsevier Science, Amsterdam (2000), p. 286.

[116] R.S. Mulliken, J. Chem. Phys. **23**, 1833 (1955).

[117] R. Hoffmann, *Solids and Surfaces: A Chemist's View of Bonding in Extended Structures*, VCH, New York (1988).

[118] R.F.W. Bader, *Atoms in Molecules. A Quantum Theory*, Int. Series of Monographs on Chemistry, Vol. 22, Oxford University Press, Oxford (1990).

[119] A.D. Becke and K.E. Edgecombe, J. Chem. Phys. **92**, 5397 (1990).

[120] G. Comelli, V. R. Dhanak, M. Kiskinova, K. C. Prince, R. Rosei, Surf. Sci. Rep. **32**, 165 (1998) and references therein.

[121] J. T. Grant and T. W. Haas, Surf. Sci. **21**, 70 (1970).

[122] D. G. Castner, B. A. Sexton and G. A. Somorjai, Surf. Sci. **71**, 519 (1978); D. G. Castner and G. A. Somorjai, Surf. Sci. **83**, 60 (1979); D. G. Castner and G. A. Somorjai, Appl. Surf. Sci. **6**, 29 (1980).

[123] K. C. Wong, K. C. Hui, M. Y. Zhou and K. A. R. Mitchell, Surf. Sci. **165**, L21 (1986).

[124] K. C. Wong, W. Liu and K. A. R. Mitchell, Surf. Sci. **360**, 137 (1996).

[125] S. Schwegmann, H. Over, V. De Renzi and G. Ertl, Surf. Sci. **375**, 91 (1997).

[126] S. Schwegmann and H. Over, Surf. Sci. **393**, 179 (1997); H. Xu and K. Y. S. Ng, Surf. Sci. **393**, 181 (1997).

[127] H. Xu and K. Y. S. Ng, Surf. Sci. **375**, 161 (1997).

[128] T. Greber, J. Wider, E. Wetli, J. Osterwalder, Phys. Rev. Lett. **81**, 1654 (1998).

[129] D. Loffreda, D. Simon, and P. Sautet, J. Chem. Phys. **108**, 6447 (1998).

[130] M. V. Ganduglia-Pirovano and M. Scheffler, Phys. Rev. B **59**, 15533 (1999).

[131] K. D. Gibson, M. Viste, E. C. Sanchez, and S. J. Sibener, J. Chem. Phys. **110**, 2757 (1999).

[132] J. Wider, T.Greber, E. Wetli, T. J. Kreutz, P. Schwaller, and J. Osterwalder, Surf. Sci. **417**, 301 (1998); *ibid* **432**, 170 (1999).

[133] J. N. Andersen, M. Qvarford, R. Nyholm, S. L. Sorensen and C. Wigren, Phys. Rev. Lett. **67**, 2822 (1991).

[134] A. Baraldi, S. Lizzit and G. Paolucci, Surf. Sci. Lett. **457**, L354 (2000).

[135] M. V. Ganduglia-Pirovano, J. Kudrnovský, and M. Scheffler, Phys. Rev. Lett. **78**, 1807 (1997).

[136] M. Gsell, M. Stichler, P. Jakob, and D. Menzel, Israel J. Chem. **38**, 339 (1998).

[137] C. Stampfl, S. Schwegmann, H. Over, M. Scheffler, and G. Ertl, Phys. Rev. Lett. **77**, 3371 (1996).

[138] C. Stampfl and M. Scheffler, Phys. Rev. B **54**, 2868 (1996).

[139] M. Stichler, Ph.D. thesis, Techn. Universität München (1998).

[140] J.P. Perdew and Y. Wang, Phys. Rev. B **45**, 13244 (1992).

[141] C. Stampfl, M.V. Ganduglia-Pirovano, K. Reuter, and M. Scheffler, Surf. Sci. **500** 368 (2002) .

[142] G.A. Benesh and D.A. King, Chem. Phys. Lett. **191**, 315 (1992).

[143] P.S. Bagus, C.R. Brundle, G. Pacchioni, and F. Parmigiani, Surf. Sci. Rep. **19**, 266 (1993).

[144] D.M. Riffe, G.K. Wertheim, and P.H. Citrin, Phys. Rev. Lett. **64**, 571 (1990).

[145] T.E. Madey, H.A. Engelhardt, and D. Menzel, Surf. Sci. **48**, 304 (1975).

[146] D.M. Riffe and G.K. Wertheim, Surf. Sci. **399**, 248 (1999).

[147] C.H.F. Peden and D.W. Goodman, J. Phys. Chem. **90**, 1360 (1986).

[148] C.H.F. Peden, D.W. Goodman, D.S. Blair, P.J. Berlowitz, G.B. Fischer, and S.H. Oh, J. Phys. Chem. **92**, 1563 (1988).

Publications

The works strictly related to this thesis can be found in the following papers:

S. Lizzit, K. Pohl, A. Baraldi, G. Comelli, V. Fritzsche, E.W. Plummer, R. Stumpf, and Ph. Hofmann, *Physics of the Be(10$\bar{1}$0) surface core level spectrum*, Phys. Rev. Lett. **81**, 3271 (1998).

A. Baraldi, S. Lizzit, G. Comelli, A. Goldoni, Ph. Hofmann and G. Paolucci, *Core–level subsurface shifted component in a 4d transition metal: Ru(10$\bar{1}$0)*, Phys. Rev. B **61** 4534 (2000).

A. Baraldi, G. Comelli, S. Lizzit, R. Rosei, and G. Paolucci, *Effects of the interatomic–potential anharmonicity on the bulk and surface photoemission core levels*, Phys. Rev. B **61** 12713 (2000).

M.V. Ganduglia–Pirovano, M. Scheffler, A. Baraldi, S. Lizzit, G. Comelli, G. Paolucci, and R. Rosei, *Oxygen–induced Rh $3d_{5/2}$ surface core-level shifts on Rh(111)*, Phys. Rev. B **63** 205415 (2001).

S. Lizzit, A. Baraldi, A. Groso, K. Reuter, M.V. Ganduglia–Pirovano, C. Stampfl, M. Scheffler, M. Stichler, C. Keller, W. Wurth, and D. Menzel, *Surface core–level shifts of clean and oxygen–covered Ru(0001)*, Phys. Rev. B **63** 205419 (2001).

A. Baraldi, S. Lizzit, K. Pohl, Ph. Hofmann, and S. de Gironcoli, *Multilayer thermal expansion of Be(0001) determined from surface core level shifts*, submitted to Phys. Rev. Lett..

Other publications on SCLS's are:

A. Goldoni, A. Baraldi, M. Barnaba, G. Comelli, S. Lizzit, and G. Paolucci, *Experimental evidence of magnetic effects at the Rh(100) surface*, Phys. Rev. Lett. **82** 3156 (1999).

A. Baraldi, S. Lizzit, and G. Paolucci, *Adsorption sites determination*

by mean of High-Resolution Surface Core Level Shift: oxygen on Ru(10$\bar{1}$0), Surf. Sci. Lett., **457**, L354-L360 (2000).

A. Baraldi, S. Lizzit, G. Comelli and G. Paolucci, *Oxygen adsorption and ordering on Ru(10$\bar{1}$0)*, Phys. Rev. B **63**, 115410 (2001).

A. Baraldi, S. Lizzit, A. Novello, G. Comelli and R. Rosei, *Second-layer surface core level shift on Rh(111)*, submitted to Phys. Rev. B.

A. Baraldi, S. Lizzit, G. Comelli, M. Kiskinova, R. Rosei, K. Honkala and J.K. Norskov, *Surface core level shifts as fingerprints of adsorption sites and of local changes of chemical reactivity*, in preparation.

Acknowledgements

Many, sincere thanks to all who supported me during these years and contributed to the successful completion of this thesis.

First of all I want to express my gratitude to my supervisor Prof. Dr. Dietrich Menzel. I must say that it has been a privilege to be one of his PhD students and to work with him for quite a long time. It is always a pleasure to speak with him of science, not only because he is always an unbelievable source of new ideas but also because he combines his knowledge about physics with humanity in an admirable way. *Thanks a lot !*

The person who I have worked closest with in the experiments of this thesis as well as in my overall scientific activity, is Alessandro (Aldo). He has been and actually is a great friend not only during the activities concerning physics, where he is always highly motivated and efficient, but also out of work. Thank you Aldo for this.
I wish to thank Giorgio for giving me the possibility and the freedom to pursue my personal scientific interest in these years and also for his trust in me when he left the SuperESCA beamline in my hands.
I wish to thank Giovanni, Maya and Renzo for their help and precious advice.
Special thanks go to my coworkers of the superESCA group, Andrea, Guillermo, Luca, Maurizio, Rosanna, for their friendship which makes my days (and nights) at work pleasent. Thanks a lot for your contribution in making the SuperESCA laboratory a great place to work.
I'm also thankful with Philip for his friendship and for the nice moments we spent together. It's always very nice to work with you!
Many thanks to Daniele for his great help on the beamline. I'm also grateful to Michele which is helping me really a lot in the final preparation of the thesis.
I'm grateful to most of the users that came, and still come to the SuperESCA for their beamtimes. Among them I want to thank especially Peter Feulner and Wilfried Wurth for their help concerning experiments and physics, Krassi, Georgi and Bobi (the bulgarian team) for teaching me some bulgarian songs like *shtip shtipbididip* and for supporting the Udinese football

team, and all the people from the department of Prof. Menzel which I had the big pleasure to work with during beamtimes in Trieste.

There are so many other persons who deserve to be acknowledged that naming them all would need several pages. Thanks a lot to all of you!!!

Finally, special and sincere thanks I owe to my parents for their continuous support and help in pursuing my decisions. My brothers and sister deserve to be acknowledged as well as their children who always encouraged me but .... never believed I would have finished this thesis.

....and, Simona, for your love and for all the beautiful moments of my life with you. I love you!